CHAPTER 1

INTRODUCTION

1.1 GENERAL INTRODUCTION

The advent of radioactive ion beam technologies has opened numerous areas of inquiry for practitioners of nuclear science. Until recently, investigation of the atomic nucleus and its properties had been restricted to the 300 or so nuclides in the valley of β-stability as opposed to the some 7000 nuclides that are predicted to be particle bound. The new experimental tools that permit the production and isolation of radioactive species have empowered theorists and experimentalists to engage in studies that would not be possible in their absence. Among the many fields that have been broached in the near past are studies of nuclear structure, nuclear reactions, the nature of astrophysical cycles, and the cosmological processes postulated to have initiated the universe.

The degree to which we understand the nucleus is often measured by the ability of theoretical models to predict fundamental properties such as isotopic masses, half-lives, β-decay systematics, delayed particle emission, and reaction strengths. Structure models, such as the shell model, are continually tested and refined by experimental data that restrict or fix the input parameters; and models of stellar and cosmological nucleosynthesis are similarly affected by both decay and reaction measurements. What follows is a brief summary of the importance of studying the decay of ^{19}N and ^{20}N by experiment for their ability to illuminate specific aspects of nucleosynthesis and their

relevance with regard to the predictions and refinement of the structure models in this mass region.

1.2 STRUCTURE

Measuring the beta decay properties of a nuclide provides information about the quantum state of that isotope and states in the daughter that are populated during the decay. Though the energy spectrum of the emitted betas is continuous, observation of delayed particles (gamma rays, protons, neutrons, alphas) whose spectra are discreet typically permits quantitative determination of the daughter level fed by the beta decay.

If the relative energy of the parent and daughter ground states are known then the energy of the populated level can be deduced from the secondary particle. This then allows for the Q-value of the beta decay to be calculated by difference. Further, if the strength of the specific transition, also known as the branching ratio, can be measured quantitatively then the energy of the transition coupled with the strength of the transition can be utilized to calculate the log(ft) value. Knowing the log(ft) value facilitates the assignment, or at least a restriction, on the spin and parity of the intermediate level in the daughter that was fed by the beta transition.

The most salient features predicted by models of nuclear structure, particularly the shell model, are the energy and quantum properties of excited states in nuclei. Although there are others, the spins, parities and energies are the most easily tested by experiment and, for the most part, are quantities upon which other inferred properties are based. The utility of the shell model in principle lies in the hope that the model will be applicable to systems that may not be accessible to experimental inquiry. In order to

inspire confidence toward extrapolation, it is necessary for the model to be proven valid in systems that are testable by experiment.

For the specific cases of studying ^{19}N and ^{20}N, the decay measurements will provide insight into the structure of ^{19}O and ^{20}O respectively. By restricting the spin and parity of the excited levels populated during the decay, the predictions of the shell model for these nuclides will be tested. Since these isotopes are relatively light, and since the perturbing nuclear quantities tend to be more dramatic as nucleons are added, it behooves the shell model to accurately describe the properties in this region prior to extrapolation to more exotic species.

1.3 NUCLEOSYNTHESIS

The generation of elements from the basic nuclear constituents is believed to have occurred during the early stages of the so-called big bang and within the interior of stellar objects – which is an ongoing process. The process is driven by the fusion of seed nuclei with simple, low mass objects such as neutrons, protons and alphas. Many of the reactions and their cross sections are known for the fusion of stable isotopes with the lighter particles, however, most of the reaction cross sections for capture by unstable species have not been measured.

To make the network calculations for the production of elements, and hence the isotopic abundances, it is necessary to know or estimate the reaction cross sections for many radioactive species with the simple species. This is true of both the primordial and stellar nucleosynthesis networks. Although it would be desirable to measure the reaction cross sections for all nuclei with the low mass subset, such voluminous, comprehensive assessments are not currently required. Typically, specific reactions are

targeted as being particularly important to measure experimentally while other, less perturbing reaction rates may be estimated systematically. One reaction cross section that has been propounded as important for both inhomogeneous models of the big bang (IMB) and stellar nucleosynthesis is the neutron capture on ^{18}O producing ^{19}O and gamma rays.

The standard model of the big bang predicts that elements beyond lithium will not be produced with any appreciable strength. The IMB model, where the number of neutrons is larger than protons, predicts that elements up to and beyond mass (A=20) may be generated [94Ra]. The production of elements beyond neon in this model proceeds through the generation of ^{18}O via the $^{14}C(\alpha,\gamma)$ and $^{17}O(n,\gamma)$ reactions. Here mass may either be recycled through the $^{18}O(p,\alpha)^{15}N$ reaction or mass may be built up through the $^{18}O(n,\gamma)^{19}O$ reaction. For material to be processed out of the CNO range into the mass (A=20) region, the strength of the $^{18}O(n,\gamma)$ reaction must exceed that of the $^{18}O(p,\alpha)$ reaction [96Me]. Thus, ^{18}O represents a potential end-point for the accumulation of mass in the IMB scenario; rendering the $^{18}O(n,\gamma)^{19}O$ a quantity of primary importance to measure.

With regard to network calculations in astrophysics: the ^{18}O seed nuclide is utilized in the mass build-up occurring in the helium core burning stage of asymptotic giant branch stars. In these objects, ^{18}O is manufactured from alpha capture on ^{14}N and processed through to ^{22}Ne by the $^{18}O(\alpha,\gamma)$ reaction. These sites are propounded to be the main locales for the slow neutron capture process (s-process); where the source of the neutron production is via the $^{22}Ne(\alpha,n)$ reaction. If the $^{18}O(n,\gamma)$ reaction strength is relatively high, the neutron production (and thus s-process rates) will be dramatically

altered. The reason being two-fold: first, if the $^{18}O(\alpha,\gamma)$ reaction competes well with the $^{18}O(\alpha,\gamma)$ then neutron production will be quenched by removing the ^{22}Ne seed from the $^{22}Ne(\alpha,n)$ reaction, and second, a strong $^{18}O(n,\gamma)$ will remove neutron material from the system that would otherwise initiate the s-process on different seed nuclei. Consequently, an experimental insight into the $^{18}O(n,\gamma)$ reaction is of critical importance as an input parameter for the network calculations of this stellar environment.

One manner by which information may be gained with regard to the $^{18}O(n,\gamma)^{19}O$ reaction is by measuring the decay properties of ^{19}N. By measuring the beta branching strength of ^{19}N to levels in ^{19}O and calculating the log(ft) values, the spins and parities of the populated levels can be restricted. From these level properties, at least those levels above the neutron emission threshold, the resonant neutron capture strength of the $^{18}O(n,\gamma)$ reaction can be calculated.

1.4 LITERATURE SEARCH - ^{19}N, ^{20}N

Numerous publications appear in the literature with regard to experimental studies of the decay modes of ^{19}N and ^{20}N. In fact, there have been half-life studies, measurements of the total neutron emission probability, and an experiment designed to record the γ-ray spectra following the decay of ^{19}N. However, rather than clarifying the decay properties of these nuclides, the published quantities are disparate - rendering the inferred decay modes dubious at best. What follows is an overview of the published experimental studies relevant to the decay properties of these neutron rich nuclides.

1.5 PRIOR MEASUREMENTS OF ^{19}N DECAY PROPERTIES

The energy level scheme of the mass A=19 system pertinent to the decay of ^{19}N is shown in figure 1 [95Ti]. The scheme indicates that the β-decay Q-value is about

12.5 MeV (see also [93Au]), while the maximum energy available for β-delayed neutron emission is about 8.5 MeV. In addition, β-delayed alpha particle emission is energetically possible by about 3.5 MeV and, although this particular channel has not been observed experimentally, similar decay channels have been observed during the decay of other nitrogen isotopes [].

There are eight known levels in the ^{19}O daughter above the ground state that are bound with respect to neutron emission. Therefore, any beta feeding to these levels will result in the emission of one or more de-excitation γ-rays. What is more, there are some forty known levels in ^{19}O above the neutron emission threshold through which β-delayed neutron emission is, at least, energetically possible. Given that there is so much energy available for β-delayed neutron emission and that there are so many levels through which such a transition may occur, it should not be surprising that β-delayed neutron emission comprises a significant fraction of the decay strength of this nuclide.

Experimental study of the decay of ^{19}N began at GANIL in 1986 with an experiment by Dufour *et al.* where β-delayed γ-ray spectroscopy was performed [86Du]. The results of the study found the half-life of ^{19}N to be 0.32(10) seconds and they were also able to identify three γ-ray transitions which they ascribed to levels in ^{19}O. The characteristic energies of the three gamma lines were found to be 96.0, 709.2, and 3137.8 keV with relative intensities of 100(10), 63(21), and 76(21), respectively. The energies imply a cascade from the 3.9449 MeV level through the 3.2316 and 0.0960 MeV levels, however, the errors on the intensities confound any serious attempt to determine specific branching strengths to individual levels in the ^{19}O daughter.

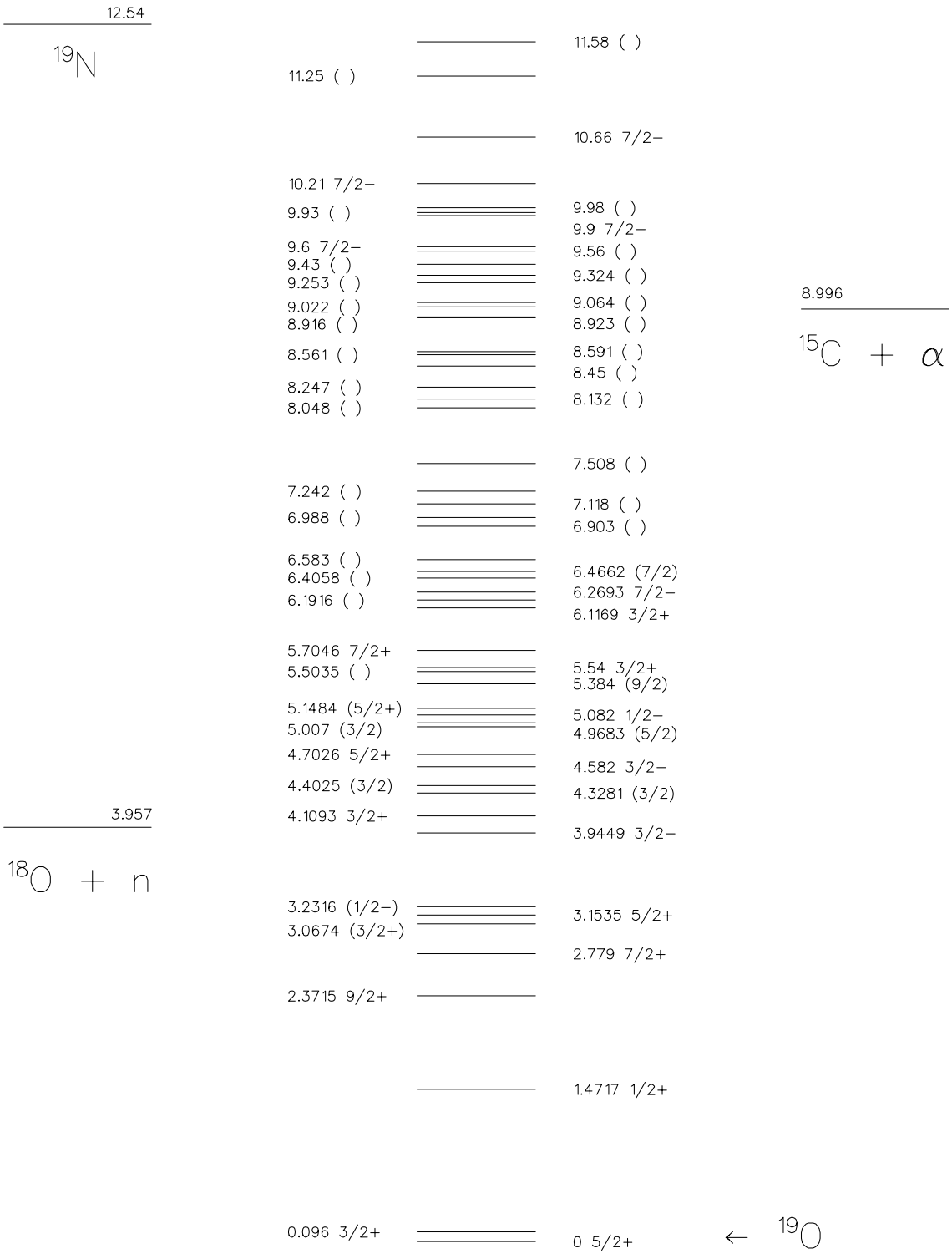

Figure 1 Energy level diagram of the portion of the mass 19 system pertinent to the decay of ^{19}N. The energies are given in MeV and are relative to the ground state of ^{19}O.

Indeed, the Dufour result is in itself an enigma because other studies [look for them in tilley] where the 3.9449 MeV level has been populated (through transfer reactions) suggest that this state relaxes to the ground state, 0.0960 and 1.4717 MeV excited states with approximately the same probability [95Ti]. The text of Dufour *et al.* indicates that their experiment was sensitive to transitions in this energy range - thus the absence of these lines in their report is puzzling.

There have been two experiments conducted in the past to measure the total neutron emission probability (P_n) of ^{19}N. The fist was performed at GANIL by Mueller *et al.* [], and the second by Reeder and collaborators at LAMPF [88Mu]. The GANIL study re-measured the half-life to be 0.210(+200 –100) seconds and found P_n to be 0.33 (+34 -11), while the Reeder group determined the half-life to be 0.329(19) seconds and the total neutron emission probability to be 0.624(26) of the decay strength. Though the two measurements of the P_n value agree within error, the Mueller result is highly uncertain and, what is more, the Reeder value has since been retracted by private communication [97Gi] and in conference proceedings [95Re]. The latter report gives an updated analysis of the same 1991 data and yields a half-life of 0.255(10) seconds, and the revised P_n as 0.487(21) of the total decay strength. Consequently, the only remaining refereed value in the literature for the P_n strength of ^{19}N is that reported by Mueller.

To date there has been no experiment to make a spectroscopic measurement of delayed neutrons emitted by ^{19}N. The only spectroscopic evidence appears in a publication by Ozawa and collaborators in 1995 [95Oz] where ^{19}N appears as a contaminant in their experiment designed to measure the delayed neutron spectrum of

^{19}C. They were able to attribute one peak in the neutron TOF spectrum as being due to the decay of ^{19}N. This neutron appeared at an energy of 0.59 MeV in the lab and was attributed to the ^{19}N β-decay populating the 4.1093 MeV state in ^{19}O. Their interpretation was based on the change in intensity of this peak as a function of time relative to the other observed neutrons. This is the only published spectroscopic result with respect to neutron emission from ^{19}N.

1.6 PRIOR MEASUREMENTS OF ^{20}N DECAY PROPERTIES

The data in the literature pertinent to the decay of ^{20}N is less by comparison to ^{19}N. The portion of the mass (A=20) system for the decay of ^{20}N is shown in figure 2. There have been two measurements of the half-life and two measurements of the P_n value of its decay. Once again, the two papers are those by Mueller and the Reeder collaborations [88Mu, 91Re]. The Mueller result gives the half-life to be 0.100(+30 – 20) seconds and the P_n as 0.53(+11 -7), while the Reeder publication of 1991 lists the half-life as 0.142(19) seconds and the total neutron emission probability to be 0.661(50) as a fraction of the total decay strength. Again, the Reeder values were updated in 1995 [95Re] and the new values are given as 0.129(8) for the half-life and 0.520(33) for the P_n value. There is no data available with respect to γ-ray emission following the β-decay, and no publication involving a spectroscopic measurement of delayed neutrons emitted by ^{20}N.

1.7 LITERATURE SEARCH SUMMARY

In total, there have been six half-life measurements of ^{19}N however those with the better statistical accuracy do not agree to within two standard deviations. The value of the P_n strength that remains in the literature is largely uncertain, and the delayed γ-ray

data do not agree with other, related measurements on the excited states of ^{19}O. The ^{20}N experiments have better agreement in half-life and P_n value but independent confirmation of the Mueller result [88Mu] is still desirable. There is no spectroscopic or branching strength data available for ^{20}N regarding beta, delayed neutron or γ-ray emission. A summary of the experimental data currently in the literature, regarding the decay of ^{19}N and ^{20}N, is given in table 1.

Table 1 Literature search results for experimental measurement of the relevant decay properties of ^{19}N and ^{20}N.

QUANTITY	^{19}N	^{20}N	REF.
Q_β (MeV)	12.54	17.97	93Au
Half-Life (ms)	329 (19)	142 (19)	91Re
	210 (+200)(-100)	100 (+30)(-20)	88Mu
	235 (32)	-	88Sa
	300 (80)	-	88Du
	320 (100)	-	86Du
	255 (10)	129 (8)	95Re
Neutron Emission Probability (%)	62.4 (26)	66.1 (50)	91Re
	33 (+34)(-11)	53 (+11)(-7)	88Mu
	48.7 (21)	52.0 (33)	95Re
Decay γ-Rays (keV)	96, 709, 3138	N/A	86Du

1.8 SHELL MODEL PREDICTIONS FOR THE DECAY OF ^{19}N

In 1988, following the appearance in the literature of the Dufour experimental results [], a shell model study of the ^{19}N decay was published by Warburton [88Wa]. Essentially, the paper included calculations of the B(GT) strength for each of the allowed and first forbidden transitions to levels in ^{19}O. In this model the ground-state spin and parity of ^{19}N was assumed to be (1/2-), which is consistent with the known spin and parity of the other odd-mass nitrogen isotopes, and the program OXBASH []

was used to determine the spin, parity and energy of the ^{19}O levels. The salient features of the shell model results are as follows. First, only about 7% [6%] of the beta strength

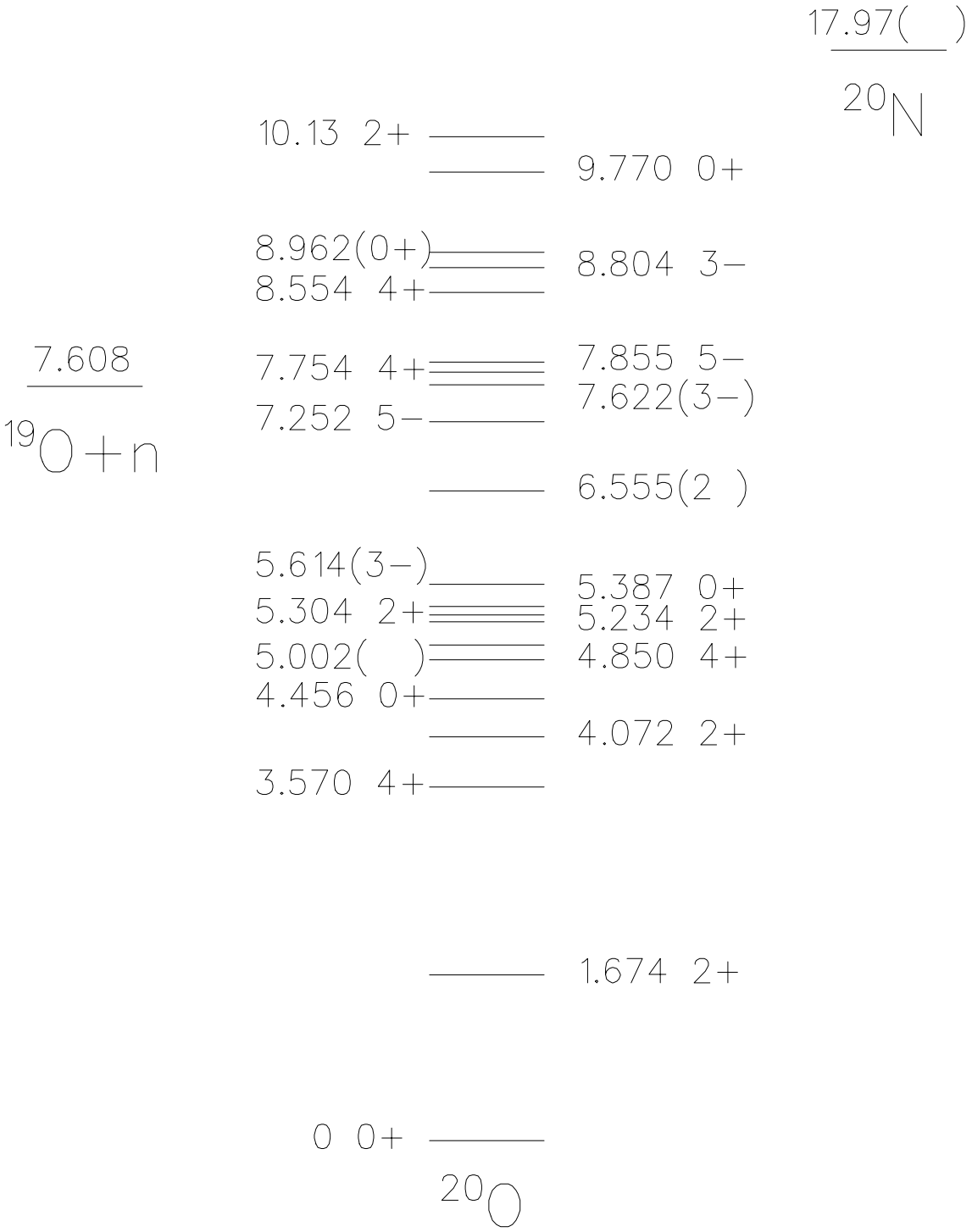

Figure 2 Energy level diagram for the portion of the mass 20 system relevent to the decay of ^{20}N.

populates γ-emitting allowed [first forbidden] final states in ^{19}O. Second, that the fraction of the decay leading to neutron emission should be about 0.87 (or 87%) of the total decay strength. Third, that the half-life of ^{19}N should be about 0.54 seconds. And fourth, that less than 5% of the allowed strength populates levels in ^{19}O above the (^{15}C + α) threshold.

Taking the theoretical and experimental results together, it may be concluded that the calculated half-life over-predicts the observed half-life by about a factor of two, and that the total β-delayed neutron emission probability, P_n, is predicted to be significantly higher than that which has been measured. Also, the model predicts significant β-strength to bound levels that would yield (either directly or through cascade) the 1376 keV γ-ray characteristic of the transition between the 1472 and 96 keV levels in ^{19}O – a transition that was not observed in the Dufour experiment [88Du].

Warburton comments that, if the calculated B(GT) values to the allowed states under-predict the actual values by and order of magnitude, the missing transition strength would by reduced to a degree where the experimental study [] may not have been sensitive to it. Increasing the B(GT) values in this way would also bring the model half-life in line with experiment, however, the P_n value under those conditions would be reduced to about 0.3 or 30% of the total branching strength. Indeed, Warburton summarizes that the predicted P_n value is very large given the energy range and number of bound states available in ^{19}O, and suggests that experimental measurement of the total neutron and γ-ray emission probabilities may be the only way to measure the absolute β-strengths to low lying levels in ^{19}O.

1.9 EXPERIMENTAL GOALS

In light of the litany of shortcomings and potential errors in the measured values of the ^{19,20}N decay modes and the general disagreement between experiment and theory in the case of ^{19}N, an experiment to re-measure the decay properties of ^{19}N and ^{20}N was proposed at the National Superconducting Cyclotron Laboratory. The goals of the experiment were to thoroughly establish the decay properties of these nuclides by making spectroscopic measurements of the delayed neutrons and γ-rays emitted during their decay. From these measurements, the predictions of the shell model may be compared and contrasted with experiment, and the importance of the ^{18}O(n,γ) reaction in both the IMB and stellar nucleosynthesis networks can be estimated.

CHAPTER 2

EXPERIMENTAL SETUP

2.1 PRODUCTION OF SECONDARY RADIOACTIVE ION BEAMS

The only naturally occurring sources of the isotopes of interest are the hot, dense environments associated with stellar objects. When this is taken together with the fact that the half-lives of ^{19}N and ^{20}N are reportedly less than one second [95Ti], it should not be surprising that there are no terrestrial samples of these nuclides upon which experiments may be performed. As a result, a facility capable of artificially generating these isotopes was required.

One facility capable of producing ^{19}N and ^{20}N in yields commensurate with the experimental goals is the National Superconducting Cyclotron Laboratory at Michigan State University. In this study, the necessary radioactive ion beams (RIBs) were generated by fragmenting an intense primary beam of ^{22}Ne in a Beryllium target. The primary beam of ^{22}Ne was accelerated in the K1200 Cyclotron and extracted at an energy of 80 MeV/A. The ^{22}Ne beam then struck a thin Beryllium foil (564mg/cm^2) resulting in the production of a wide variety of secondary fragments near or below mass (A=22).

The nuclides of interest were selected, sequentially, using the A1200 fragment mass analyzer [91Sh]. The fragmentation products were separated on the basis of their mass to charge ratio (A/Z) by the first set of A1200 dipoles. The specific nuclides were

further separated from other reaction products by passing them through an achromatic wedge (241 mg/cm^2 Al equivalent) and the second pair of A1200 dipoles. The wedge induced momentum shifts, based on the atomic charge of the recoil products, allowing unambiguous separation among nuclides at the final focus of the A1200.

Once purified, the RIBs were transported, using various electromagnetic devices, to the low background experimental end-station located in the N3 vault at the NSCL complex. Generally speaking, the transmission of the secondary beam from the A1200 focus to the experimental end-station was about 80 percent over the course of the study. For this experiment, the primary beam was pulsed to allow for efficient and conclusive data recording. The beam-on and beam-off intervals were selected on the basis of the half-life of the nuclide being transported to the experimental end-station. The beam pulsing sequences for each nuclide studied are given in table 2.

Table 2 Beam-On and Beam-Off pulsing times for each nuclide investigated.

Nuclide	Experimental Runs	Beam-On Time	Beam-Off Time
^{17}N	17 - 23	8 s	12 s
^{16}C	46 - 50	1.5 s	3 s
^{19}N	59 - 90	1 s	3 s
^{20}N	93 - 105	0.5 s	0.8 s
^{20}N	106 - 116	0.375 s	0.375 s

2.2 EXPERIMENTAL END STATION

The radioactive beams of ^{16}C, ^{17}N, ^{19}N, and ^{20}N initially passed through a parallel plate avalanche counter (PPAC) located at the inlet of the 92” chamber and immediately upstream of the main detector array. The PPAC was most useful during the preliminary beam tuning as it provided position information on the incoming beam.

Downstream of the PPAC, the RIBs passed through a thin Zirconium window separating the beam-line vacuum (10^{-6} torr) from the end station that was at atmospheric pressure. The detection system consisted of four dependent sub-systems that will be referred to as the implantation system, neutron bar array, ^{6}Li array, and Germanium pair.

2.3 IMPLANTATION SYSTEM

After transmission through the PPAC, the ion beam entered the first detection sub-system called the implantation system. The implantation system consisted of two transmission mounted, silicon surface barrier detectors, a series of aluminum degrader foils, and a thin plastic scintillator. The silicon detectors were 300 um thick and had surface areas of 300mm^2. The scintillator was made of BC412 plastic and had the dimensions of 2.5cm x 2.5cm x 0.3cm deep. The two silicon detectors were placed one on the upstream side, and one on the downstream side of the plastic scintillator. The upstream silicon was referred to as the dE detector, the downstream silicon as the VETO detector, and the plastic scintillator was referred to as the START detector. The components of the implantation system and the detector designations are shown in Figure 3.

During the beam-on intervals, the beam passed first through the dE detector, was degraded in the aluminum foils, and then implanted into the START scintillator. The dE detector provided a useful real-time monitor of the purity of the secondary beam, while the dE detector in concert with the START detector and the VETO detector provided data on the fraction and purity of the secondary beam actually implanted within the scintillator.

During the beam-off intervals, the scintillator generated a signal caused by transmitted beta particles from the decay of the implanted species. This provided valuable data for half-life measurements and the determination of the total number of decay events and also provided a start signal for the delayed neutron time-of-flight spectroscopy.

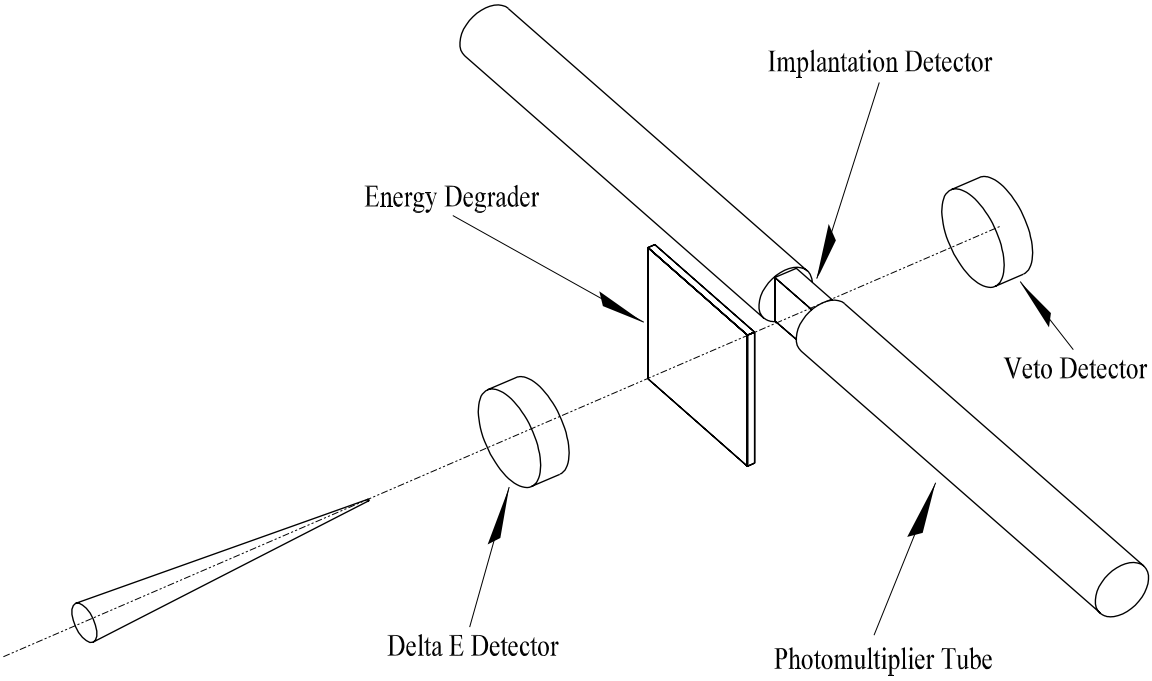

Figure 3 The implantation system showin the diagnostic silicon elements and the implantation or START scintillator.

2.4 NEUTRON BAR ARRAY

The second detector system utilized in this study was the so-called Neutron Bar Array. The neutron bar array was originally constructed by Dr. Richard Harkewicz during the period of his graduate study at Michigan State University [92Ha]. This array consists of sixteen plastic scintillator bars, composed of BC412 plastic, with the approximate dimensions 157cm x 7.6cm x 2.54cm thick. The scintillator bars were

shaped such that the radius of curvature of every bar is equal to one meter. The sixteen neutron bars are housed in an aluminum frame with the bars arranged such that they are concentric with a single point in space. At this point, the START detector is situated to enable a time-of-flight technique for the determination of delayed neutron energies.

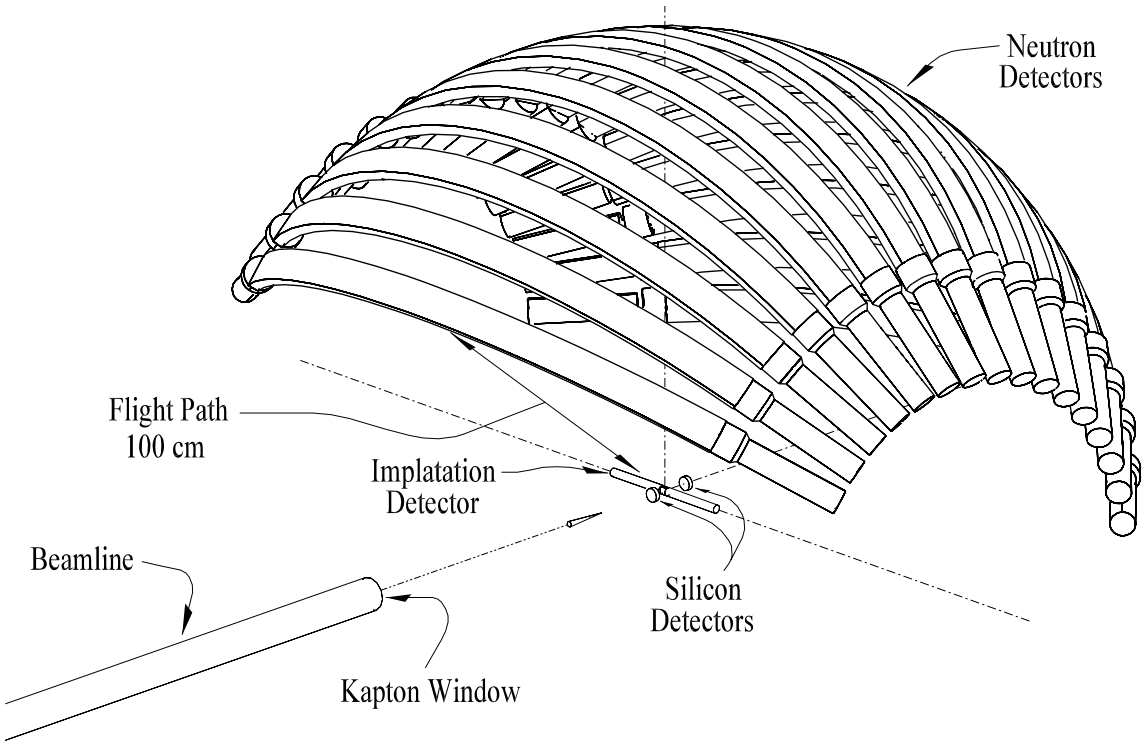

Figure 4 The neutron bar array showing the sixteen bars and the implantation system situated at the geometric center of the device.

The beta decay in the implantation scintillator provides a common start while a neutron event detected within an array bar provides the individual stop. The time difference between the events yields the time-of-flight and, knowing the flight path, the neutron energy. The neutron bar array was selected for its ability to efficiently detect delayed neutrons in the energy range between one MeV and ten MeV. A schematic diagram of the neutron bar array is shown in Figure 4.

2.5 ^{6}Li GLASS SCINTILLATORS

To detect beta-delayed neutrons emitted with energies lower than the threshold of the neutron bar array, the detector end-station housed three inorganic scintillators containing enriched quantities of ^{6}Li. The detectors were right-cylindrical with radii equal to 2.54 cm. Two of the three were 2.54 cm deep while the depth of the third crystal was equal to 1cm. The three detectors were placed about the START scintillator without shadowing the bars of the array, and with as much separation as possible to minimize scattering among the devices. The two thicker ^{6}Li glass scintillators were placed about 25cm from the source activity while the thinnest detector was situated about 10cm from the source activity.

The ^{6}Li glass scintillators also provided spectroscopic information on delayed neutron emission using a TOF technique. Again, the implantation scintillator provided a start signal from the beta decay and the detection of a neutron by a ^{6}Li glass scintillator gave an individual stop signal.

2.6 HIGH PURITY GERMANIUM DETECTORS

To detect gamma rays emitted during the decay of the isotopes of interest, the detector end-station included two, high purity germanium crystals. The detectors were 120% and 80% efficient relative to standard sodium iodide and were placed as close as possible to the source activity given the physical constraints of the neutron bar array and its supporting apparatus. The detectors were situated upstream of the source activity to minimize the effect of the opening angle with respect to the beam-pipe. The angle between the detectors and the implantation position was about eighty degrees. The more efficient (Ge#1) and the less efficient (Ge#2) were placed at about 17cm and

22cm away from the source activity, respectively. Figure 5 is a schematic representation of the end station showing the implantation system, the neutron bar array, ^{6}Li detectors and germanium detectors.

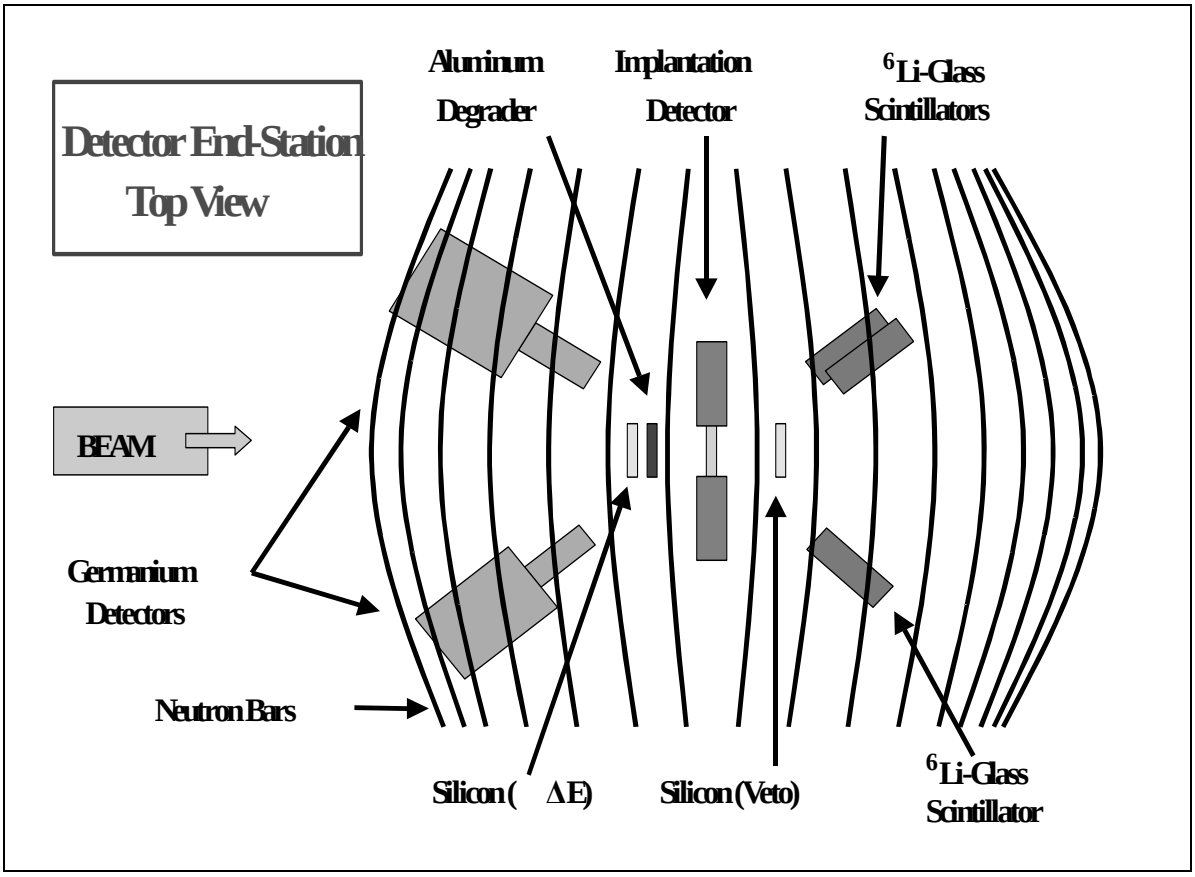

Figure 5 Schematic diagram of the experimental end-station viewed from above.

2.7 ELECTRONICS AND DATA ACQUISTION

Data taking for the experiment employed standard electronics modules available within the NSCL electronics pool for all systems including the CAMAC portion. The beam pulsing signals were supplied by a programmable dual gate generator where a TTL signal was input to the cyclotron follower, causing the current supply for the last cyclotron beam line magnet to be altered. This initiated a beam-off interval within the electronics protocol.

For both the beam-on and beam-off intervals, a master gate was caused by an event in the implantation scintillator. This event in conjunction with the beam-status bit (on or off) triggered reads in the electronics for the detectors of interest. The neutron detectors were disabled during the beam-on period, as was the real-time clock, however, the germanium detectors were enabled during both the beam-on and beam-off intervals. Figures 6-8 show the electronics set-up utilized in this experiment.

The data were recorded on an event-by-event basis and written to 8mm tape for subsequent analysis offline. The in-house SARA [] analysis code was utilized for both online and offline purposes along with the associated XAMINE [] display package. The data taking was divided into runs of approximately two hours duration to ensure manageability of the files during analysis.

2.8 SECONDARY BEAM PURITY

In this experiment, four radioactive ion beams were generated by the fragmentation of a ^{22}Ne beam in a beryllium foil. Two of the beams were produced for calibration purposes (^{16}C and ^{17}N) and two of the beams were the isotopes of interest for the experiment (^{19}N and ^{20}N). The purity of the secondary beams was established at two points. The first was during beam tuning through the A1200 fragment mass analyzer (which is independent of the user defined set-up in the experimental vaults) and the second was by analysis of the data recorded downstream by the implantation system at the end-station.

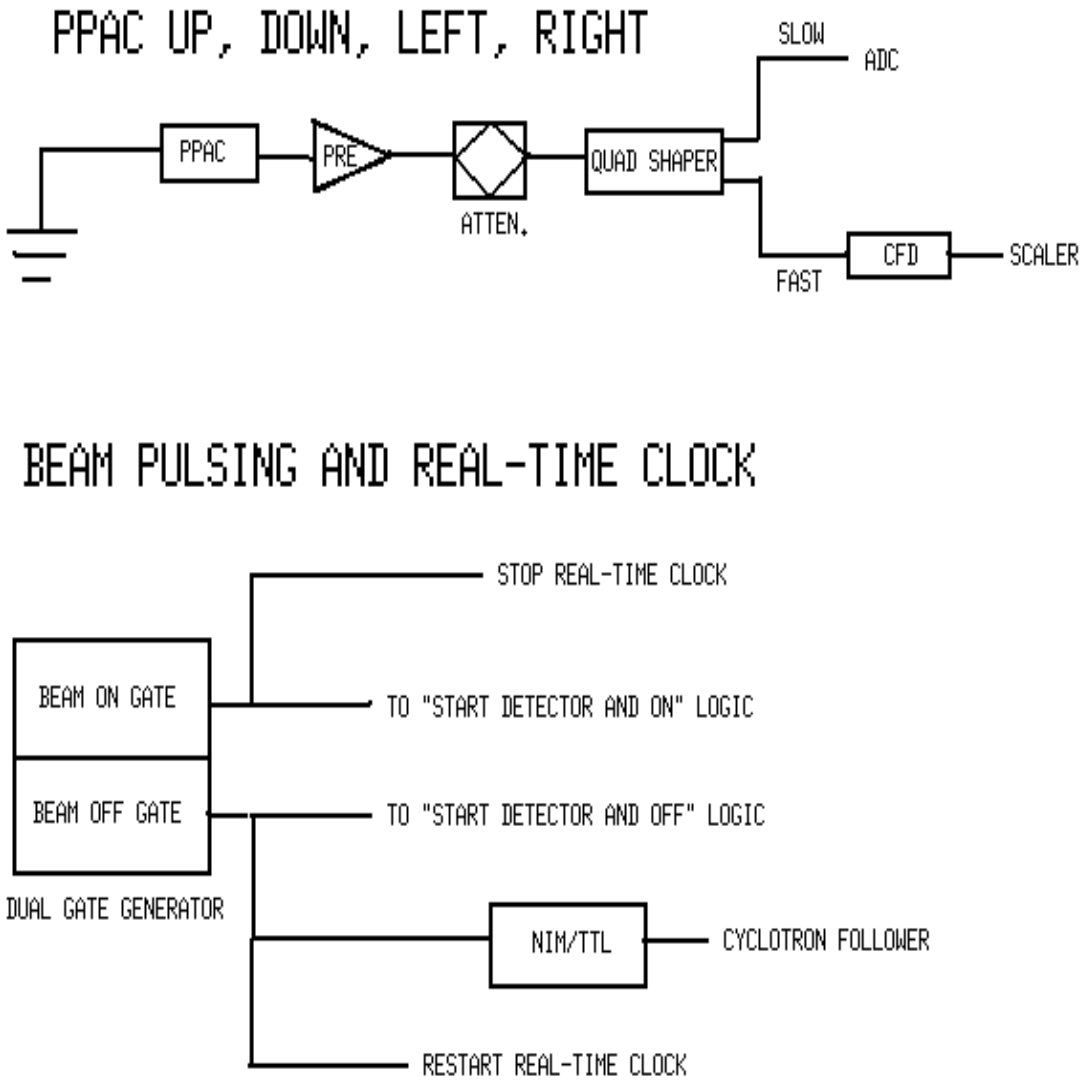

Figure 6 Electronics diagrams for the PPAC beam diagnostic elements and the beam pulsing / real-time clock set-up.

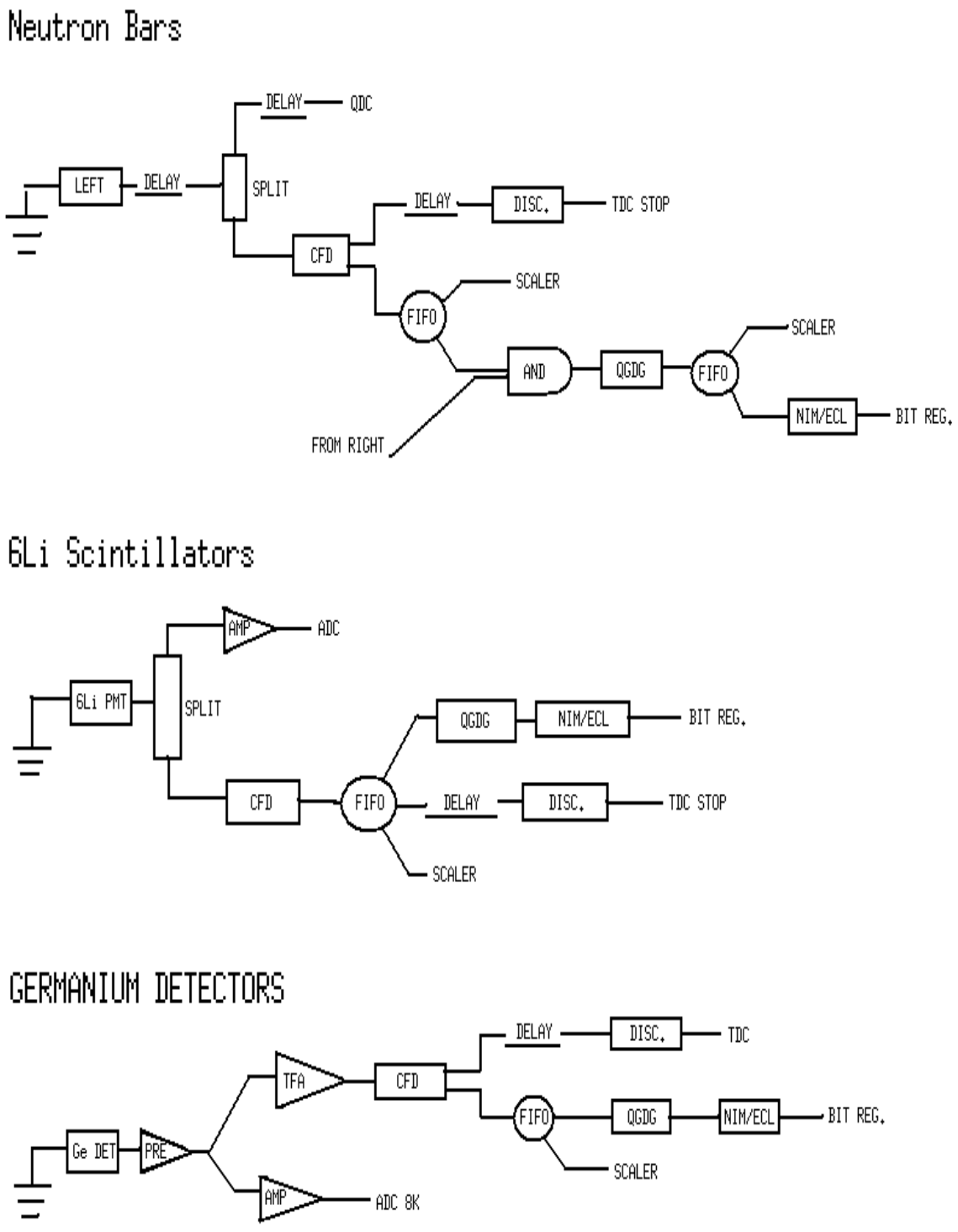

Figure 7 Electronics diagrams for the neutron bar array, ^{6}Li glass scintillators and germanium detectors.

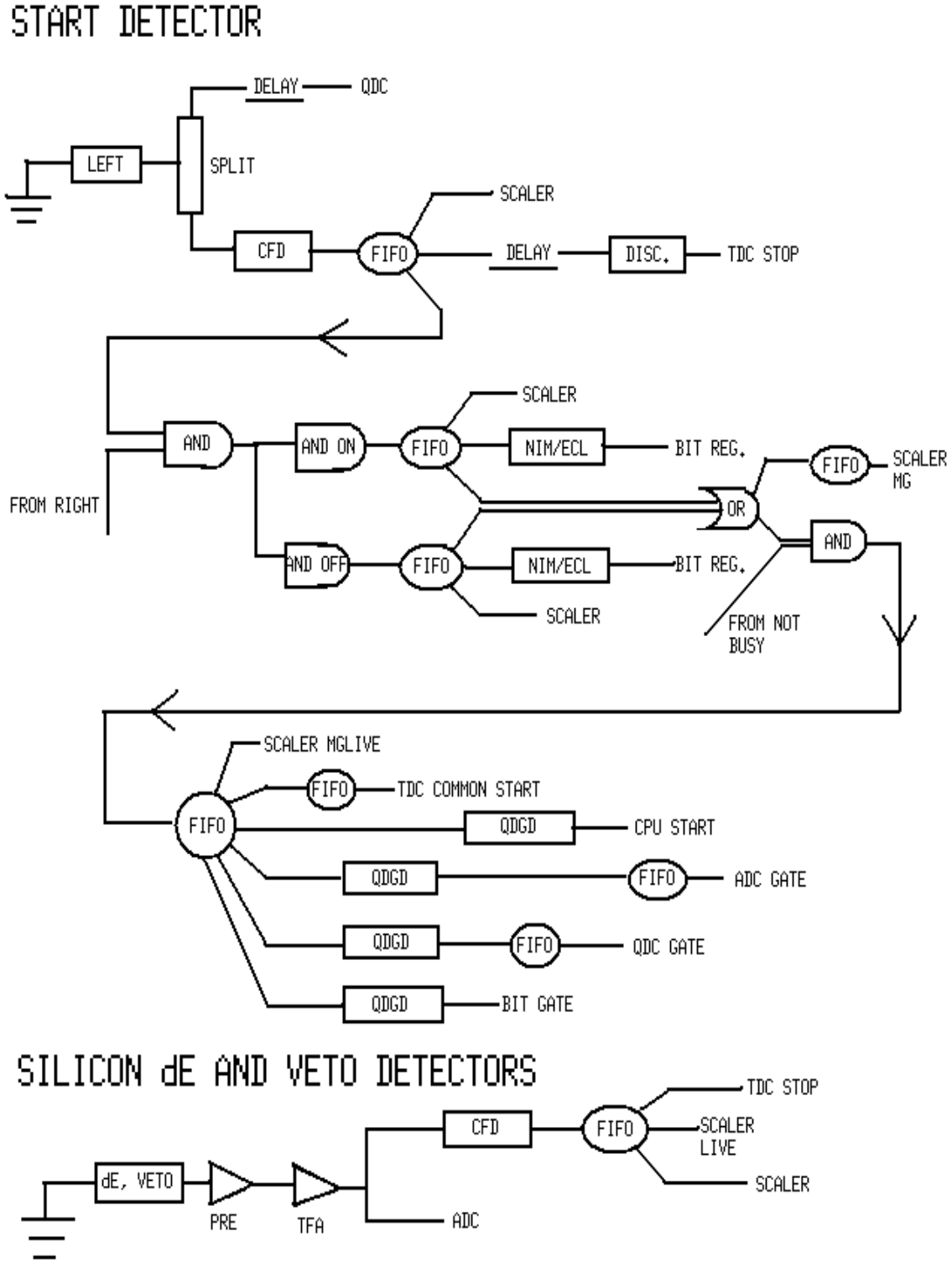

Figure 8 Electronics diagrams for the START detector and the silicon elements of the implantation system.

During beam tuning, the purity of the secondary product of interest is determined by monitoring both the fragment TOF through the separator, and the energy loss of the fragments in two silicon PIN detectors (typically 300 microns thick). The optimum settings are selected for such variables as the momentum acceptance of the spectrometer, the width and breadth of the momentum slits, the thickness of the achromatic wedge, the thickness of the production target and, occasionally, the composition of the target itself. Prior to transmitting the secondary beam to the desired experimental vault, a purity run is performed and the data stored for later reference.

For this experiment, the secondary beams were also monitored for purity at the end-station using the implantation system. The yield and composition of the secondary beam entering the vault is determined by the dE detector and the RF time-of-flight from the cyclotron while the yield and composition of the beam actually implanted into the start detector is determined from the dE vs. RF time-of-flight vetoed by the second silicon detector located downstream of the implantation scintillator. The results of the purity analysis for both the spectrometer analysis and end-station response is shown in table 3 for the four secondary beams of ^{16}C, ^{17}N, ^{19}N, and ^{20}N.

Table 3 Beam purity at the A1200 focal plane and the experimental end-station for those secondary nuclides isolated in this experiment.

SECONDARY BEAM	A1200 % PURE	IMPLANTED % PURE	CONTAMINANT	FRACTION %
^{16}C	99.3 (9)	99.70(6)	^{19}N, ^{18}N	0.7
^{17}N	>99.9	99.75(4)	N/A	N/A
^{19}N	99.5(10)	99.5(1)	^{17}C	0.5
^{20}N	98.8(17)	94.4(21)	^{18}C	1.1

From the data collected it is clear that the calibration beams of ^{16}C and ^{17}N, as well as the ^{19}N nuclide of interest, are better than 99% pure, while the secondary ^{20}N beam is about 95% pure. The lower purity of the ^{20}N beam is not unexpected due to the nature of the process through which ^{20}N is produced from a primary beam of ^{22}Ne. The reaction required a nucleon transfer or a charge exchange with the target material and hence the momentum distribution of this particular isotope covers a larger range. As a consequence, there is a greater probability of momentum overlap with other secondary products and thus the purity is reduced relative to the fragmentation products.

CHAPTER 3

EXPERIMENTAL RESULTS

3.1 HALF LIFE MEASUREMENT OF ^{19}N

The first priority in the experimental study of ^{19}N was to determine the half-life of the nuclide. Due to the high secondary yield of ^{19}N the data acquisition experienced a high degree of dead time. To minimize the contribution of this effect to the half-life determination, the primary ^{22}Ne beam was attenuated by a factor of about 30 during the run in which the half-life was measured.

The beta decay of ^{19}N populates states either in ^{19}O or ^{18}O depending on whether the exit channel is pure beta or delayed neutron emission. As such, the half-life fit to the recorded data must include a term for the decay of ^{19}O. Fortunately, the half-life of ^{19}O (26.9 seconds) is not only well established [] but is also roughly two orders of magnitude longer than the ^{19}N parent. This large difference, taken together with the fact that the total time of the half-life run was much longer than either half-life (~2 hours), permits a simplifying assumption where the two decays can be treated as independent quantities and the feeding term characteristic of secular decay modes may be eliminated.

The time sequence for the pulsing of the primary beam during the half-life run was set such that the beam-on period (implantation) was one second and the beam-off period (data acquisition) was three seconds. The half-life determination was made on the basis of the spectrum collected as a function of the real-time clock (Ortec model

RC014) during the beam-off periods. The full scale time of the clock was set to sixteen seconds.

The delayed neutron daughter, ^{18}O is stable and therefore a secular component for this decay is not necessary. Figure 9 shows the half-life fit to the data collected in the implantation scintillator for the decay of ^{19}N. Shown are the raw data, the ^{19}N component, the background due to ^{19}O, and the aggregate fit to the spectrum. The result of the fit indicates that the half-life of ^{19}N is 299 ±3 ±16 milliseconds. This result is in close agreement with the result reported in reference [].

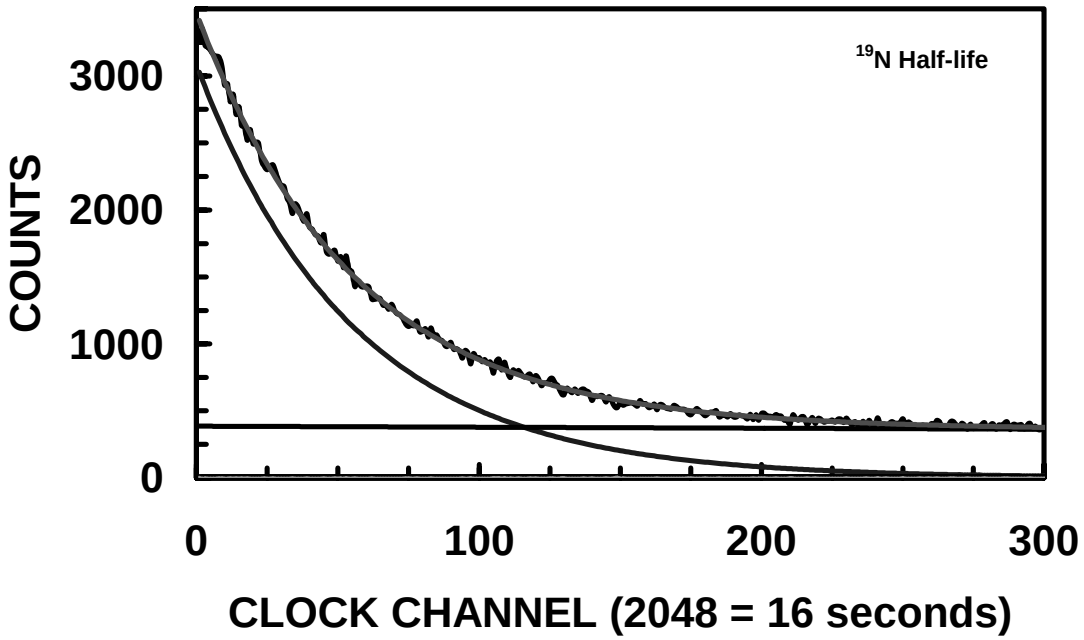

Figure 9 Fit to the half-life spectrum of ^{19}N. Shown are the raw data and background term (black), the ^{19}N component (blue) and the aggregate fit to the data (red).

3.2 HALF LIFE MEASUREMENT OF ^{20}N

The production rate of ^{20}N from the primary ^{22}Ne beam was orders of magnitude lower than that realized in the ^{19}N experiment. As a result, there was little or no dead

time associated with monitoring the decay of ^{20}N. The half-life fit included a term for the decay of both ^{20}O and ^{20}F, the daughter and granddaughter, but once again these half-lives are orders of magnitude longer than that of ^{20}N – permitting the same simplifying assumption as with the ^{19}N case.

During the ^{20}N runs, the beam-off time (where the real-time clock is active) was changed from 0.8 seconds to 0.375 seconds to improve the efficiency for recording ^{20}N events. Both series, long and short respectively, permit half-life determinations for ^{20}N. Figure 10 shows the fit to the long beam off data with the ^{20}N component, the sum of the daughter contributions and the aggregate fit to the data.

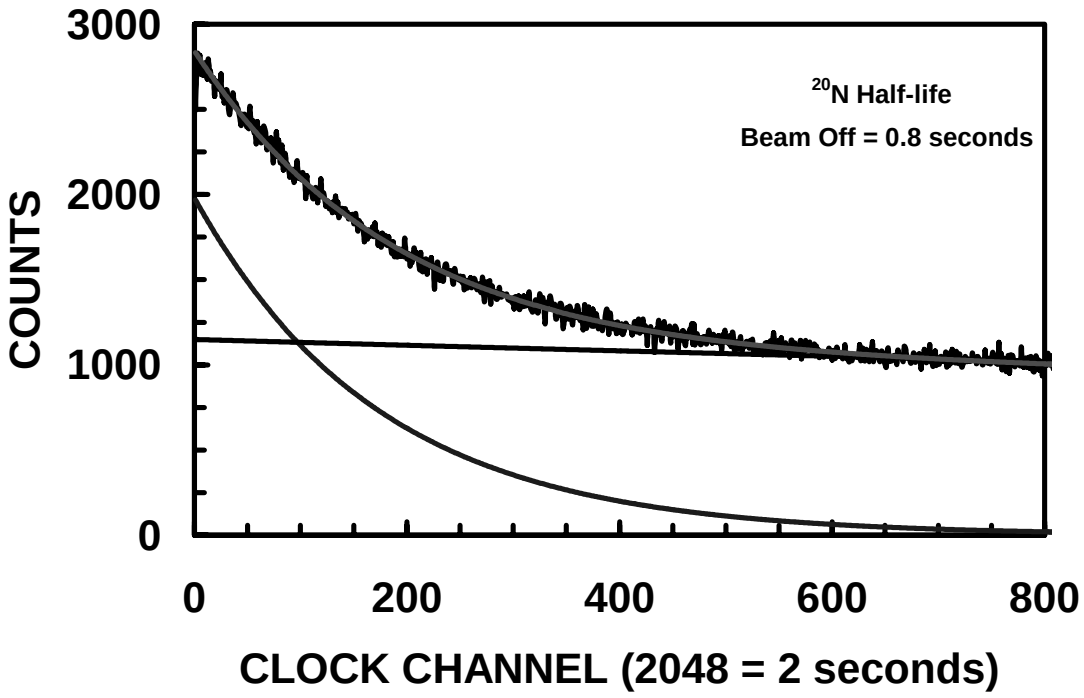

Figure 10 Half-life fit for the ^{20}N decay data recorded by the implantation scintillator and the real-time clock. This figure is the fit to the ^{20}N decay measured with a beam off time of 0.8 seconds.

The results of the long and short beam-off time data for the half-life of ^{20}N are 118 ±6 ±10 and 124 ±7 ±10 milliseconds, respectively. These results are in reasonably good agreement with the previously reported measurements in the literature [].

3.3 TOTAL NUMBER OF EVENTS

The total number of decay events for each nuclide was determined by the response of the implantation scintillator to beta particles. The total number of events is a necessary quantity to calculate the efficiency of the neutron and gamma-ray detectors and to determine the branching ratios for the ^{19}N and ^{20}N decay channels. The specific procedure used to solve for the total number of decays was to integrate the half-life spectrum collected for each nuclide.

3.3.1 DEAD TIME CONSIDERATIONS

Due to the high yield of secondary fragments, the data acquisition system experienced considerable dead-time. To account for the effect of dead-time analytically, the procedure outlined by Knoll[] and Leo[94Le] for non-paralyzable dead-time was employed. In this technique, the relationship between the actual and observed activity can be described by the equation:

$$m = n / (1 + n \tau)$$

Where m is the observed activity, n is the actual activity and τ is a dead-time related constant. It is noteworthy that the parameter, τ, will depend on the properties of the particular nuclide under scrutiny (half-life, implantation rate, daughter properties) thus τ is not general and must be solved for each secondary product of interest.

To elucidate an accurate value for the parameter, τ, subset half-life spectra were generated by applying tight gates around the peaks of the well-separated neutron

transitions recorded by the neutron bar array, and reflecting back onto the half-life spectrum. This protocol maximized the signal/background ratio and also ensured that the resultant half-life spectrum was as pure as possible – containing only one radioactive component. The caveat to this technique is that the dead-time formula is no longer strictly applicable. This is due to the fact that τ (though it is a constant over all channels) is dependent on the total instantaneous activity and not on any subset. However, the fraction of counts missed due to the computer being busy will be a constant at each channel for all subsets of the total half-life spectrum. Mathematically, the value of:

$$1 / (1 + n \tau)$$

will be a different constant at each channel for all gated and ungated half-life spectra. Clearly, n, the actual number of counts at any channel, varies among the gated subsets, thus the solution for τ will vary based on the inverse of n. However, since at channel zero (or any specific channel for that matter) the fraction of counts missed by the computer is the same for all subsets of the total half-life spectrum, the *product* of the value of τ with the *initial* activity will be the same for all subsets. For our purposes, it is more convenient to solve for the activity-times-τ constant ($A\tau con$) at channel zero, and for the initial gated activity for each subset of the total half-life histogram and compare across subsets for reliability.

For the calibration beams of ^{16}C and ^{17}N, the protocol was as follows: first, the neutron-gated half-life spectra were fit with MINUIT and MINOS where the decay constant was fixed to the known half-lives and $A\tau con$ and the initial activities were allowed to vary freely – as was the background. Second, the total half-life spectrum

was fit in MINUIT/MINOS in a similar way except that the value of Aτcon was restricted to be within the range defined by the solution of the fits to the gated spectra. Third, from the minimized fit, the total number of decays for each isotope was extracted. For the ^{19}N and ^{20}N nuclides, this same procedure was followed except that, in addition to fixing the half-lives to the literature or independently determined values, the procedure was repeated in its entirety with the half-lives permitted to vary freely in the minimization. As an example, figure 11 shows the aggregate delayed neutron spectrum of ^{16}C along with the neutron gates used to reflect back onto the half-life spectrum.

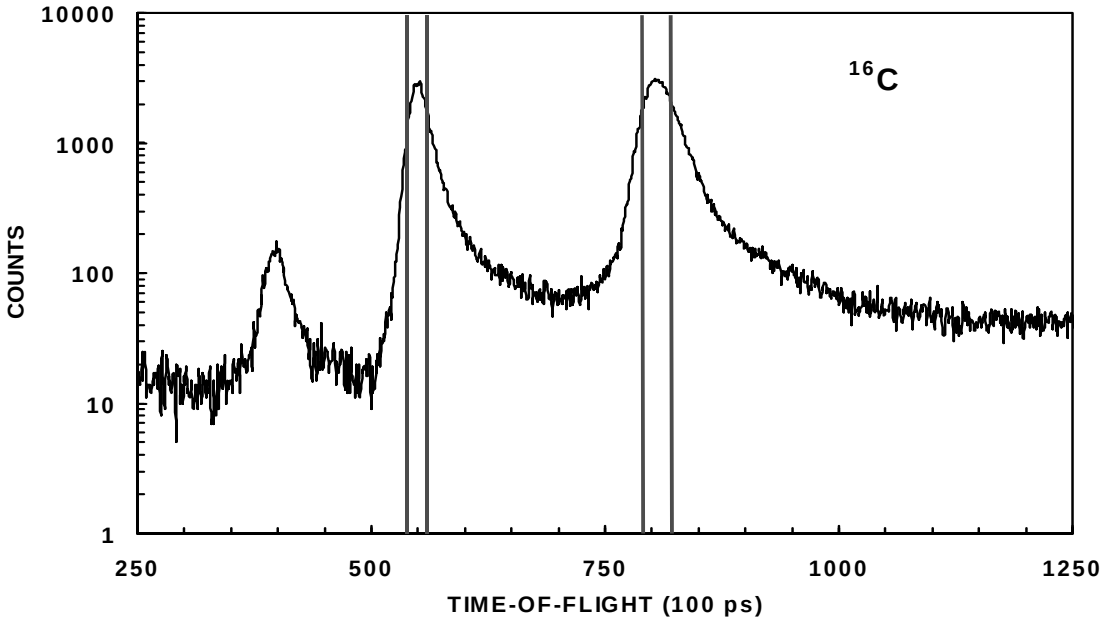

Figure 11 Aggregate delayed neutron spectrum collected by the neutron bar array during the decay of ^{16}C. Shown in red are the neutron gates used to reflect back onto the half-life spectrum for the dead-time analysis.

The gated half-life spectra were fit using the equation given by Knoll[] and Leo[] where the quantity n was of the form:

$$n = A_1 \, Exp[-\lambda_1 \, CH] + A_2 \, Exp[-\lambda_2 \, CH] + constant$$

where λ_1 was fixed to the known decay constant of ^{16}C in inverse channels, A_1 is the initial activity of ^{16}C in counts/channel, A_2 and λ_2 were parameters included to allow for the possibility of a second radioactive component, and CH is the channel of the half-life spectrum. In addition to these parameters, the value of the total initial activity times the dead-time parameter τ (Aτcon) was allowed to vary freely for each gated spectrum. Figure 12 shows the neutron-gated half-life spectra and the best-fit curves to those data as determined in MINUIT/MINOS.

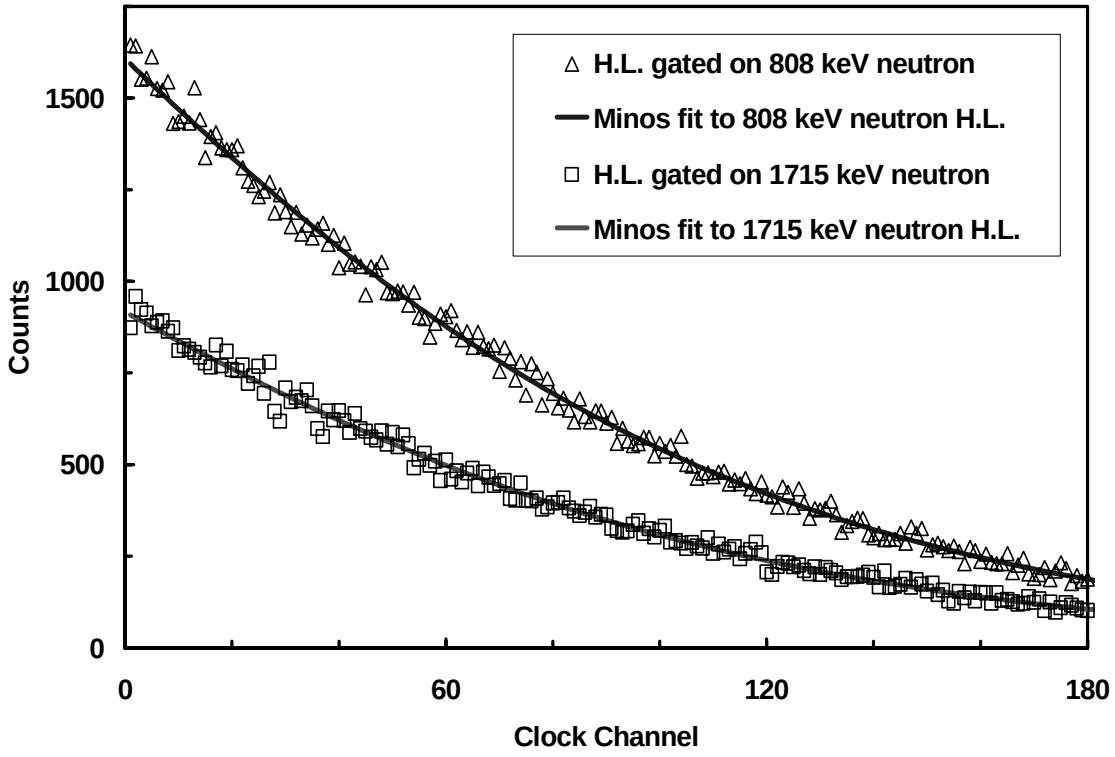

Figure 12 Best fit curves to the neutron-gated half-life spectra of ^{16}C. The data were minimized on the basis of the reduced chi-squared values as calculated in the MINUIT/MINOS package.

From these fits, the value of Aτcon is deduced to be 0.64(5) for the ^{16}C data, which is the weighted mean of the best-fit results for this parameter in MINUIT/MINOS. This value of Aτcon was input into the parameter list for the fit to

the total half-life spectrum and permitted to vary between the bounds defined by the one-sigma range. Again, the half-lives of ^{16}C and the beta daughter ^{16}N were fixed to their literature values, while the initial activities and a constant background were permitted to vary freely. Figure 13 shows the total half-life spectrum collected for the ^{16}C calibration runs and the best fit to those data using the procedure outlined above.

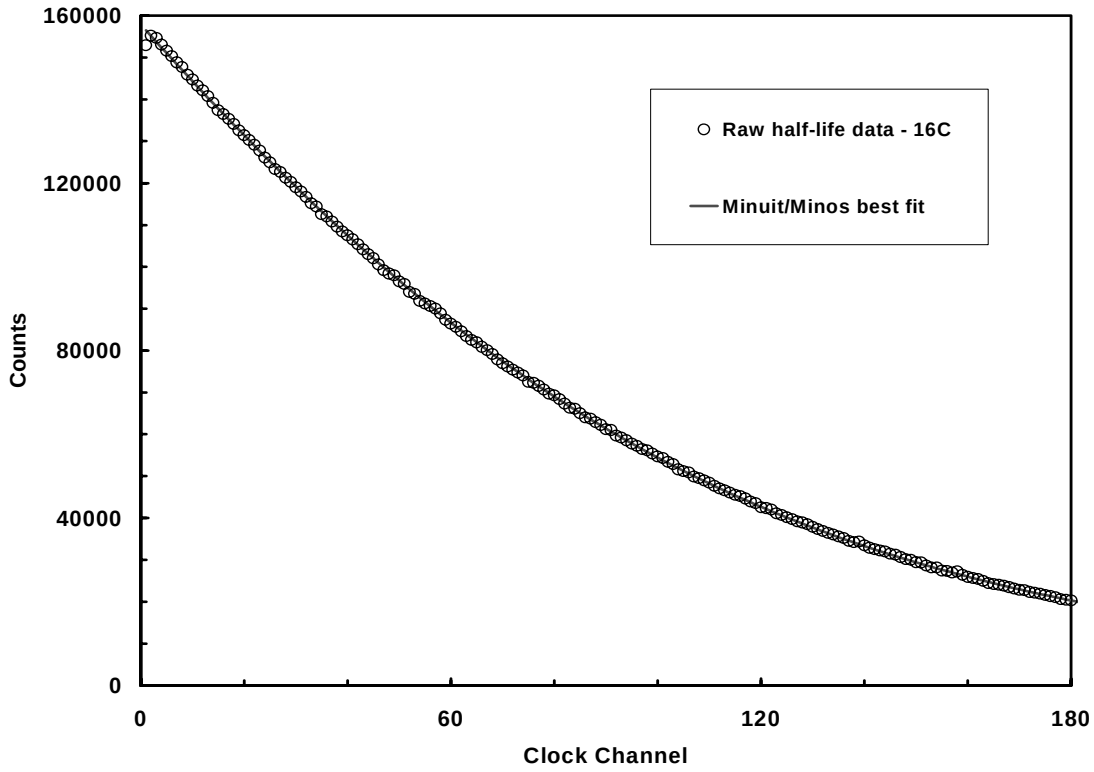

Figure 13 Fit to the full half-life spectrum recorded during the decay of ^{16}C by the implantation scintillator. The fit includes the correction for the dead time.

The best-fit value of Aτcon was 0.642(5), which is within the range defined by the gated data. Integrating the ^{16}C component with the dead time included leads to a total number of ^{16}C decays recorded in the experiment as 1.25(2) x 10^7 events.

3.4 SUMMARY

A similar procedure was followed for all isotopes of interest. In all cases, the reduced chi-squared of the fits was better than 1.15 and the value for Atcon derived

from the gated spectra reflected the value obtained for the total half-life data. Table 4 lists the final values for the total number of decays of each of the observed isotopes in this experiment.

Table 4 Total number of decays recorded by the implantation detector for each of the isotopes of interest.

Secondary Beam	Isotope	Total # of Decays
^{16}C	^{16}C	1.249(18) x 10^7
^{16}C	^{16}N	3.54(10) x 10^5
^{17}N	^{17}N	2.30(3) x 10^7
^{19}N	^{19}N	4.64(10) x 10^7
^{19}N	^{19}O	3.08(1) x 10^7
^{20}N	^{20}N	7.60(1) x 10^5

3.5 NEUTRON BAR ARRAY

The sixteen detectors of the neutron bar array were utilized to determine the energy of delayed neutrons emitted during the decay of the nuclides of interest and also the intensity or strength of the observed branches. Therefore, the individual detectors required calibration for both energy and detection efficiency. Since neutron energies were determined using a time-of-flight technique, the energy calibration is effectively a time calibration for the neutron bars. To calibrate the array in time, two techniques were combined: first, the TDC modules were slope calibrated using a precision time calibrator and second, the known delayed neutron lines of ^{16}C and ^{17}N were monitored to deduce the TDC offset. For the efficiency calibration, the decay of ^{16}C and ^{17}N provided transitions with known intensities over a range of neutron energies while

monte carlo simulations allow for the determination of the array's efficiency for higher energy neutrons. Each of these techniques is discussed in the following sections.

3.5.1 TIME CALIBRATION OF NEUTRON BAR ARRAY

The energy of neutrons emitted following the beta decay of ^{16}C, ^{17}N, ^{19}N, and ^{20}N were determined using a time-of-flight technique. As a consequence, it was desirable to find the time response of the time-to-digital-converters (TDCs) accurately and independent of the detectors' intrinsic responses. This was accomplished using a precision time calibrator (Ortec model 462) where the calibrator start was split and input to the implantation detector CFDs, while the calibrator stop was input, sequentially, to the CFD channel of each photomultiplier tube (PMT) in the experimental set-up. The period of the time calibrator was set to ten nanoseconds and the range was set to 320 nanoseconds. These were chosen knowing that the TDC modules' full scales were set by hand to be approximately 200 nanoseconds. Due to the fact that each bar of the neutron array contained two PMTs, the time response of both TDC channels was determined independently. A representative spectrum obtained using the time calibrator is shown in figure 14.

This technique was used to determine the slope of the time response of each photomultiplier tube utilized for time-of-flight measurements. In total there were 36 such PMTs – two for each of the sixteen neutron bars, one for each of the three ^{6}Li glass detectors and one for the standard detector. Table 5 gives the result of the TAC calibrator measurement for the slope of the PMTs' response as a function of detector.

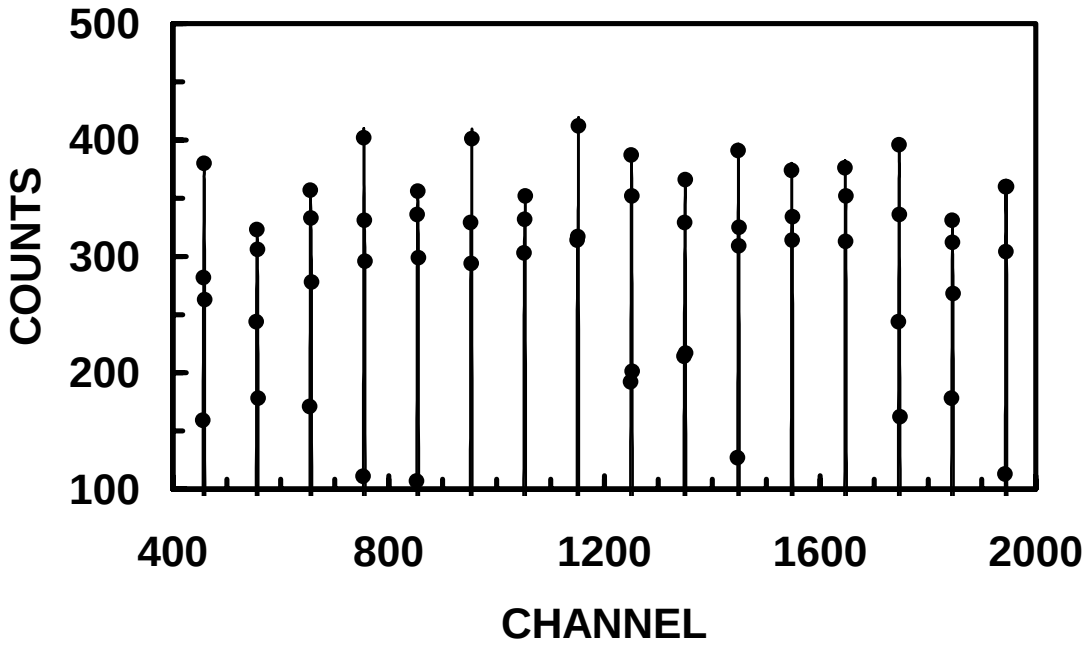

Figure 14 Representative spectrum collected by one of the neutron array bar phototubes using the precision time calibrator.

Table 5 PMT slopes for the neutron bar array as deduced from the precision time calibrator data.

PMT Designation	SLOPE Channels/ns	PMT Designation	SLOPE Channels/ns
BAR 01 R	9.960(4)	BAR 01 L	9.891(2)
BAR 02 R	9.899(5)	BAR 02 L	9.910(3)
BAR 03 R	10.002(1)	BAR 03 L	10.275(2)
BAR 04 R	10.278(3)	BAR 04 L	10.317(2)
BAR 05 R	10.506(2)	BAR 05 L	10.541(3)
BAR 06 R	10.354(3)	BAR 06 L	10.376(2)
BAR 07 R	10.357(4)	BAR 07 L	10.511(5)
BAR 08 R	10.300(4)	BAR 08 L	10.262(4)
BAR 09 R	10.313(2)	BAR 09 L	10.133(2)
BAR 10 R	10.317(3)	BAR 10 L	10.054(4)
BAR 11 R	10.253(3)	BAR 11 L	10.230(2)
BAR 12 R	10.603(5)	BAR 12 L	10.601(3)
BAR 13 R	10.609(4)	BAR 13 L	10.611(5)
BAR 14 R	10.571(3)	BAR 14 L	10.553(4)
BAR 15 R	10.578(4)	BAR 15 L	10.611(3)
BAR 16 R	10.336(4)	BAR 16 L	10.766(4)

The slopes determined by this method were incorporated into pseudo parameters within the SARA analysis code. The event time for a detected neutron in one of the array bars was defined as the average TDC channel recorded by the two phototubes of each array bar relative to the start signal of the implantation detector. The incorporation of the slopes into the pseudo code results in a histogram for each bar where the channels reflect a time duration of 100 picoseconds.

From these histograms having slopes of 100ps per channel, the energy/time response of the array bars was determined, on-line, by observing the delayed neutron emission from known sources. The decay of ^{16}C and ^{17}N are known to exhibit beta delayed neutron emission. The energies of the delayed neutrons emitted from these sources serve as useful on-line calibration beams for the neutron bar array. Table (*) gives the delayed neutron lines from these sources and the reference from which they are drawn.

Table 6 Calibration delayed neutrons of ^{16}C and ^{17}N given by energy and branching ratio.

SOURCE	ENERGY CM keV	ENERGY LAB keV	INTENSITY Percent	REFERENCE
^{17}N	407.6	384	38.0 (13)	
^{17}N	1245.4	1172	50.1 (13)	
^{17}N	1808.2	1702	6.9 (5)	
^{16}C	859	808	84.4 (17)	
^{16}C	1829	1715	15.6 (17)	

Secondary beams of ^{16}C and ^{17}N were generated in a manner completely analogous with that described in section (*) and monitored under experimental conditions identical to those of the ^{19}N and ^{20}N runs. The exception being that the beam

pulsing sequence was adjusted according to the half-lives of the respective nuclides. The spectra collected for ^{16}C and ^{17}N delayed neutrons were analyzed on a bar-by-bar basis to determine the peaks' centroids as a function of neutron energy.

To determine the centroid of the calibration peaks, the slope-adjusted spectra were fit to functional forms containing peak and background components. The peak shape was approximated by a combination of gaussian and Breit-Wigner functions. Below the centroid the shape of the peak is gaussian while at channels above the centroid the shape is Breit-Wigner. This functional form proved to be the most reliable estimation of the response function of the array detectors. The background term was simply a broad asymmetric gaussian plus a constant to account for random events and potential neutron scattering from the end-station environment.

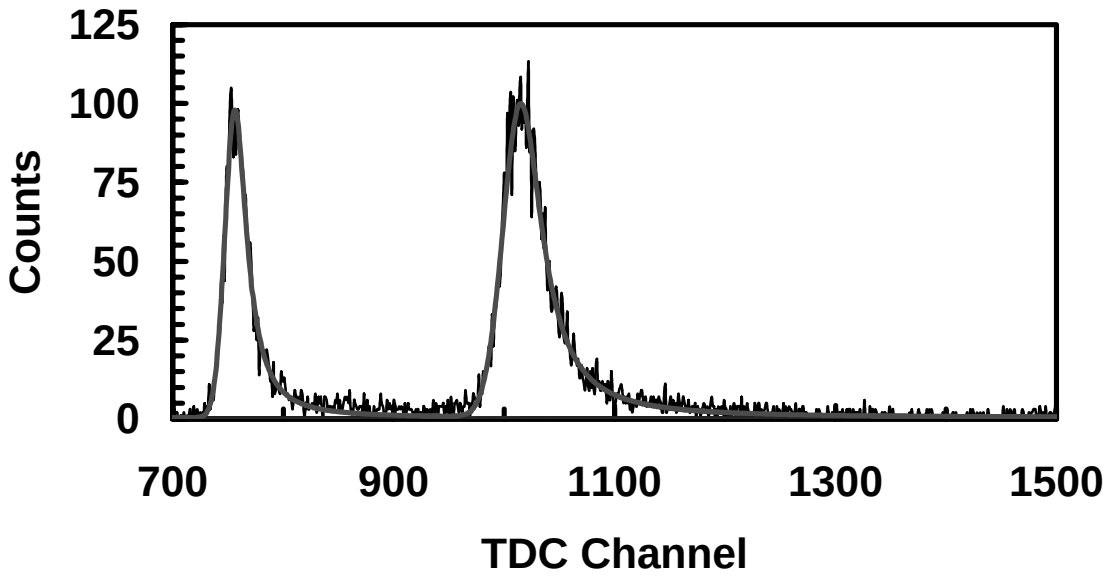

Figure 15 Delayed neutron spectrum collected by one of the array bars during the decay of the ^{16}C calibration beam.

As an example, figure 15 shows the delayed neutron spectrum collected in one of the array bars during the decay of ^{16}C. The fit to the data is indicated in red where

the best fit was determined by minimizing the total Chi-squared using the program MINUIT [] from the Cern library. Typically, the reduced Chi-squared was between 0.9 and 1.2 for the fits to the individual bars for both the ^{16}C and ^{17}N data.

Table 7 gives the results of the fits to all of the calibration neutron peaks. Tabulated are the centroids of the calibration lines along with the uncertainty in the fit (in TDC channels) as a function of delayed neutron energy.

Table 7 Centroid channels of the neutron peaks utilized in the calibration of the neutron bar array.

Array Bar	1715 keV peak Centroid	808 keV peak Centroid	1702 keV peak Centroid	1172 keV peak Centroid
1	754.9	1009.8	759.1	874.7
2	753.7	1011.7	757.5	874.6
3	776.8	1034.3	781.6	898.5
4	745.9	1005.6	749.0	864.5
5	814.4	1081.2	819.7	937.9
6	796.6	1060.3	803.0	919.9
7	810.6	1069.0	816.6	931.8
8	756.4	1013.5	760.4	877.5
9	737.1	997.3	740.4	858.5
10	752.1	1009.8	757.5	873.1
11	718.7	975.3	725.5	838.3
12	776.7	1036.2	782.0	897.5
13	748.1	1004.4	751.7	868.0
14	732.5	989.1	735.4	853.4
15	729.1	981.9	732.7	851.4
16	773.3	1033.4	778.1	895.1

Unfortunately the individual array bars were not efficient enough at low energy to detect the 384 keV neutron from the decay of ^{17}N. However, in addition to the known

neutron transitions, the plastic bars were able to record events due to the beta particles. These peaks provide additional calibration points in the time spectrum of each array detector. Table 8 gives the MINUIT result for the centroid of the prompt beta transition on a bar-by-bar basis.

Table 8 Centroid channels of the prompt beta peaks utilized in the calibration of the neutron bar array.

Array Bar	β-Prompt ^{16}C Centroid	β-Prompt ^{17}N Centroid
1	234.0	234.6
2	232.6	233.4
3	256.2	257.9
4	226.3	226.6
5	294.0	295.2
6	276.2	277.3
7	292.4	293.0
8	238.7	239.4
9	221.4	220.8
10	233.9	234.5
11	200.2	200.6
12	258.3	258.5
13	229.4	229.7
14	210.2	210.8
15	201.8	202.3
16	247.7	248.7

To calibrate the individual detectors, the neutron and beta energies were converted into velocities with the dimension of metres/(100 picoseconds). The unusual unit was chosen to take advantage of the known 100 picosecond wide bins of the PMT

slope corrected histograms. For the neutrons, the velocity was determined from the general equation:

$$E = \tfrac{1}{2} mv^2$$

where E is the laboratory energy listed in table 6. For the neutrons, no relativistic correction was included as the energies were low enough to treat them classically. For the β-particles, the energy used to calculate the velocity was for the most probable energy in the distribution. This was taken to be 0.33 of the β-decay energy - yielding most probable β energies of 1.265 and 1.522 MeV for ^{17}N and ^{16}C, respectively. These were deduced by weighting the known decay branches by their normalized probability and summing over the possible transitions. The calculated velocity of the representative β particles, unlike the neutron case, included a relativistic correction.

The inverse of the calculated particle velocity was fit to the observed histogram channel using the general form:

$$1/v \;=\; 1/d \cdot (TDCChannel - Offset)$$

where v is the velocity (m/100ps), d is the distance between the position of the source activity and the array bar (metres), and the offset is measured in channels or 100ps. Expanding the equation leads to a simple linear relationship:

$$1/v \;=\; 1/d \cdot TDCChannel - 1/d \cdot Offset$$

or equivalently:

$$y \;=\; M \cdot x + B$$

By way of example, table 9 lists the particle energies, their calculated velocities, and respective peak centroids for the determination of the parameters M and B (leading to d and Offset) for one of the sixteen array bars.

Table 9 Parameters derived from the delayed neutron energies and their centroid channels necessary to calibrate the neutron bars.

Particle Type	Energy MeV	Velocity m/100ps	1/v 100ps/m	Peak Centroid Channel
Neutron	1.702	0.00180	554.2	759.1
Neutron	1.172	0.00149	667.8	874.7
Neutron	1.715	0.00181	552.1	754.9
Neutron	0.808	0.00124	804.3	1009.8
^{16}C β	1.522	0.02823	35.4	234.0
^{17}N β	1.265	0.02742	36.5	234.6

These data, specifically columns four and five of table (above) were fit to a line yielding best fit values for M and B along with their associated interpolation errors. Figure 16 shows the data and the fit for neutron bar number one where the centroid is plotted on the X-axis and the inverse velocity is plotted on the Y-axis.

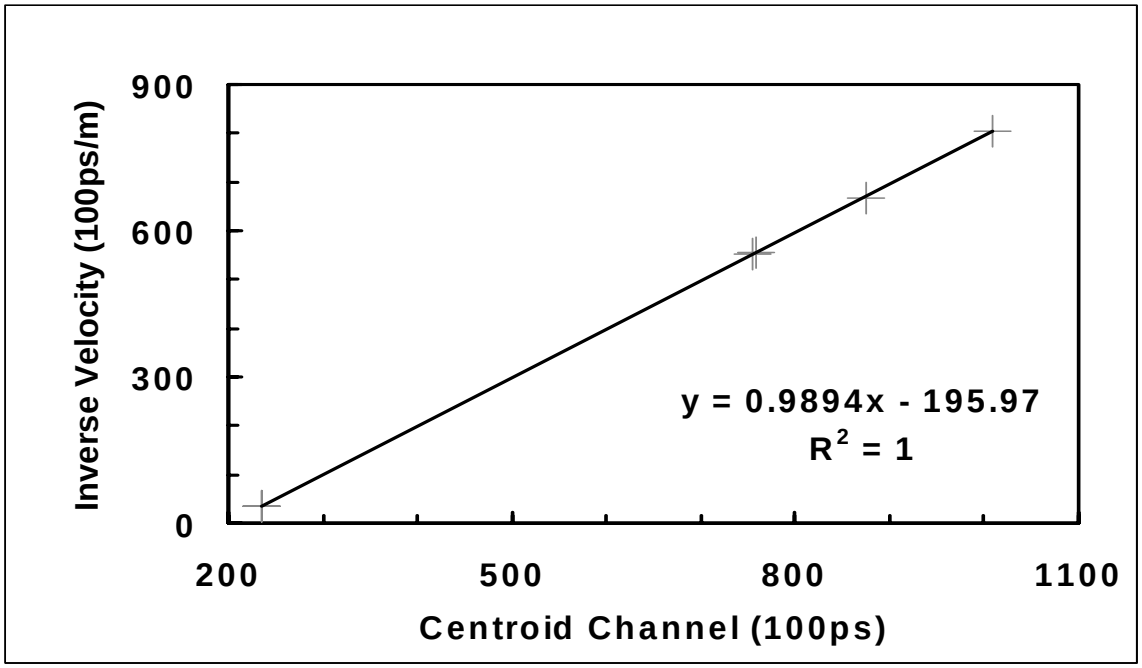

Figure 16 Plot of inverse velocity versus centroid channel and the best fit straight line to the data.

From the best-fit values of M and B determined on a bar-by-bar basis, values for the parameters d and Offset can be calculated. When known, the constants d and Offset can be incorporated into new SARA pseudo parameters that will result in histograms that have normalized the time-of-flight to a flight path of one metre. The channel number will be a measure of the inverse velocity in units of (100ps/metre) or, equivalently, time-of-flight in hundreds of picoseconds. What is perhaps most important is that, following this transformation, the time-of-flight spectra of the individual array bars are gain matched, if you will, which allows for a cumulative neutron TOF spectrum to be recorded. This is advantageous generally, but in particular it ensures that the experiment as a whole is as sensitive to lower-energy delayed neutrons as possible. Table 10 lists the values of the best-fit parameters and the calculated values of d and Offset for each of the sixteen array bars.

3.5.2 NEUTRON BAR ARRAY – EFFICIENCY CALIBRATION

The time calibrated spectra of the individual bars were summed to generate the final delayed neutron spectra with the caveat that bar #15 was excluded due to a failure of one of the phototubes during the experiment. The summed spectra collected for each of the calibration isotopes are shown in figures 17 and 18. Included in the figures are the raw data, the individual peak contributions (blue), the two-component background (black), and the aggregate fit to the data (red). The best fit is the minimum in the total χ^2 which was determined using the minimization package MINUIT. The error in the fit for each parameter was calculated within the MINUIT routine using the associated MINOS package that removes the parameter correlation and hence delivers a more true evaluation of the individual parameter errors.

Table 10 Summary of the calibration fits for each of the array bars. The parameters d and Offset are generated from the M and B results.

Array Bar	M Value (from fit)	B value (from fit)	Distance d metres	Offset Channels
1	0.989(2)	-196(1)	1.011(2)	198(1)
2	0.987(2)	-193(1)	1.013(2)	196(1)
3	0.988(2)	-217(2)	1.012(2)	220(2)
4	0.989(2)	-187(1)	1.011(2)	189(2)
5	0.981(4)	-252(3)	1.019(4)	257(4)
6	0.983(3)	-235(3)	1.018(4)	239(3)
7	0.990(2)	-254(2)	1.010(2)	256(2)
8	0.992(3)	-200(2)	1.008(3)	202(2)
9	0.992(5)	-181(3)	1.008(5)	183(3)
10	0.991(2)	-196(1)	1.009(2)	197(2)
11	0.991(2)	-163(1)	1.009(2)	164(1)
12	0.989(2)	-219(2)	1.011(2)	221(2)
13	0.992(1)	-192(1)	1.008(1)	193(1)
14	0.986(2)	-172(1)	1.014(2)	174(1)
15	0.980(4)	-162(3)	1.020(4)	165(3)
16	0.978(2)	-206(1)	1.022(2)	211(1)

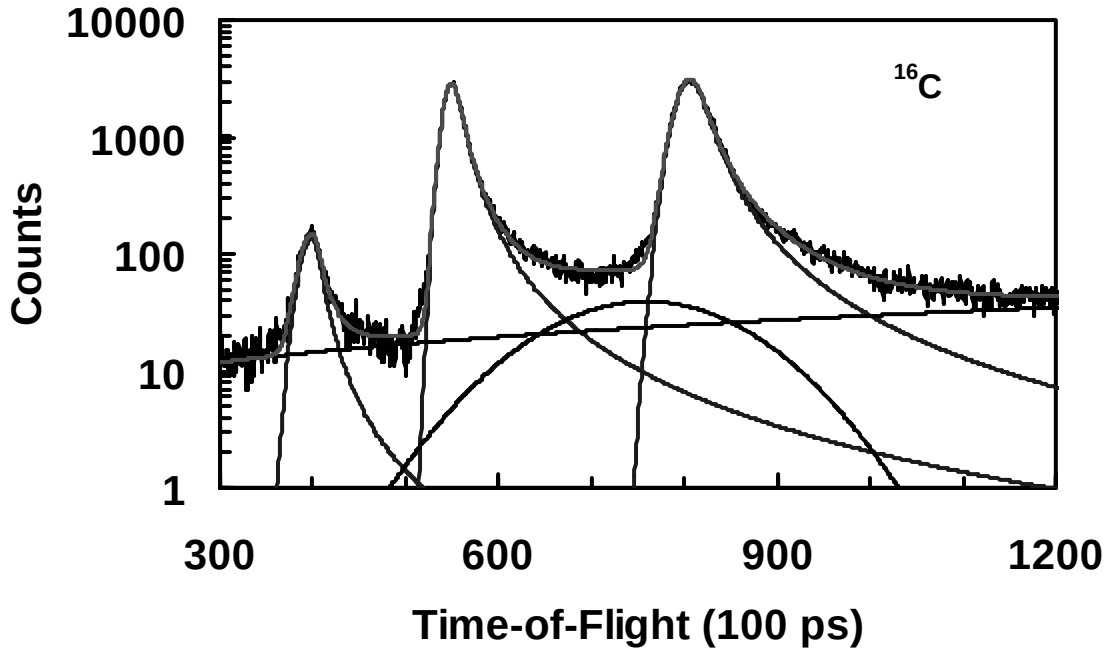

Figure 17 TOF spectrum of delayed neutrons detected by the neutron bar array for the decay of ^{16}C showing the individual peaks, background and cumulative fit to the data.

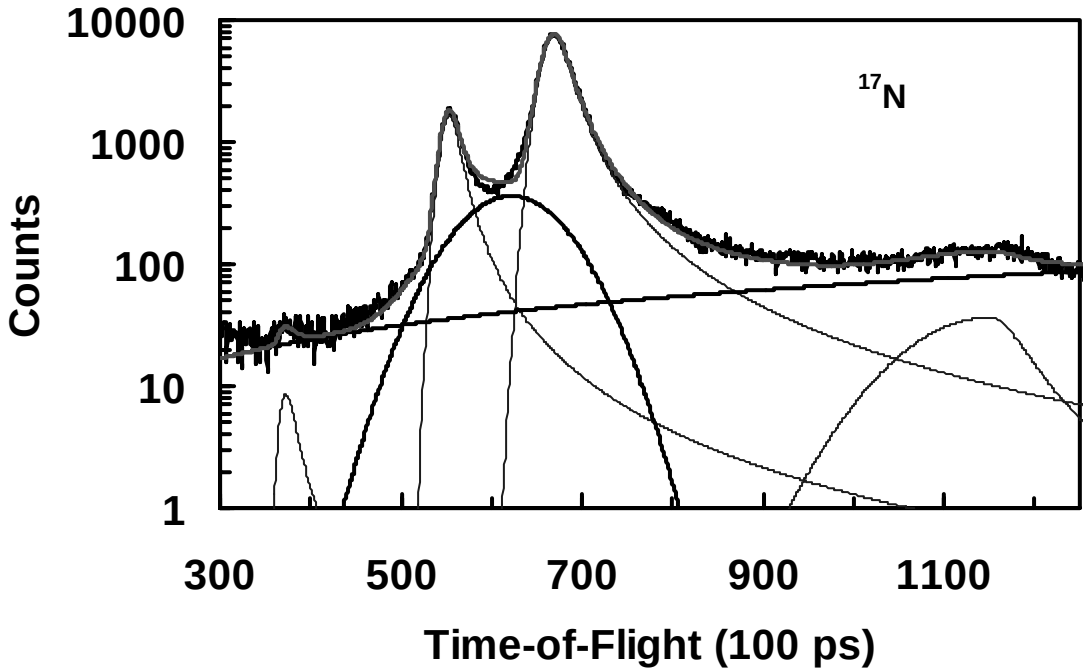

Figure 18 TOF spectrum for neutrons detected by the neutron array during the decay of ^{17}N. The plot shows the individual peaks, background and cumulative fit to the data.

To generate an efficiency calibration curve, the known transitions of the calibration isotopes (^{16}C, ^{17}N) were integrated. Knowing the individual branching ratios for the delayed neutron transitions [] and the total number of parent decays, several calibration points for the total efficiency were acquired. For higher energy neutrons, the efficiency of the array has been approximated using a monte-carlo method []. Table 11 gives the calculated efficiency points from the on-line data and figure 19 shows the final efficiency calibration curve including the monte-carlo data and the spline fit. The error in the efficiency determination has been shown to be about ten percent of the extracted value [93Ha].

Table 11 Data points used to generate and efficiency calibration for the neutron bar array. The monte-carlo points are from reference [].

Source	En (keV)	Branch (%)	Parent Decays	Peak Area	Efficiency Total
^{17}N	384	38.0 (13)	2.30(3)E7	6.1(5)E3	6.98(55)E-4
^{17}N	1172	50.1 (13)	2.30(3)E7	3.33(4)E5	2.89(10)E-2
^{17}N	1702	6.9 (5)	2.30(3)E7	5.07(32)E4	3.20(31)E-2
^{16}C	808	84.4 (17)	1.25(2)E7	1.50(3)E5	1.42(5)E-2
^{16}C	1715	15.6 (17)	1.25(2)E7	8.51(16)E4	4.37(49)E-2
Monte Carlo	1800	N/A	N/A	N/A	3.35(34)E-2
Monte Carlo	3000	N/A	N/A	N/A	3.16(32)E-2
Monte Carlo	4500	N/A	N/A	N/A	2.86(29)E-2

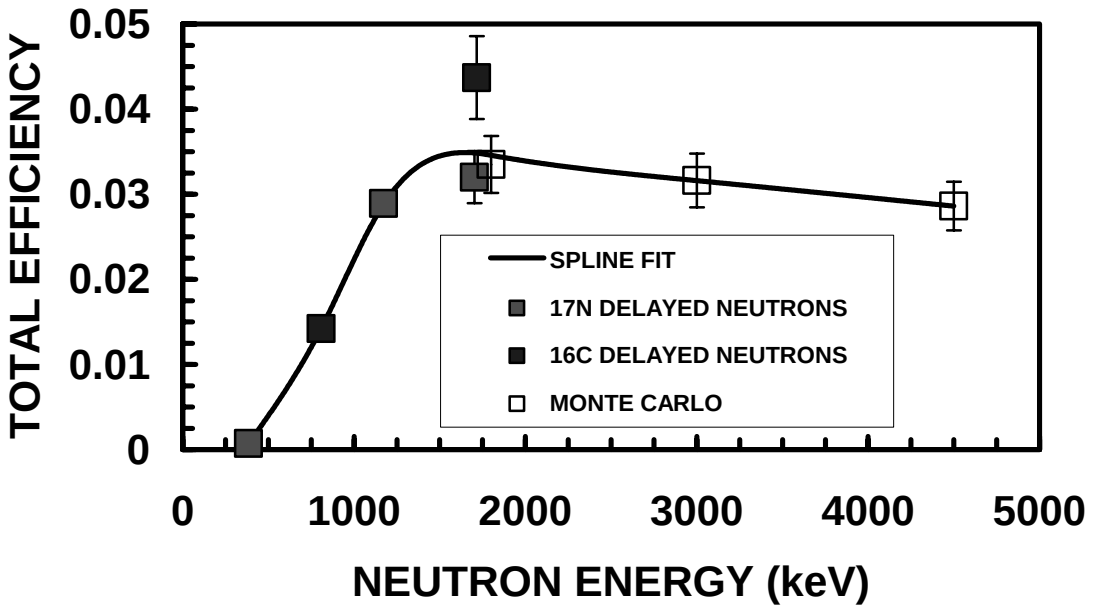

Figure 19 Calibration curve for the total efficiency determination of the neutron bar array as a function of incident neutron energy in the laboratory frame.

3.6 NEUTRON BAR RESULTS – ^{19}N AND ^{20}N

The delayed neutron spectra of the isotopes of interest (^{19}N, ^{20}N) were recorded under experimental conditions identical with those of the calibration beams of ^{16}C and ^{17}N. The spectra collected by the individual bars were summed to generate cumulative delayed neutron spectra suitable for integration. The raw data were fit to peaks having the same functional form as with the calibration spectra and were minimized using the MINUIT/MINOS package.

3.6.1 ^{19}N DELAYED NEUTRON SPECTRUM

Figure 20 shows the cumulative neutron TOF spectrum collected by the neutron bar array during the decay of ^{19}N. The background components of the fit are shown in black, the individual peaks are shown in blue, and the sum of the components is shown in red. The TOF scale is given in bins having 100 ps width.

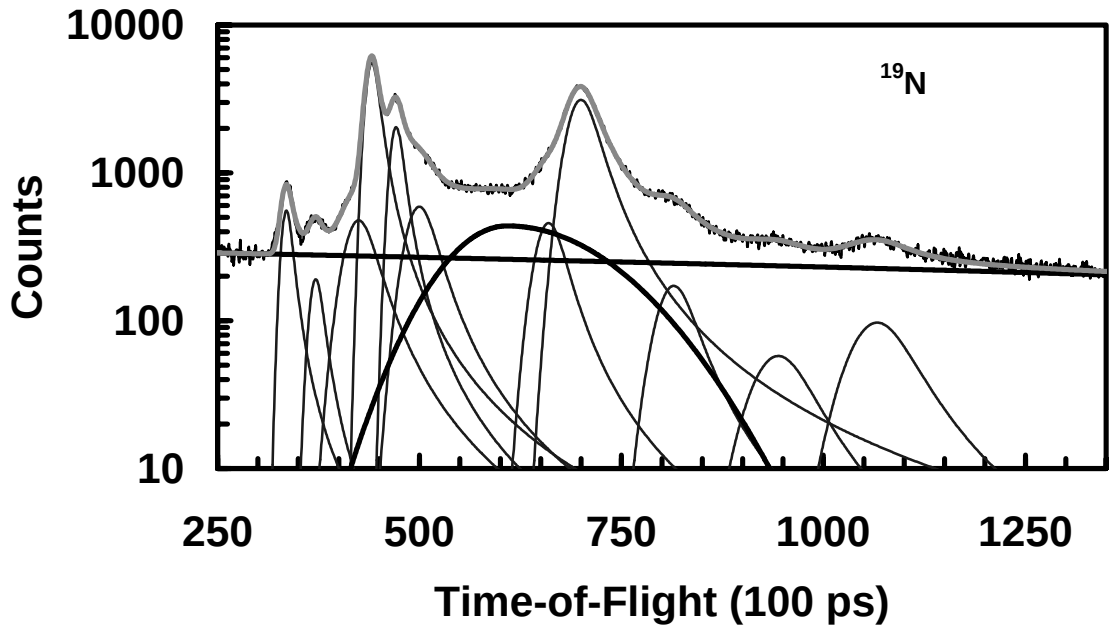

Figure 20 Delayed neutron time-of-flight spectrum collected by the neutron bar array during the decay of ^{19}N.

As is evidenced by the figure, the delayed neutron spectrum of ^{19}N is a rich one. The best-fit to the data indicates that there are some eleven delayed-neutron lines with eight of these being reasonably well-separated, and three appearing as shoulders on larger peaks. From the best-fit centroids and knowing the time of flight scale, the energy of the neutron lines may be calculated. Table 12 lists the peak centroids, and calculated delayed neutron energy in both the laboratory and center-of-mass reference frames.

From the integrated areas of the eleven observed neutron peaks, the total efficiency calibration, and the sum of the parent beta decays, the branching ratios of the transitions can be calculated. Table 13 lists the ^{19}N observed delayed neutrons by energy, the values of the parameters necessary for the branching ratio calculation, and the corresponding branching ratios.

Table 12 Delayed neutron lines observed during the decay of ^{19}N. The TOF is given along with the neutron energies in both the lab and center of mass frames.

Peak Designation	Time of Flight (100 ps)	Neutron Energy Lab. (MeV)	Neutron Energy C.o.M. (MeV)
1	335.24	4.65	4.91
2	371.55	3.79	4.00
3	424.68	2.90	3.06
4	441.01	2.69	2.84
5	471.07	2.36	2.49
6	499.75	2.09	2.21
7	659.86	1.20	1.27
8	699.93	1.07	1.13
9	814.76	0.79	0.83
10	944.24	0.59	0.62
11	1066.70	0.46	0.49

Table 13 Delayed neutron branching ratios for those neutron lines observed in the neutron bar array during the decay of ^{19}N.

Neutron Peak	E_n (MeV) CoM	Peak Area	Parent Decays	Total Efficiency	Branching Ratio (%)
1	4.91	1.19(3)E4	4.64(1)E7	2.85(29)E-2	0.90(10)
2	4.00	5.13(32)E3	4.64(1)E7	3.00(30)E-2	0.37(4)
3	3.06	2.91(36)E4	4.64(1)E7	3.18(32)E-2	1.97(32)
4	2.84	1.44(3)E5	4.64(1)E7	3.22(33)E-2	9.6(11)
5	2.49	5.34(12)E4	4.64(1)E7	3.29(33)E-2	3.5(4)
6	2.21	3.50(78)E4	4.64(1)E7	3.36(34)E-2	2.2(4)
7	1.27	2.60(62)E4	4.64(1)E7	2.96(30)E-2	1.9(2)
8	1.13	1.88(2)E5	4.64(1)E7	2.50(25)E-2	16.2(17)
9	0.83	1.25(7)E4	4.64(1)E7	1.33(14)E-2	2.0(3)
10	0.62	6.48(29)E3	4.64(1)E7	6.51(66)E-3	2.2(3)
11	0.49	1.14(4)E4	4.64(1)E7	2.84(29)E-3	8.7(10)

3.6.2 ^{20}N DELAYED NEUTRON SPECTRUM

The data collected by the neutron bar array during the decay of ^{20}N was summed in a manner consistent with the previously detailed analyses. Unfortunately, the production of ^{20}N from a primary beam of ^{22}Ne requires a particle transfer or charge-exchange mechanism rather than the more probable nucleon removal. As a result, the intensity of the ^{20}N secondary beam was dramatically reduced relative to the other secondary isotopes studied. Because of this reduction in intensity, the data collected by the neutron bar array was compressed by a factor of two to better examine the features of the plot and to improve the fits to the spectrum.

Once again, the individual bar data were summed to produce and aggregate delayed-neutron time-of-flight spectrum for the decay of ^{20}N. The time bins, in this case, had widths of 200 ps. Figure 21 is the aggregate neutron bar spectrum and shows the raw data, background terms (black), individual peaks (blue) and the cumulative fit to the spectrum (red). It is noted that this spectrum has the y-axis on a linear scale rather than on a logarithmic scale as for the previous spectra.

The cumulative fit from MINUIT supports a delayed neutron spectrum consisting of eight transitions. Six of these are well separated in energy while the other two appear as shoulders of larger peaks. From the bset-fit centroids, the energy of the delayed neutrons can be calculated knowing that each channel represents 200 ps in time. Table 14 lists the ^{20}N peak centroids, and the corresponding energies in both the laboratory and center of mass reference frames.

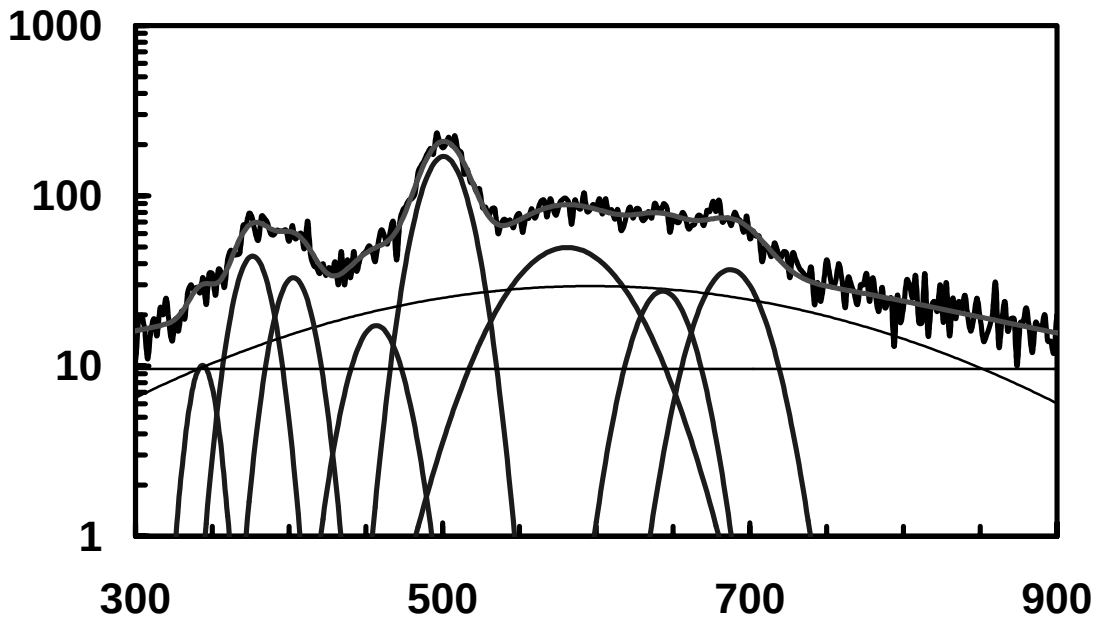

Figure 21 Delayed neutron spectrum recorded by the neutron array during the decay of ^{20}N. The data are compressed by two relative to the other isotopes of interest.

Table 14 Summary of delayed neutrons observed during the decay of ^{20}N. Listed are the centroid channels and the corresponding neutron energy in both the lab and center of mass frames.

Peak Designation	Centroid 1ch = 200 ps	Neutron Energy Laboratory (MeV)	Neutron Energy C.o.M. (MeV)
1	171.9	4.412	4.644
2	188.1	3.682	3.876
3	201.4	3.213	3.382
4	228.4	2.500	2.632
5	250.3	2.082	2.192
6	290.6	1.545	1.626
7	321.7	1.261	1.327
8	343.6	1.105	1.163

From the integrated peak areas, the measured number of parent ^{20}N decays, and the efficiency calibration, the branching ratio for each transition was calculated. Table 15 is a summary of the branching ratio calculation for ^{20}N delayed neutrons that includes the values of the parameters necessary to elucidate the decay strength.

Table 15 Calculated branching ratios for the delayed neutron lines observed by the neutron bar array during the decay of ^{20}N.

Neutron Peak	E_n (MeV) CoM	Peak Area	Parent Decays	Total Efficiency	Branching Ratio (%)
1	1.16	900(30)	7.6(1)E5	2.65E-02	4.5(5)
2	1.33	600(38)	7.6(1)E5	3.12E-02	2.5(3)
3	1.63	2200(57)	7.6(1)E5	3.47E-02	8.3(9)
4	2.19	3087(56)	7.6(1)E5	3.37E-02	12.1(13)
5	2.63	329(33)	7.6(1)E5	3.26E-02	1.3(2)
6	3.38	486(25)	7.6(1)E5	3.12E-02	2.1(3)
7	3.88	624(26)	7.6(1)E5	3.03E-02	2.7(3)
8	4.64	102(19)	7.6(1)E5	2.88E-02	0.5(1)

3.7 ^{6}Li INORGANIC SCINTILLATORS

In addition to the neutron bar array, the experimental set-up included three ^{6}Li glass scintillators to detect delayed neutron events. The TDC modules for these devices were calibrated in a manner completely analogous with the procedure outlined for the bars of the array. The slopes of the TDC channels were determined by the use of a precision time calibrator set to 10ns intervals and a 320ns range.

To complete the calibration, the decay of the isotopes ^{16}C and ^{17}N were monitored by the glass scintillators. Figures 22 and 23 show the spectra collected by one of the three ^{6}Li detectors (detector #3) in the time domain for each of the ^{16}C and ^{17}N calibration beams. Included in the plot is the best fit to the data assuming a

gaussian peak shape below the peak centroid and a briet-wigner shape above the centroid. The error bars are the statistical errors of the points only. It is noted that, due to the low total efficiency of the ^{6}Li devices, the spectra are compressed to seven bits to better illuminate the salient features of the plots.

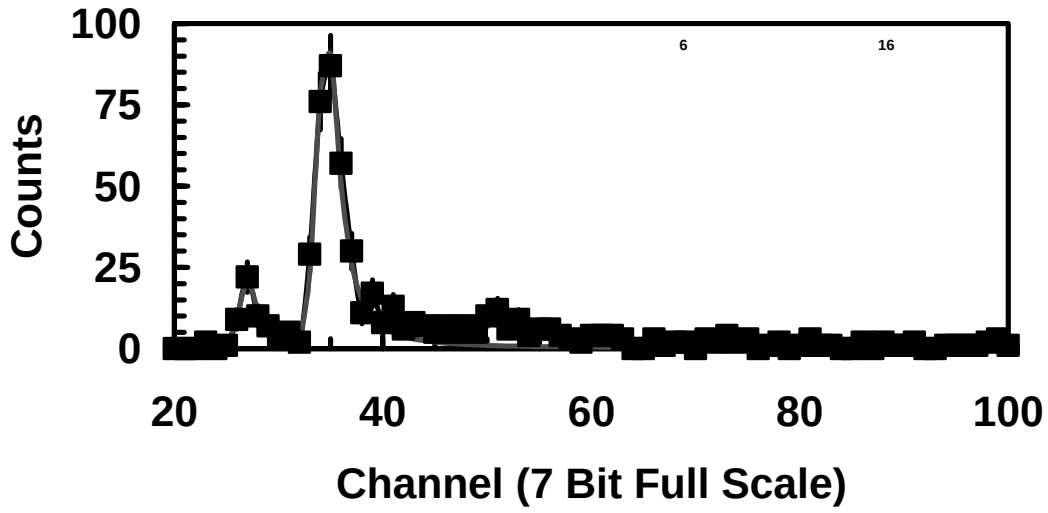

Figure 22 ^{16}C Delayed neutron spectrum collected in lithium detector #3.

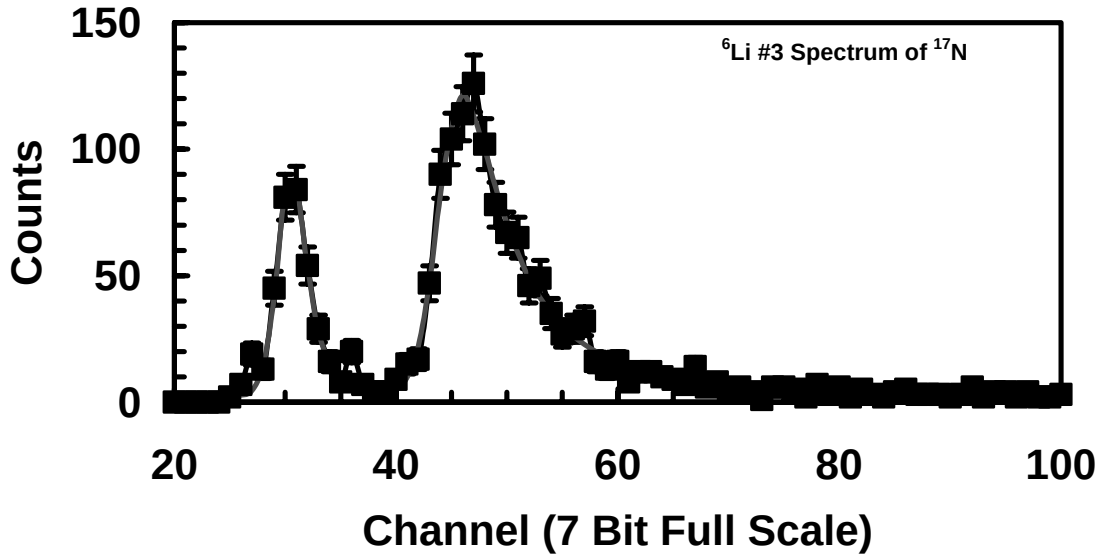

Figure 23 ^{17}N Delayed neutron spectrum collected in lithium detector #3.

As with the neutron bars, a calibration curve was constructed on the basis of the observed centroid channel of the delayed neutrons and their known energies. The parameters of the fit were the same as outlined in section (*) and will not be repeated here. Figure 24 shows the calibration curve for one of the ^{6}Li detectors (#3) generated using the compressed data. The y-axis value is inverse velocity in (ns/m) and the x-axis is the TDC channel of the neutron peak centroid.

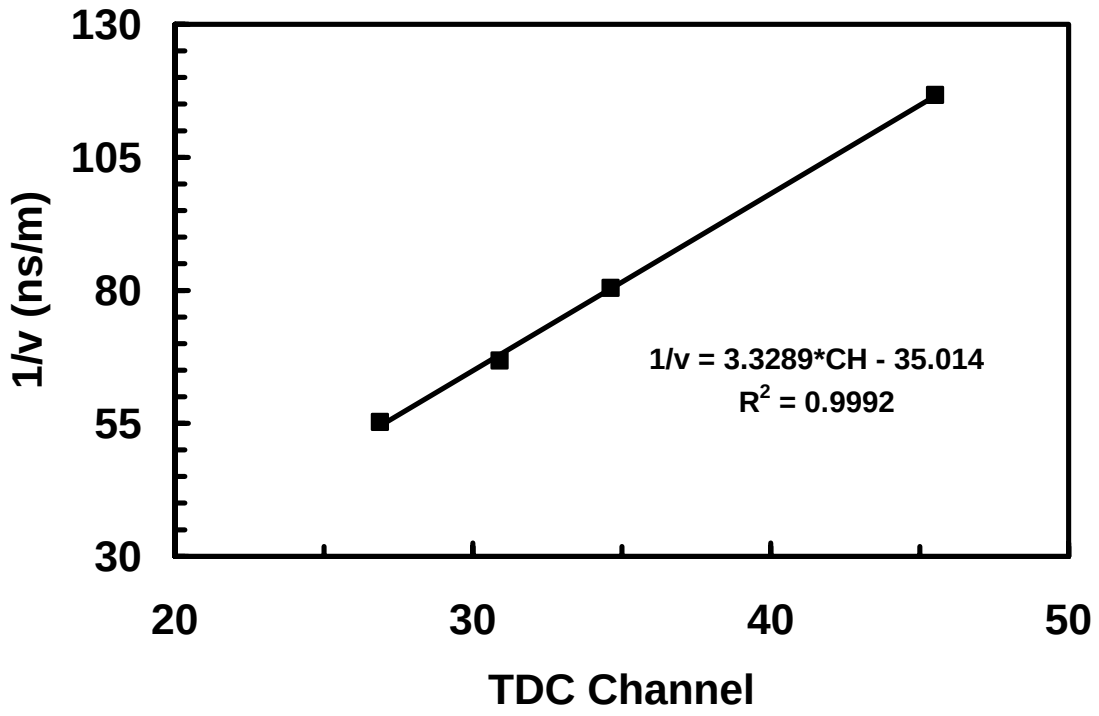

Figure 24 Calibration curve of lithium detector #3 from the known delayed neutrons of ^{16}C and ^{17}N. The y-axis is in units of inverse velocity (ns/m) and is related to the neutron energy. The TDC was compressed to reflect 7 bits full-scale.

The procedure was repeated for each of the three ^{6}Li detectors in the seven-bit time domain. The final values of the slope and offset parameters relating the TDC channel to the inverse velocity are given in table 16. The inverse velocity in (ns/m) will

be equal to the channel multiplied by the slope parameter plus the offset parameter. The energy of the neutron in MeV will be 5227.083 times the squared velocity in ns/m.

Table 16 Calibration parameters for the lithium detectors in the seven bit time domain. The inverse velocity of a neutron in (ns/m) is equal to the TDC channel times the slope plus the offset.

Detector	Slope	Offset
^{6}Li #1	3.631	-36.406
^{6}Li #2	7.651	-114.15
^{6}Li #3	3.329	-35.014

3.7.1 EFFICIENCY CALIBRATION

To determine the efficiency of the ^{6}Li glass detectors as a function of energy, the four delayed neutrons emitted by the calibration isotopes, ^{17}N and ^{16}C were integrated in each of the spectra. From these data, the known branching ratios of the neutron lines, and the total number of decays extracted from the half-life spectra, a measure of the ^{6}Li glass detectors' efficiencies at the corresponding energies was calculated. Table 17 gives the measured total efficiency as a function of neutron energy for the three ^{6}Li detectors.

Table 17 Calibration points utilized to determine the total efficiency of each lithium detector. The source neutrons are from the decay of ^{16}C and ^{17}N.

E_n keV	^{6}Li #1 ε–total	^{6}Li #2 ε–total	^{6}Li #3 ε–total
384	1.68(15) E-4	2.62(16) E-4	1.35(9) E-4
808	4.06(39) E-5	6.65(61) E-5	3.13(31) E-5
1172	3.81(35) E-5	7.96(49) E-5	3.01(22) E-5
1715	3.39(62) E-5	5.70(94) E-5	3.08(58) E-5

The neutron capture cross section of ^{6}Li is well known over a large range of incident neutron energies and they have been tabulated in the common nuclear databases []. The molar composition of the inorganic material was supplied by the manufacturer [] and the isotopic fraction of ^{6}Li was also made available. From the known neutron-capture cross section and the physical characteristics of the scintillators, the intrinsic efficiency of the three ^{6}Li detectors was calculated following the procedure outlined in [FKMM]. The center of mass energies were converted to lab energy for the cross-sectional data and the intrinsic efficiency curve was scaled to fit the measured total efficiencies supplied by the calibration beams of ^{16}C and ^{17}N. Figure 25 shows the scaled intrinsic efficiency for ^{6}Li detector #3 and the data to which the cross-sectional curve was scaled.

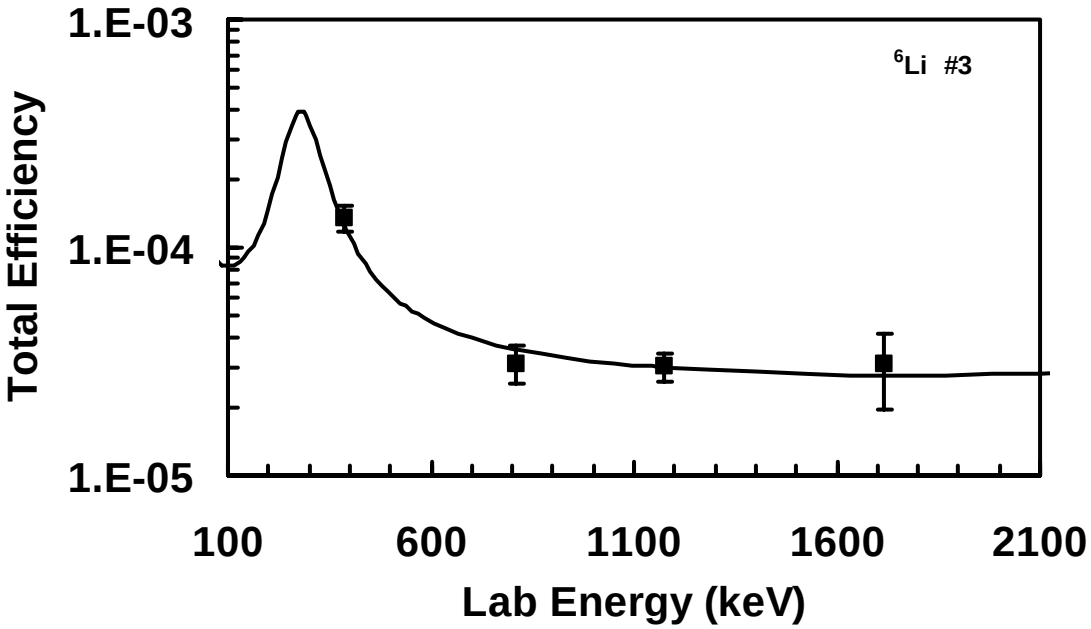

Figure 25 Calibration curve for the efficiency determination of lithium detector #3. The solid line represents the known neutron capture cross-sectional data on ^{6}Li converted into relative efficiency and scaled to fit the data points measured.

The scaling factor derived for the three ^{6}Li glass scintillators should be representative of the detectors' geometric efficiencies. The solid angle coverage of the detectors was calculated from the measured physical geometry and crystal dimensions. The necessary parameters to calculate the geometric solid angle are shown in figure 26.

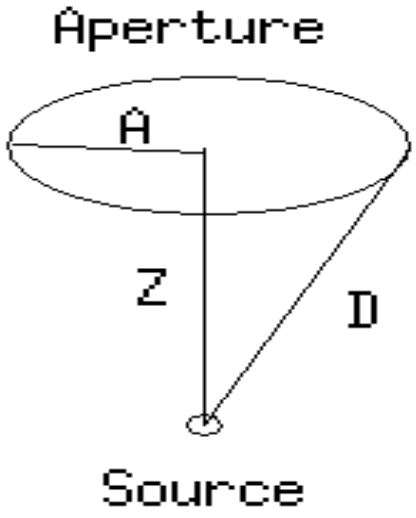

Figure 26 Parameters necessary to estimate the geometric solid angle of an aperture (detector) with respect to a point source of activity.

Here, A is the detector radius (2.54cm), Z is the linear source-to-aperture distance, and D is the distance between the source activity and the edge of the aperture. From these values, and assuming that the source/detector separation is much larger than the source spread, the geometric solid angle (G_p) may be calculated from the expression:

$$G_p = 1/2\,(1 - Z/D)$$

Table 18 lists the geometric solid angle for each of the ^{6}Li detectors calculated in this manner along with the scaling parameter for the efficiency fits based on the reported cross-sectional data. The error in the scaling parameter reflects the change in its value necessary to produce a $\Delta\chi^2$ of one unit in the fit.

Table 18 Calculated value of the geometric efficiency and best fit value of the scaling parameter for each of the lithium detectors.

Detector	Geometric Efficiency	Scaling Factor
^{6}Li #1	4.11(12) x 10^{-3}	3.57(37) x 10^{-3}
^{6}Li #2	1.46(8) x 10^{-2}	1.57(13) x 10^{-2}
^{6}Li #3	2.64(7) x 10^{-3}	2.89(25) x 10^{-3}

Of note here is the good agreement between the solid angle estimates from the physical geometry and the best-fit value for the scaling parameter, particularly for detectors two and three. The agreement provides a greater measure of confidence in the total efficiency derived for the ^{6}Li glass scintillators and thus for the branching ratio determinations for the ^{19}N isotope of interest.

3.7.2 ^{19}N RESULTS – ^{6}Li DETECTORS

Unfortunately, the intensity of the ^{20}N secondary beam taken together with the total efficiency of the ^{6}Li detectors resulted in too few events recorded by the devices to be of use. As a consequence, the results presented here are restricted to those for ^{19}N.

The goal behind including the ^{6}Li detectors was to enable the observation of low energy delayed neutrons from the decay of ^{19}N. To accentuate the low energy peaks in the ^{6}Li spectra, the time calibration was utilized to rebin the data into the energy domain. The following three figures 27-29 show the spectra collected by each of the ^{6}Li detectors during the decay of ^{19}N where the data have been converted into an energy scale and redistributed into bins of 40 keV width. Also shown are the fits to the peaks where the peak shapes used were simple gaussians and the background is of the form $1/x^{2}$.

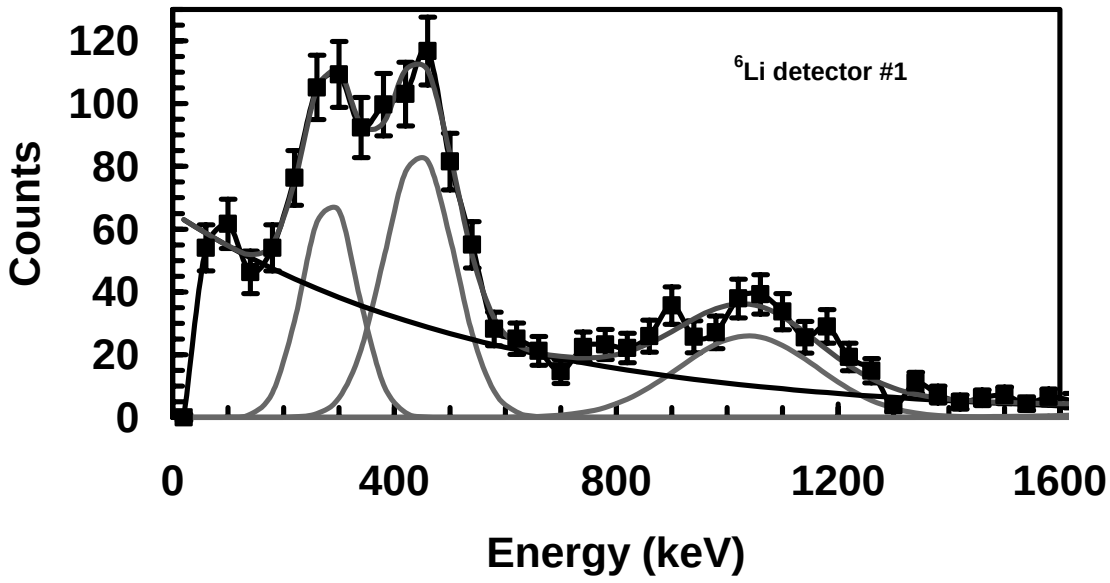

Figure 27 Energy spectrum of delayed neutrons observed by ^{6}Li detector #1 during the decay of ^{19}N. The width of the energy bins is 40 keV.

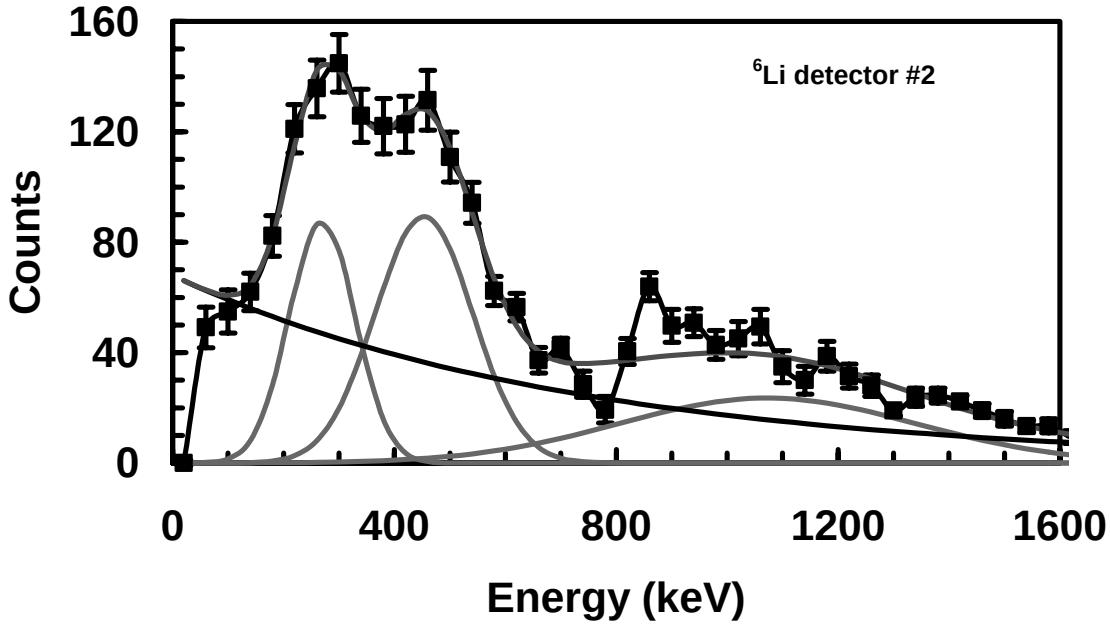

Figure 28 Energy spectrum of delayed neutrons observed by ^{6}Li detector #2 during the decay of ^{19}N. The width of the energy bins is 40 keV.

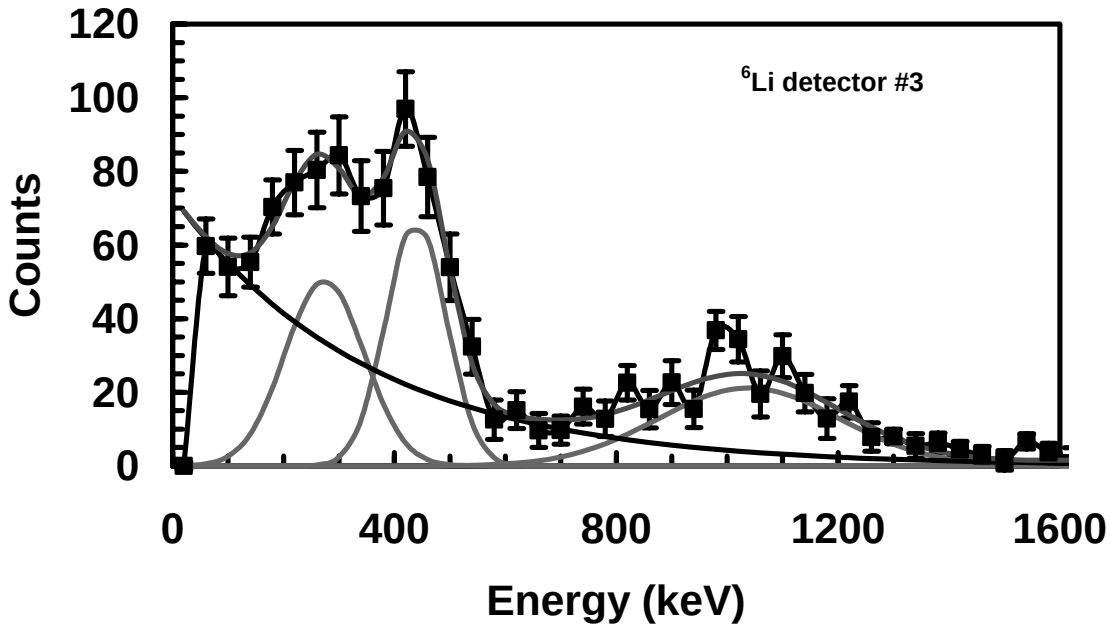

Figure 29 Energy spectrum of delayed neutrons observed in lithium detector #3 during the decay of ^{19}N. The width of the energy bins is 40 keV.

From the integrated area of the peaks, the detection efficiency calibration, and the total number of ^{19}N decay events, the branching ratio can be deduced for the transitions observed in each of the three devices. The dominant sources of error in the branching ratio determination come from the integrated area of the peaks and the total efficiency. Due to the uncertainty in the shape of the ^{6}Li energy spectrum background, the error was estimated from a series of fits to the data with different background shapes including exponentials, lines, and functions of the form $1/x^2$. All fits were done in MINUIT/MINOS and the large uncertainties in the peak areas reflect differences in the best-fit values of the peak parameters over the various functional forms of the background.

The error in the efficiency comes from two sources; first, the error in the scaling parameter imparts an error of nearly ten percent in all three cases and, second, the error

in the centroid energy from the fits drives an additional uncertainty in the efficiency, particularly for low energy neutrons where the slope of the efficiency curve is extremely steep. Consequently, taking the energy error into account yields large fractional errors for the ~280 and ~460 keV transitions. Table 19 gives the necessary parameters and the calculated branching ratios for the delayed neutrons by detector.

Table 19 Branching ratio determination for delayed neutrons observed by the lithium detectors during the decay of ^{19}N. Also tabulated are the parameters necessary for the branching ratio calculation along with the associated errors.

Detector	Neutron Energy (keV)	Peak Area	^{19}N Total Decays	Efficiency (Total)	Branching Ratio (%)
^{6}Li #1	280(50)	331(115)	4.64(10)E7	4.9(13)E-4	1.5(7)
^{6}Li #1	450(40)	449(115)	4.64(10)E7	1.01(16)E-4	9.6(29)
^{6}Li #1	1040(40)	305(100)	4.64(10)E7	3.86(41)E-5	17.0(59)
^{6}Li #2	270(50)	483(155)	4.64(10)E7	8.6(14)E-4	1.2(4)
^{6}Li #2	460(40)	649(155)	4.64(10)E7	1.63(24)E-4	8.6(20)
^{6}Li #2	1070(40)	590(195)	4.64(10)E7	6.61(69)E-5	19.2(67)
^{6}Li #3	280(50)	306(80)	4.64(10)E7	3.93(65)E-4	1.7(6)
^{6}Li #3	440(40)	306(80)	4.64(10)E7	8.5(19)E-5	7.8(27)
^{6}Li #3	1040(40)	267(50)	4.64(10)E7	3.13(34)E-5	18.4(40)

The branching ratio results for the corresponding transitions among the three ^{6}Li detectors are in excellent agreement. The weighted means of the measurement yield branching ratios of 1.4(22) %, 8.6(10) % and 18.2(23) % for the delayed neutrons having energies of about 280 keV, 460 keV and 1050 keV respectively.

3.8 GAMMA RAY DATA

The experimental end-station included two HPGe detectors to monitor gamma-rays emitted during the decay of the isotopes of interest. The detectors were energy calibrated with in-house sources of ^{134}Cs, ^{204}Bi, and ^{60}Co - all of which have known

decay schemes and well-established gamma transitions. The detectors were energy calibrated over the full 8192 channel domain as the gamma-ray intensities were sufficiently strong for all calibration sources and secondary beams to do so.

The in-house sources were monitored by affixing the source's solid support backing to the implantation scintillator. However, unlike the radioactive beam runs, the implantation scintillator was removed from the trigger and replaced by either a BaF_2 or NaI detector "start" signal. This substitution for the implantation scintillator "start" permitted conclusive identification of the gamma ray causing the "start" signal in the electronics which later facilitated a determination of the HpGe detectors' efficiency at various known energies. The BaF_2 or NaI detector was placed directly beneath the implantation scintillator to provide the maximum possible solid angle coverage. As an example of the spectra collected in the HPGe detectors using the calibration sources, Figure 30 shows the response of one of the gamma-ray detectors to the ^{60}Co activity.

The peaks observed in the Germanium detectors were fit to symmetric gaussian shapes plus linear backgrounds. Using these data, a calibration line for each of the two germanium detectors was determined by plotting the centroid channel versus the known transition energy. The data points were fit to a line using EXCEL. The raw data and the results of the straight line fits are shown in figure 31. The slope and offset for the energy calibration of Ge1 are 0.4919(2) keV/CH and 11.51(31) keV, respectively, while the slope and offset for the full-scale energy calibration of Ge2 are 0.7309(3) keV/CH and 9.02(29) keV.

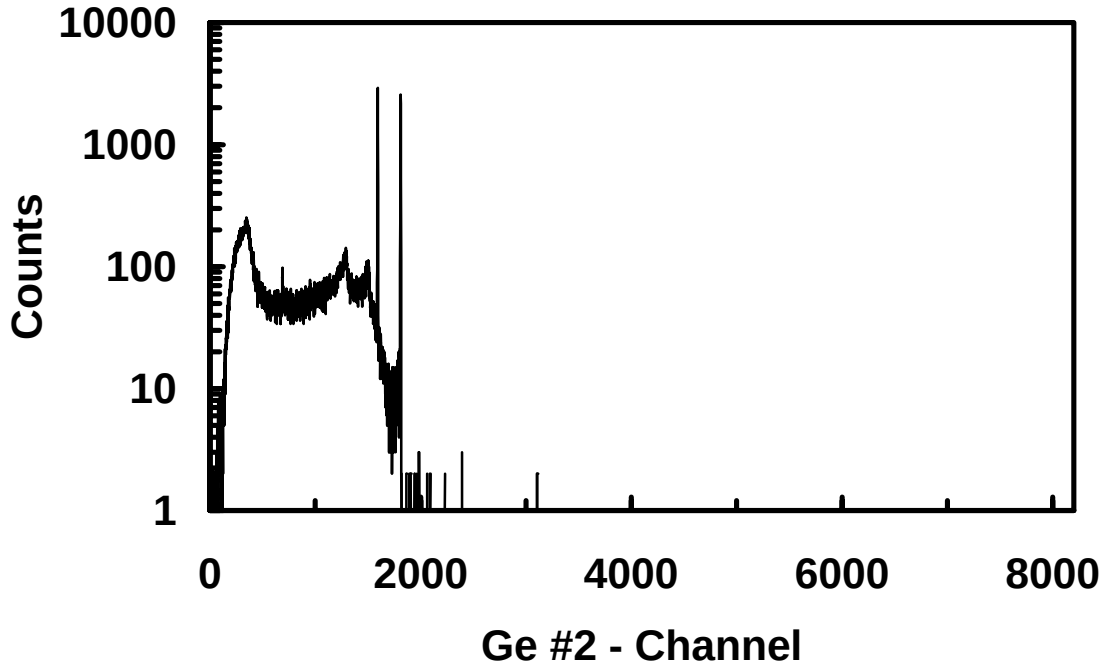

Figure 30 Gamma ray spectrum collected by Ge #2 plotted as intensity versus channel number for the ^{60}Co calibration source.

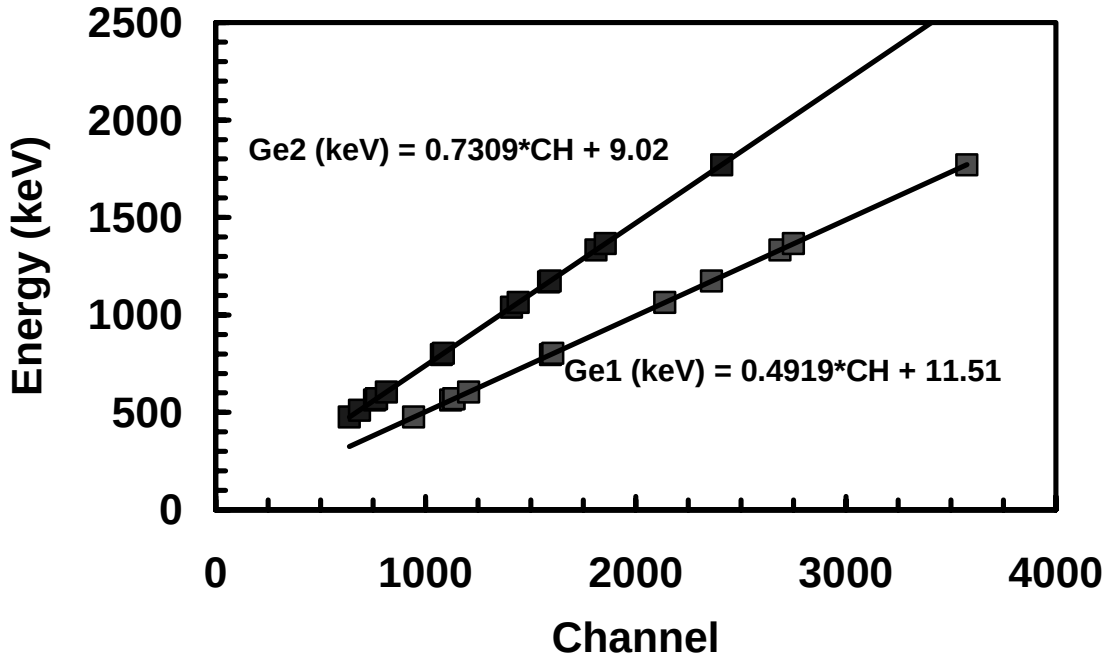

Figure 31 Calibration curves for the energy calibration of the Germanium detectors. Shown in the figure are the best-fit slope and offset for the linear fit to the calibration data.

3.8.1 GAMMA-RAY SPECTRA OF THE ISOTOPES OF INTEREST

The experiment proceeded by implanting secondary beam activity within the start detector for a set time followed by a beam-off interval where the real-time clock was in play. The germanium detectors, however, were supported by an electronics algorithm that permitted data to be collected during both the implantation period and the beam-off period. This was done to allow for the possibility of observing gamma rays of lower intensity due to the increased duty cycle of the Germanium detectors. For the branching ratio determinations outlined in section (*), the included data are restricted to the beam-off interval as this is the portion of the sequence from which the beta activity may be conclusively extracted.

Figures 32 through 39 show the spectra collected in the germanium detectors during the beam-off sequences of the data runs for the four secondary beams (^{16}C, ^{17}N, ^{19}N, ^{20}N). The spectra are plotted on a logarithmic scale of counts versus energy in keV as calculated from the calibration formulae indicated in figure 31.

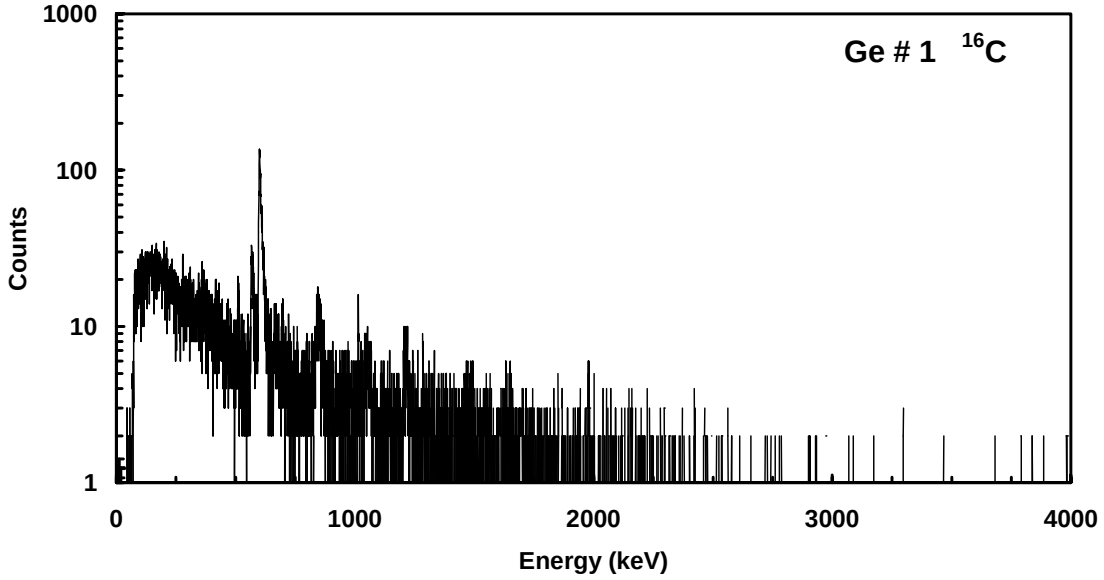

Figure 32 Calibrated energy spectrum of events collected in germanium detector # 1 during the beam-off period of the ^{16}C runs. The data are plotted as intensity versus energy on a logorithmic scale.

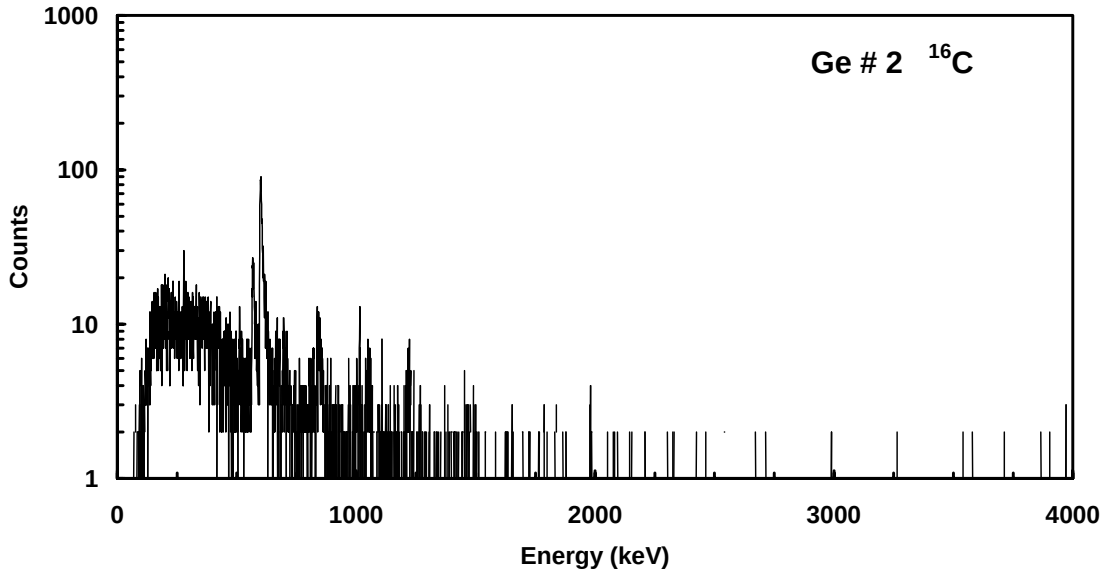

Figure 33 Calibrated energy spectrum of events collected in germanium detector # 2 during the beam-off period of the ^{16}C runs. The data are plotted as intensity versus energy on a logarithmic scale.

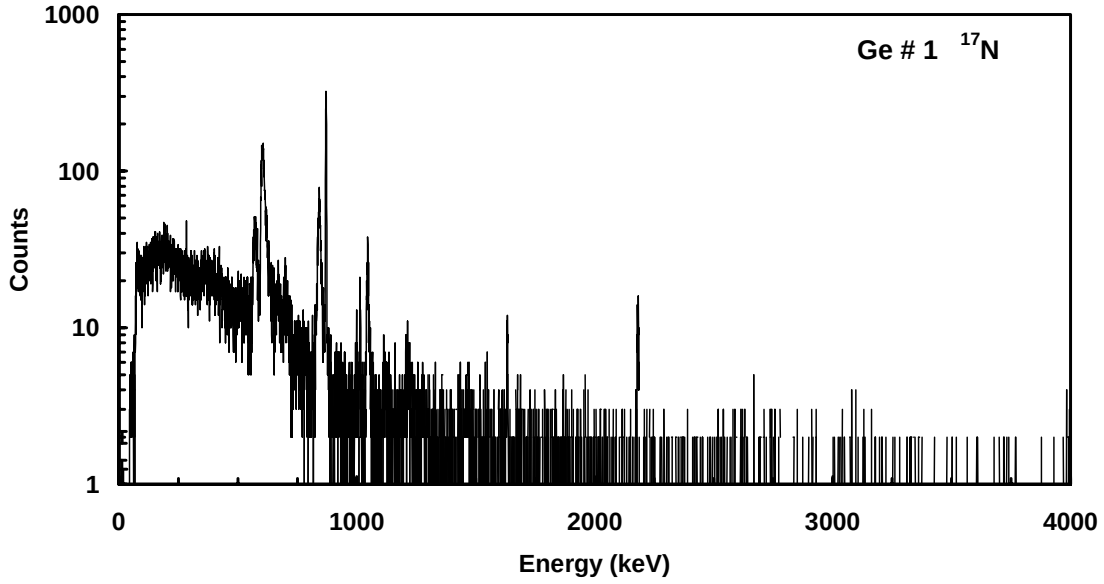

Figure 34 Calibrated energy spectrum of events collected in germanium detector # 1 during the beam-off period of the ^{17}N runs. The data are plotted as intensity versus energy on a logarithmic scale.

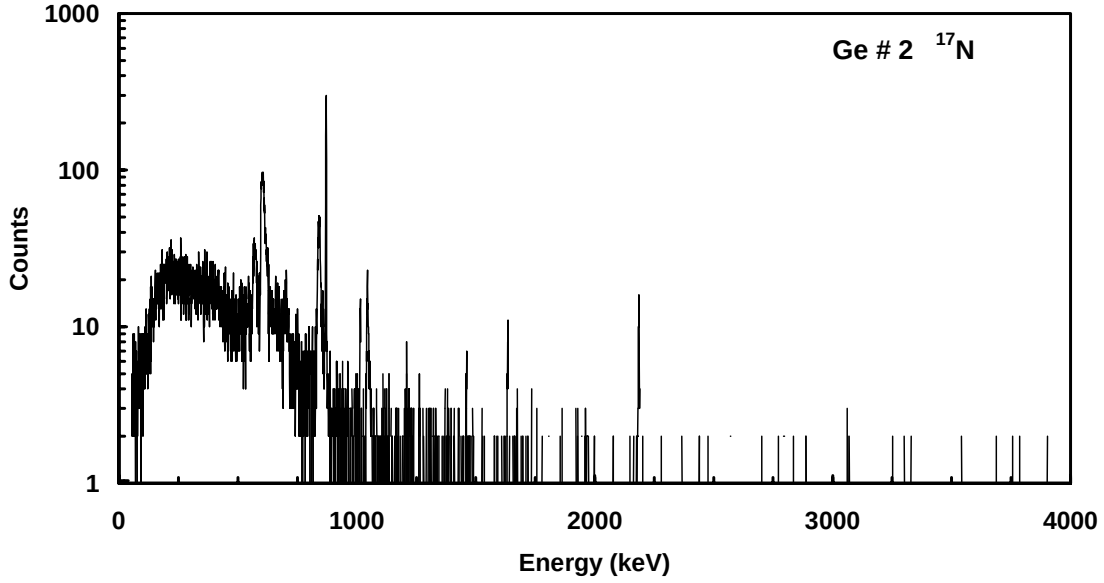

Figure 35 Calibrated energy spectrum of events collected in germanium detector # 2 during the beam-off period of the ^{17}N runs. The data are plotted as intensity versus energy on a logarithmic scale.

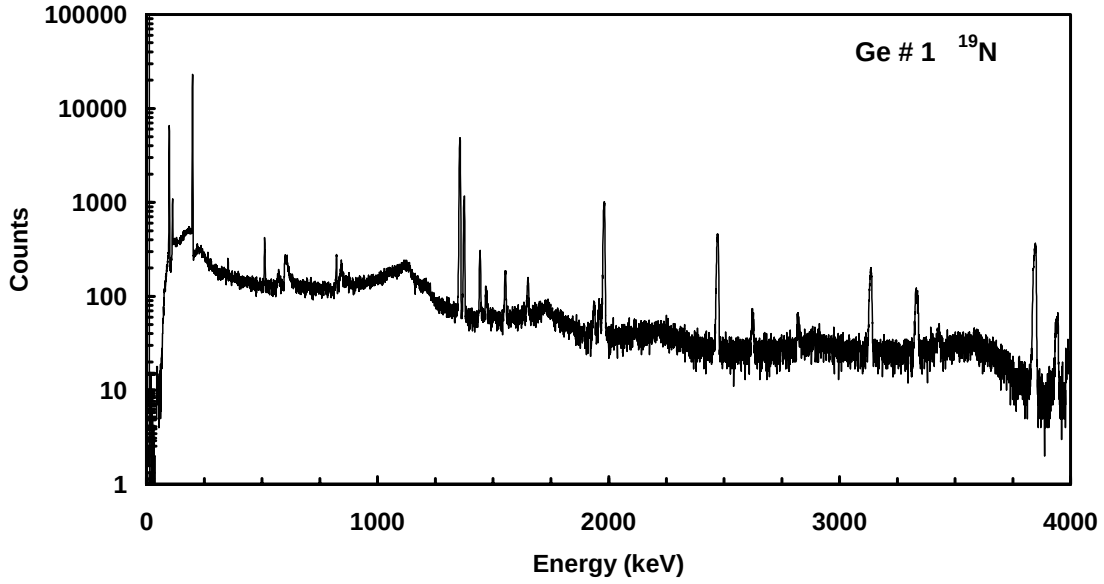

Figure 36 Calibrated energy spectrum of events collected in germanium detector # 1 during the beam-off period of the ^{19}N runs. The data are plotted as intensity versus energy on a logarithmic scale.

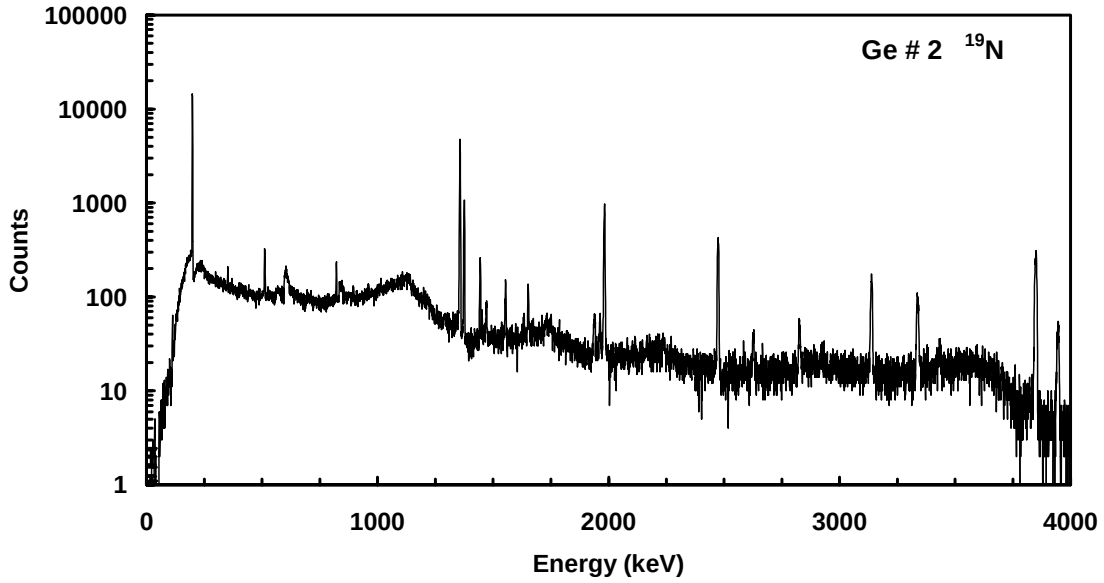

Figure 37 Calibrated energy spectrum of events collected in germanium detector # 2 during the beam-off period of the ^{19}N runs. The data are plotted as intensity versus energy on a logarithmic scale.

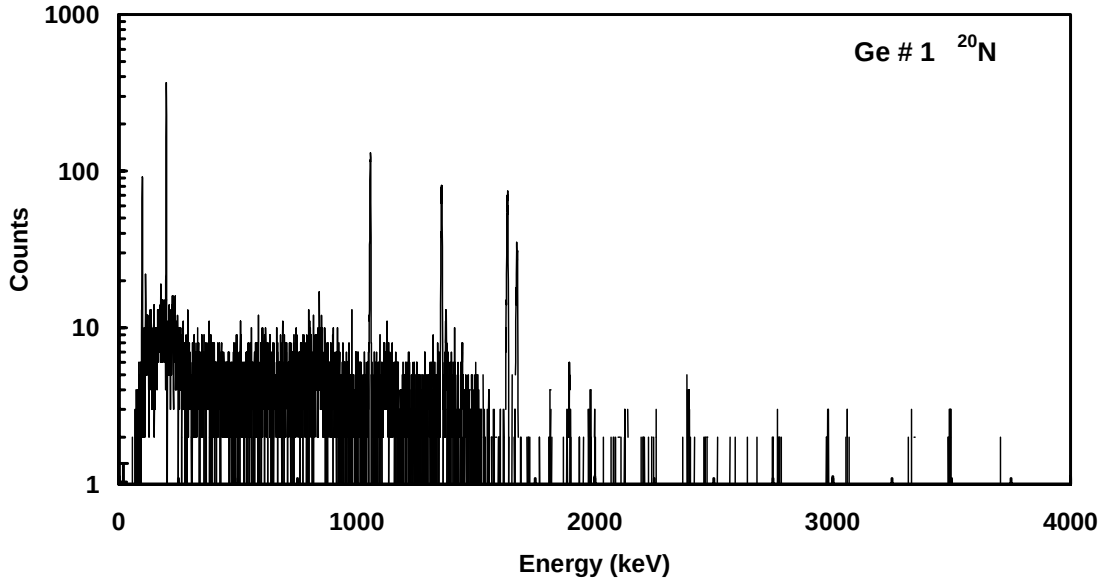

Figure 38 Calibrated energy spectrum of events collected in germanium detector # 1 during the beam-off period of the ^{20}N runs. The data are plotted as intensity versus energy on a logarithmic scale.

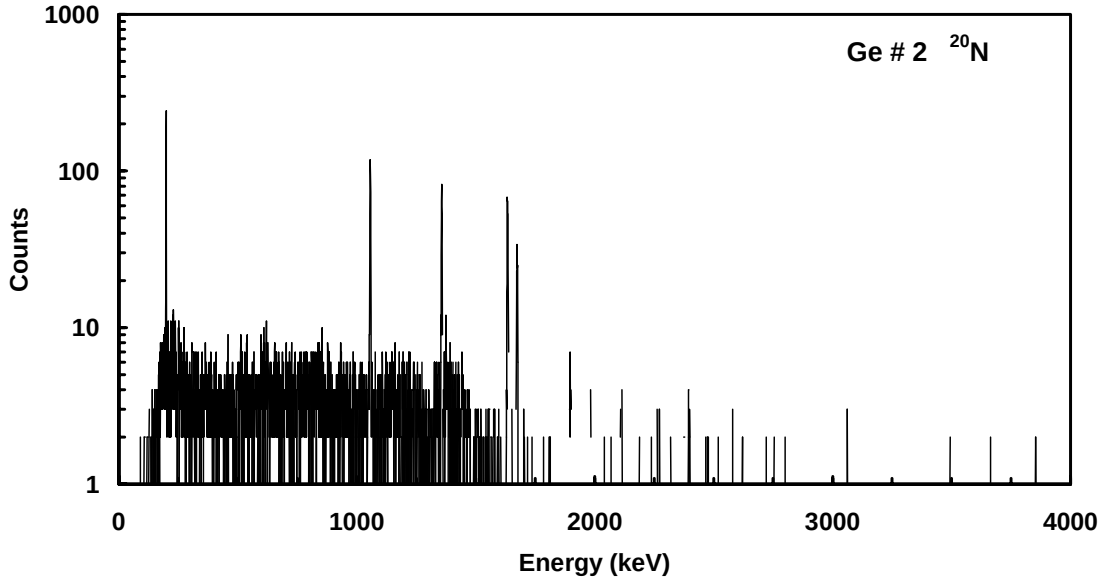

Figure 39 Calibrated energy spectrum of events collected in germanium detector # 2 during the beam-off period of the ^{20}N runs. The data are plotted as intensity versus energy on a logarithmic scale.

3.8.2 BACKGROUND GAMMA RAYS

Gamma-ray lines that appeared in the spectra of any three of the four isotopes of interest were assigned as being due to background. Table 20 lists, by detector, the transitions satisfying this criterion. As expected, there is a direct correspondence between the two detectors for the gamma rays identified in this way. The exception to the background assignment, of course, is the 511 keV transition which is not necessarily due to background exclusively.

Table 20 Gamma rays attributed to background.

Ge # 1	Ge # 2
Energy (keV)	Energy (keV)
352	351
420	419
442	441
511	511
569	571
605	606
844	840
1014	1014
1273	1273
1367	1368
1808	1809

3.8.3 RATIO OF EFFICIENCIES

To determine the detection efficiency ratio of Ge1 to Ge2, and to detect systematic problems that may have developed over time in the germanium detectors, the ratio of counts in Ge1 to Ge2 for non-background transitions was calculated. The ratio of Ge1 to Ge2 intensities should be a constant for all gamma transitions originating at the implantation position provided that both germanium detectors were stable over the course of the experiment. Furthermore, if constant, the ratio of the counts is equal to

the ratio of the total detection efficiencies. Figure 40 shows a plot of the ratio of counts in Ge1 to counts in Ge2 (during the beam-off period) versus the energy of the gamma-ray line for those transitions observed during the ^{19}N production runs.

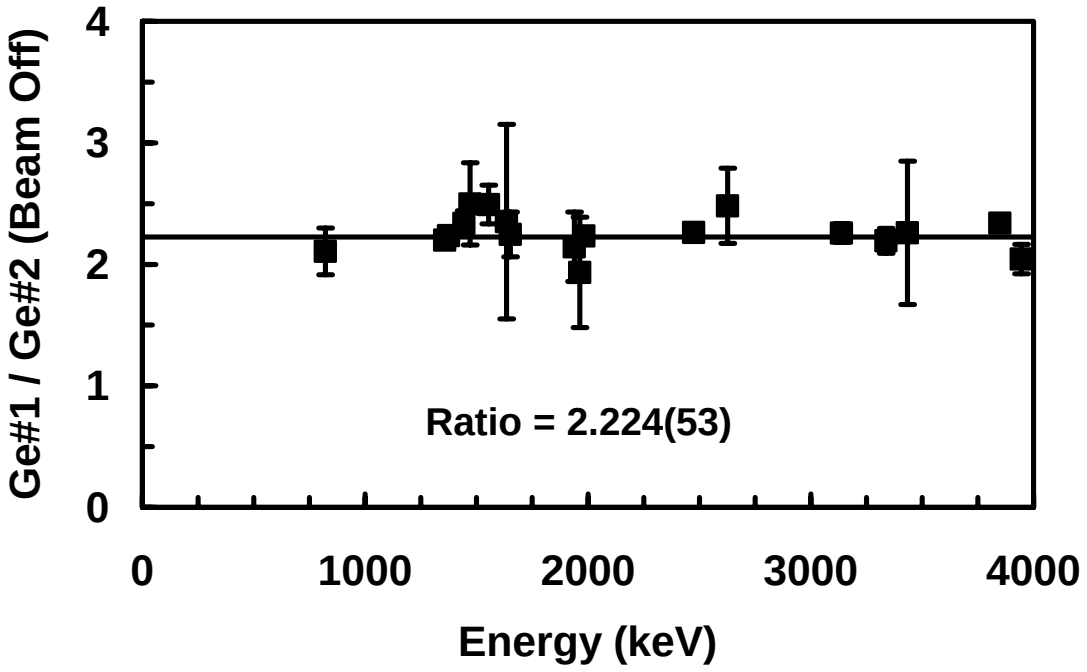

Figure 40 A plot of the ratio of counts detected in Ge#1 to counts in Ge#2 during the beam-off period of the ^{19}N experimental runs. The data are plotted at the ratio versus the energy of the gamma ray.

The figure suggests that the ratio of counts is indeed a constant. The value of the constant is 2.225(53) determined from a weighted linear fit to the data yielding a best-fit slope consistent with zero. Thus, the total detection efficiency of Ge1 is equal to this constant multiplied by the total detection efficiency of Ge2 over the energy range indicated.

3.8.4 GAMMA RAY SEGREGATION

As noted earlier, the germanium detectors were active during both the implantation and beam-off intervals. By taking the ratio of counts detected at each

gamma line over all times to the counts detected during the beam-off period, it was possible to segregate the observed gamma rays into groups. This was useful for assigning gamma rays as being due to the decay of the parent or the decay of the daughter.

The impantation and beam-off periods were set to maximize the counts detected from the isotope of interest. However, there may be significant gamma activity due to the beta decay of the daughter. The intensity of counts detected over all times to beam-off will not be the same for the daughter(s) as it will be for the isotope of interest – due to the difference between the half-lives. Thus, if the statistics are good enough, a plot of the counts over all times to beam-off counts should filter gammas due to the daughter's decay from those due to the implanted species. Figure 41 shows an example of this for ^{19}N where the ratio of counts in Ge2 for all times to beam-off is plotted against transition energy.

From figure 41 it appears that four of the observed gamma rays (blue) are not from the same source as the others (red). This is not unexpected as, in addition to gamma rays from the decay of ^{19}N, there should also be gamma rays present following the beta decay of the ^{19}N beta daughter, ^{19}O. This result was useful for the assignment of previously unobserved gamma rays – a topic that will be discussed later.

3.8.5 GAMMA RAY HALF-LIFE MEASUREMENTS

In addition to the detection ratios, the gamma rays were assigned on the basis of their half-life. In most cases, the intensity of the transitions was sufficiently strong to permit an analysis by this technique, however, it is noted that for the weakest transitions this method was not conclusive due to statistics and to the unfortunate fact that the

general background, whether due to Compton edges or betas or…, tended to have a half-life consistent with the dominant source implanted.

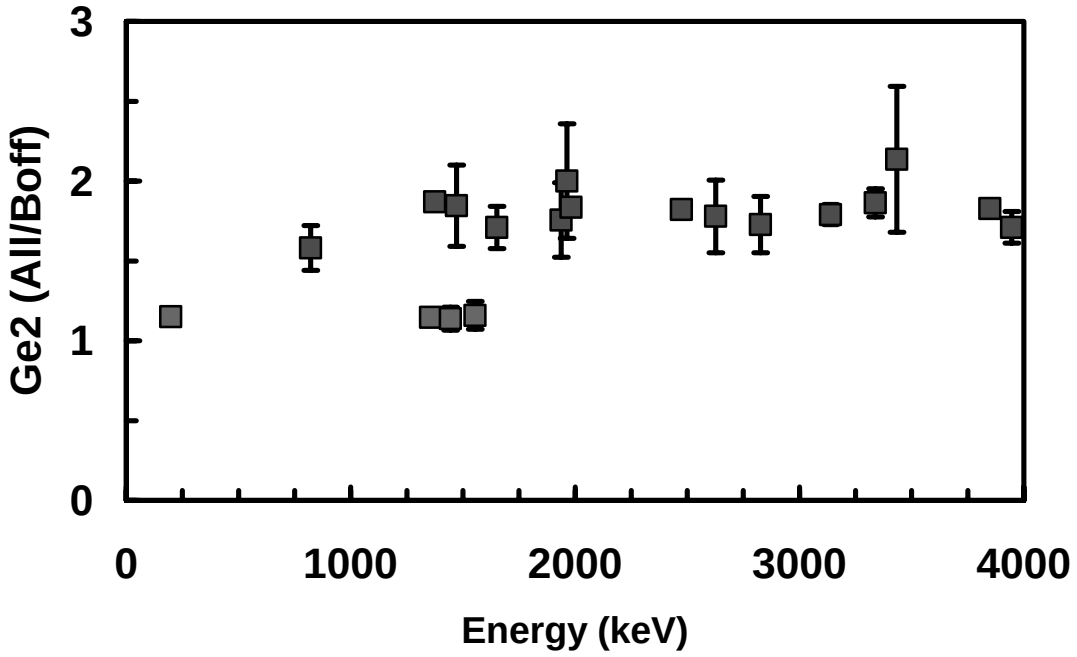

Figure 41 The ratio of counts detected in Ge #2 at all times to counts detected during the beam off period plotted against gamma-ray energy. The colors indicate those gamma rays that appear to originate from the same source.

Unlike the determination of the beta half-lives, the approach taken here was not rigorous. To circumnavigate the dead-time, the half-life spectra were fit over the final 80% of the clock channels rather than utilizing the more complicated dead-time/τ formalism outlined in section (*). Fortunately, the high purity of the secondary beams and the dramatic difference between the half-lives of the parent and daughter isotopes permitted a conclusive separation of gamma rays even using this less rigorous approach. It is necessaray to note that the best-fit value of the half-lives from the gamma gating were systematically longer than those from the beta decay analysis – not surprisingly.

As an example, figure 42 shows two representative half-life spectra from gamma rays observed during the implantation of a ^{19}N secondary beam.

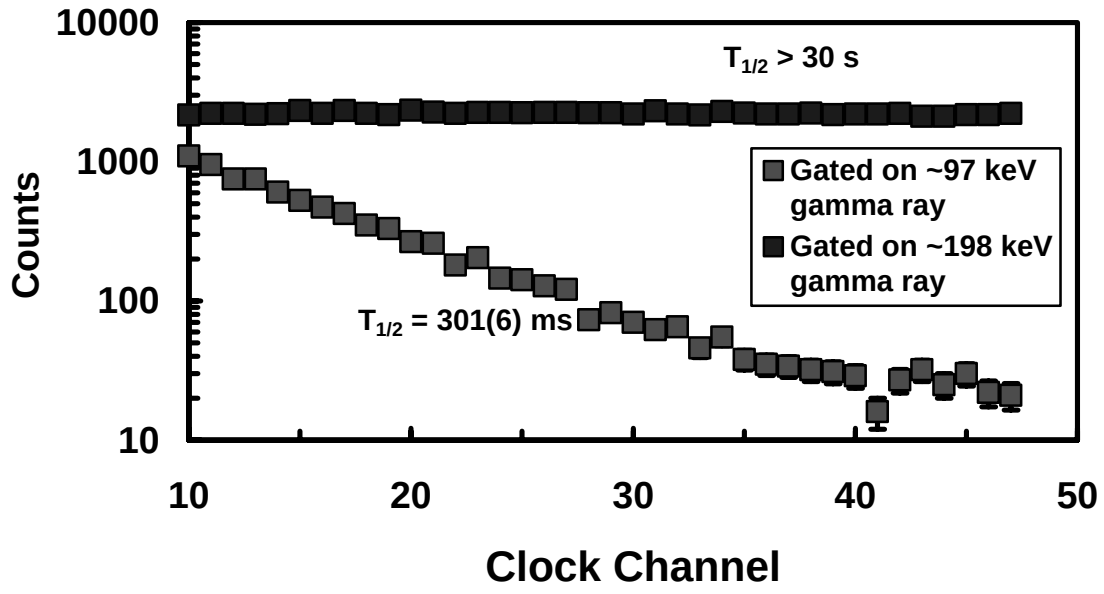

Figure 42 Gamma ray gated half-life spectra for two transitions observed in Ge #1. The clock parameter has been rebinned to reflect sixteen seconds in 256 channels.

3.8.6 GAMMA RAY ASSIGNMENTS ^{19}N, ^{20}N SECONDARY BEAMS

The gamma gated half-life spectra and the ratio of counts analysis facilitate the assignment of gamma rays to specific sources and as originating from specific levels. From the half-life data, the identity of the beta-decaying isotope may be extracted and from the energy of the gamma ray, the specific transition can be determined by comparison with daughter levels and in some cases, known transition energies given in the literature. Table 21 give the assignment of the observed, non-background gamma rays for the ^{19}N secondary beam runs and table 22 for the ^{20}N secondary beam runs.

Table 21 Gamma ray assignments for transitions observed during the beam-off period of the ^{19}N production runs.

R.I.B.	γ-Ray keV	β-Decay Source	γ-Ray Source	E-initial level	E-final level
^{19}N	**96**	^{19}N	^{19}O	96	0
^{19}N	**110**	^{19}O	^{19}F	110	0
^{19}N	**197**	^{19}O	^{19}F	197	0
^{19}N	**511**	-	-	-	-
^{19}N	**821**	^{19}N	^{18}O	4456	3634
^{19}N	**1357**	^{19}O	^{19}F	1554	197
^{19}N	**1374**	^{19}N	^{19}O	1472	96
^{19}N	**1444**	^{19}O	^{19}F	1554	110
^{19}N	**1472**	^{19}N	^{19}O	1472	0
^{19}N	**1554**	^{19}O	^{19}F	1554	0
^{19}N	**1633**				
^{19}N	**1652**	^{19}N	^{19}O	3634	1982
^{19}N	**1938**	^{19}N	^{18}O	3920	1982
^{19}N	**1960**	^{19}N	^{19}O	-	-
^{19}N	**1980**	^{19}N	^{18}O	1982	0
^{19}N	**2473**	^{19}N	^{19}O	3945	1472
^{19}N	**2623**	^{19}N	^{19}O	-	-
^{19}N	**2822**	^{19}N	^{19}O	-	-
^{19}N	**3136**	^{19}N	^{19}O	3232	96
^{19}N	**3338**	^{19}N	^{19}O	-	-
^{19}N	**3434**	^{19}N	^{19}O	-	-
^{19}N	**3849**	^{19}N	^{19}O	3945	96
^{19}N	**3945**	^{19}N	^{19}O	3945	0

Table 22 Gamma ray assignments for transitions observed during the beam off period of the ^{20}N production runs.

R.I.B.	γ-Ray keV	β-Decay Source	γ-Ray Source	E-initial level	E-final level
^{20}N	96	^{20}N	^{19}O	96	0
^{20}N	110	^{19}O	^{19}F	110	0
^{20}N	197	^{19}O	^{19}F	197	0
^{20}N	1057	^{20}O	^{20}F	1057	0
^{20}N	1127				
^{20}N	1357	^{19}O	^{19}F	1554	197
^{20}N	1374	^{20}N	^{19}O	1472	96
^{20}N	1444	^{19}O	^{19}F	1554	110
^{20}N	1634	^{20}F	^{20}Ne	1634	0
^{20}N	1674	^{20}N	^{20}O	1674	0
^{20}N	1896	^{20}N	^{20}O	3570	1674

3.8.7 EFFICIENCY CALIBRATION – STANDARD SOURCES

The efficiency of detectors Ge1 and Ge2 at specific gamma-ray energies was established utilizing both on-line and off-line data. The bulk of the efficiency determination arises from standard sources that were placed at the implantation position and monitored by the germanium detectors with a sodium iodide serving as the trigger for the electronics. This is the off-line portion.

The technique involved selecting one gamma ray in the NaI detector and calculating the number of gamma rays at a different energy that would be emitted in coincidence with the first one. The sources used were ^{134}Cs, ^{204}Bi, and ^{60}Co which all have gamma cascades as a part of their decay scheme. The following cross tables, for each of the isotopes (tables 23-25), detail the coincidence strength for gamma ray pairs in a cascade. The column headers indicate the energy of the gamma ray detected by the NaI trigger. The row headers indicate the energy of a second gamma ray that is in coincidence with the trigger – available to be recorded by one of the germanium devices. The table value is the fraction of the column-energy counts that will be emitted at the row energy. The efficiency of each germanium detector at a particular energy was determined by gating on one of the gamma rays detected in the NaI crystal. The trigger peak was integrated to determine the total number of start signals generated by the trigger gamma ray. As an example, figure 43 shows the relevant portion of the NaI spectrum collected for the ^{60}Co calibration source and the fits to the two peaks.

Table 23 Cross-table for ^{60}Co. For N gamma rays at "column" energy there are N times "cell value" gamma rays emitted at "row" energy in coincidence.

^{60}Co	1173	1332
1173	**0**	**0.99945**
1332	**1**	**0**

Table 24 Cross-table for ^{207}Bi. For N gamma rays at "column" energy there are N times "cell value" gamma rays emitted at "row" energy in coincidence.

^{207}Bi	1770	1442	1063	898	328	570
1770	**0**	**0**	**0**	**0**	**0**	**6.91e-2**
1442	**0**	**0**	**0**	**1**	**1**	**7.10e-6**
1063	**0**	**0**	**0**	**0**	**0**	**8.42e-1**
898	**0**	**9.94e-1**	**0**	**0**	**0**	**0**
328	**0**	**5.50e-3**	**0**	**0**	**0**	**7.1e-6**
570	**1**	**5.50e-3**	**1**	**0**	**1**	**0**

Table 25 Cross-table for ^{134}Cs. For N gamma rays at "column" energy there are N times "cell value" gamma rays emitted at "row" energy in coincidence.

^{134}Cs	1365	802	569	1039	475	796	1168	563	605
1365	**0**	**0**	**0**	**0**	**0**	**0**	**0**	**0**	**3.10e-2**
802	**0**	**0**	**0**	**0**	**0**	**0**	**8.57e-1**	**8.57e-1**	**7.30e-2**
569	**0**	**0**	**0**	**0**	**0**	**1.81e-1**	**0**	**0**	**1.58e-2**
1039	**0**	**0**	**0**	**0**	**0**	**0**	**0**	**0**	**1.00e-2**
475	**0**	**0**	**0**	**0**	**0**	**0**	**1.43e-1**	**1.43e-1**	**1.20e-2**
796	**0**	**0**	**0**	**0**	**0**	**0**	**0**	**0**	**8.69e-1**
1168	**0**	**1.77e-1**	**1**	**0**	**1.77e-1**	**0**	**0**	**0**	**0**
563	**0**	**8.23e-1**	**0**	**0**	**8.23e-1**	**0**	**0**	**0**	**9.00e-2**
605	**1**	**8.23e-1**	**1**	**1**	**8.23e-1**	**1**	**0**	**1**	**0**

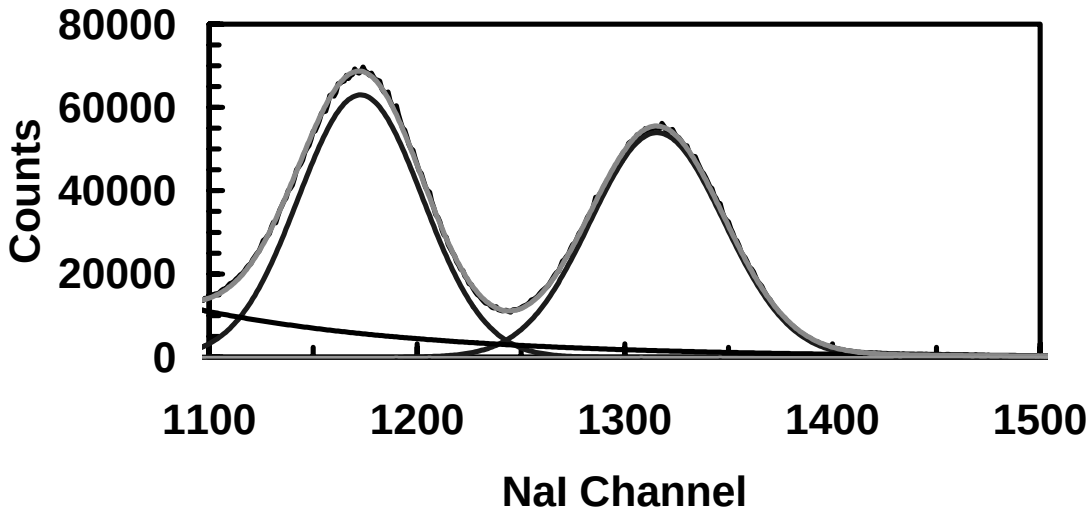

Figure 43 ^{60}Co source spectrum collected by the NaI start detector showing the fits to the peaks.

The energy of the trigger gamma ray, in this case 1332 keV, was designated the column of the appropriate cross-table. The energy of a gamma ray detectable by either germanium in coincidence with the trigger was found in the cross-table (by row). Multiplying the integrated number of events in the trigger peak by the value in the cell defined by the row and column energies determined the total number of transitions at the row energy that could possibly have been detected by the germanium detectors.

Setting a gate around the NaI peak and reflecting back onto the individual germanium spectra allowed for a measurement of the coincidence spectrum. The peak in the germanium spectrum corresponding to the row energy was then integrated to determine the intensity at that energy. As an example, figure 44 shows the spectrum accumulated by Ge2 while gated on the 1332 keV peak in the NaI detector.

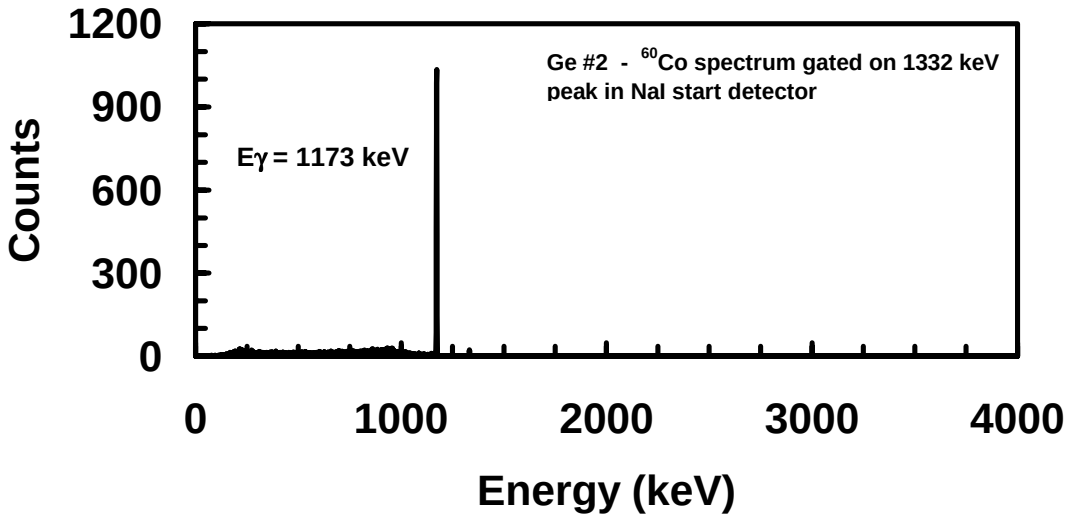

Figure 44 ^{60}Co spectrum collected in Ge # 2 gated on the 1332 keV peak of the NaI start detector. The only notable transition is the coincident 1173 keV line.

The efficiency of the specific germanium detector at the row energy is then equal to the integrated area of that peak in the germanium detector divided by the number that could possibly have been detected under these conditions. Table 26 lists the results of the efficiency determinations for Ge1 and Ge2 using this technique. Tabulated are the calibration source, the NaI peak energy and integration, the Ge1 (Ge2) peak energy and integration, fraction as taken from the cross-tables, and calculated Ge1 (Ge2) efficiency.

3.8.8 EFFICIENCY CALIBRATION – ON-LINE SOURCES

In addition to the off-line source measurements, there are data available within the experimental runs that provide a measure of the germanium detector efficiencies at various energies. The decay of ^{17}N provides two known gamma-ray lines for which the branching is known [NPA564] and the decay of ^{19}O provides five gamma-ray lines with known branching ratios [NPA595]. From the integrated half-life spectra, the total

number of decays due to each isotope may be determined. Taking the individual branching ratios and the total number of decays in concert yields the number of gamma rays emitted at the specific energies. The efficiency of the germanium detector at this energy is then simply the observed intensity of the line divided by the total number emitted. Table 27 lists the quantities necessary to deduce the germanium detector efficiencies at the tabulated energy.

Table 26 Off-line source calibration data for determining the efficiencies of the Ge detectors. The emboldened columns are the data necessary to generate a calibration curve.

Source	NaI gate (keV)	Counts	Ge1 Peak (keV)	Counts	Fraction (x-table)	Efficiency Ge # 1
60Co	1173	4.74E+06	**1332**	11294	1	**2.38E-03**
60Co	1332	4.29E+06	**1173**	10795	0.99945	**2.52E-03**
207Bi	570	1.20E+07	**1063**	22077	8.42E-01	**2.19E-03**
207Bi	570	1.20E+07	**1770**	1663	6.91E-02	**2.01E-03**
207Bi	1063	5.28E+06	**570**	17629	1	**3.34E-03**
207Bi	1770	3.41E+05	**570**	1044	1	**3.06E-03**
134Cs	795	1.25E+06	**604**	4131	1	**3.31E-03**
134Cs	795	1.25E+06	**569**	722	1.81E-01	**3.19E-03**
134Cs	605	2.05E+06	**563**	704	9.00E-02	**3.81E-03**
134Cs	605	2.05E+06	**796**	5374	8.69E-01	**3.01E-03**
Source	NaI gate (keV)	Counts	Ge2 Peak (keV)	Counts	Fraction (x-table)	Efficiency Ge # 2
60Co	1173	4.74E+06	**1332**	5222	1	**1.10E-03**
60Co	1332	4.29E+06	**1173**	5055	0.99945	**1.18E-03**
207Bi	570	1.20E+07	**1063**	11177	8.42E-01	**1.11E-03**
207Bi	570	1.20E+07	**1770**	801	6.91E-02	**9.70E-04**
207Bi	1063	5.28E+06	**570**	9238	1	**1.75E-03**
207Bi	1770	3.41E+05	**570**	581	1	**1.70E-03**
134Cs	795	1.25E+06	**604**	2076	1	**1.66E-03**
134Cs	795	1.25E+06	**569**	364	1.81E-01	**1.61E-03**
134Cs	605	2.05E+06	**563**	318	9.00E-02	**1.72E-03**
134Cs	605	2.05E+06	**796**	2506	8.69E-01	**1.40E-03**

Table 27 On-Line data pertinent to the efficiency calculation of the germanium detectors.

Eγ	Branch	# of βs	# of γs	Ge1	Ge2	**εGe1**	**εGe2**
keV	%	(/ 1e7)		Counts	Counts	**x1000**	**x1000**
	$^{19}O \rightarrow {}^{19}F^{*} + \beta^{-}$						
110	2.54(10)	4.4(2)	1.12(6)E6	3.1(1)E3	N/A	**2.77(15)**	**N/A**
197	95.9(21)	4.4(2)	4.2(3)E7	9.96(4)E4	3.64(2)E4	**2.36(12)**	**0.86(5)**
1357	50.4(11)	4.4(2)	2.2(2)E7	5.57(3)E4	2.54(2)E4	**2.51(13)**	**1.14(6)**
1444	2.64(6)	4.4(2)	1.16(6)E6	2.84(8)E3	1.22(5)E3	**2.44(14)**	**1.05(7)**
1554	1.39(3)	4.4(2)	6.1(4)E5	1.77(7)E3	7.1(4)E2	**2.89(18)**	**1.16(9)**
	$^{17}N \rightarrow {}^{17}O^{*} + \beta^{-}$						
871	3.34(50)	2.3(1)	7.7(12)E5	2.58(6)E3	1.15(4)E3	**3.36(53)**	**1.50(24)**
2184	0.34(6)	2.3(1)	7.8(15)E4	150(14)	7.2(10)E1	**1.92(44)**	**0.92(21)**

3.8.9 EFFICIENCY CALIBRATION – GERMANIUM COINCIDENCES

In addition to the on-line calibrations described in the previous section, it was possible to generate efficiency calibration points for Ge#1 at low energy using a coincidence technique. The energy levels of the ^{19}O and ^{19}F daughters are well known and some of the properties of the decay of each level are also known or may be inferred. For example, the observation of a 1376 keV line during the decay of ^{19}N indicates the transition from the 1472 keV excited state in ^{19}O to the 96 keV excited state. It must be true that for every 1376 keV gamma ray there is a corresponding emission of a 96 keV

gamma ray. Therefore, the efficiency of Ge#1 at 96 keV can be determined by gating on the 1376 keV line in Ge#2 and reflecting back onto the Ge#1 energy spectrum. The efficiency of Ge#1 at 96 keV will be equal to the number of observed 96 keV counts in the gated spectrum divided by the total number of 1376 keV counts in Ge#2. The statistics of such an analysis are necessarily poor due to the multiplicative aspect of the germanium efficiencies. However, in the absence of another method to measure the efficiency of at least one of the germanium detectors at 96 keV, the poor statistics will have to be absorbed. Table 28 gives the results of the germanium coincidence analysis and the calculated efficiency at the points taken.

Table 28 Germanium detector efficiencies determined using the coincidence technique.

Ge#2 Peak Gating (keV)	Ge#1 Peak Energy (keV)	Ge#1 Peak Area	Ge#2 Peak Area	Efficiency at Ge#1 Energy
3849	96	14(3.7)	6604(84)	2.12(57)E-3
1376	96	18(4.3)	10412(109)	1.73(41)E-3
1357	197	82(9.1)	29080(175)	2.82(32)E-3
1444	110	2(1.4)	1384(72)	1.45(102)E-3
2473	96	11(3.3)	6401(85)	1.72(52)E-3
2473	1376	16(4)	6401(85)	2.50(63)E-3

3.8.10 EFFICIENCY CALIBRATION – SUMMARY

Taking the data acquired from the on-line and off-line sources in concert, efficiency curves for detectors Ge1 and Ge2 were constructed. Figure 45 shows the comprehensive raw efficiency data for detector Ge2.

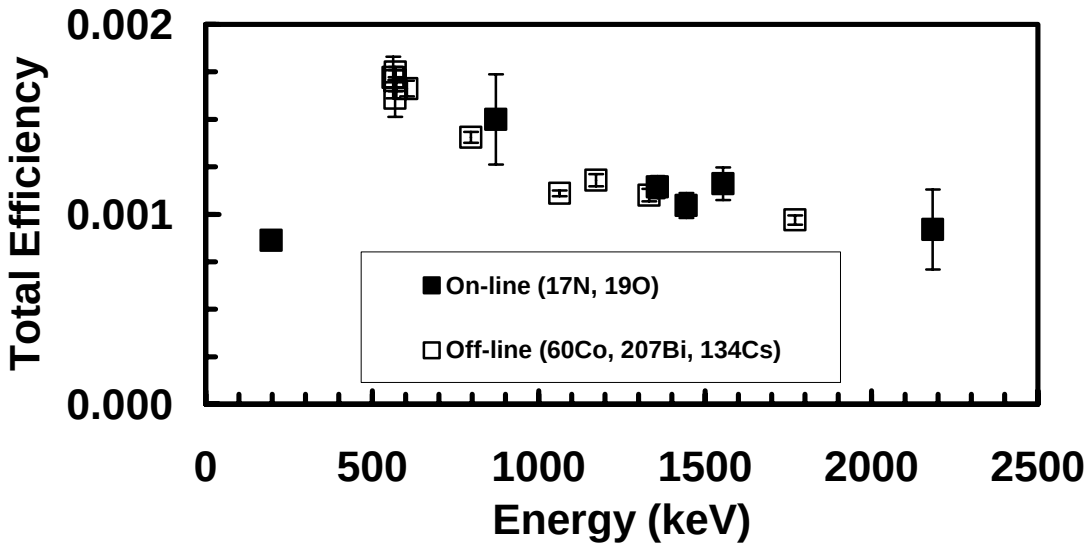

Figure 45 Efficiency data collected for detector Ge #2 from the on-line and off line data. The total efficiency is plotted as a function of gamma-ray energy.

The data above 500 keV were fit to a functional form given in []. The equation of the fit is given as:

$$\varepsilon = c \cdot (E / Eo)^{-\delta}$$

where ε is the efficiency, c is a dimensionless variable parameter, E is the gamma-ray energy in keV, Eo is a constant set equal to 1 keV to eliminate the energy dimension, and δ is a constant based on the volume of the germanium crystal that is given by:

$$\delta = 2.14 - 0.629 \log V$$

Where V is the volume of the germanium detector in cm^3. In this experiment, the volume of detector Ge1 was 542 cm^3 and the volume of Ge2 was 411 cm^3 where these quantities were deduced from the specification sheets provided by the manufacterer. Figure 46 shows the same calibration data for Ge2 and the best fit to the efficiency data using the above formulae.

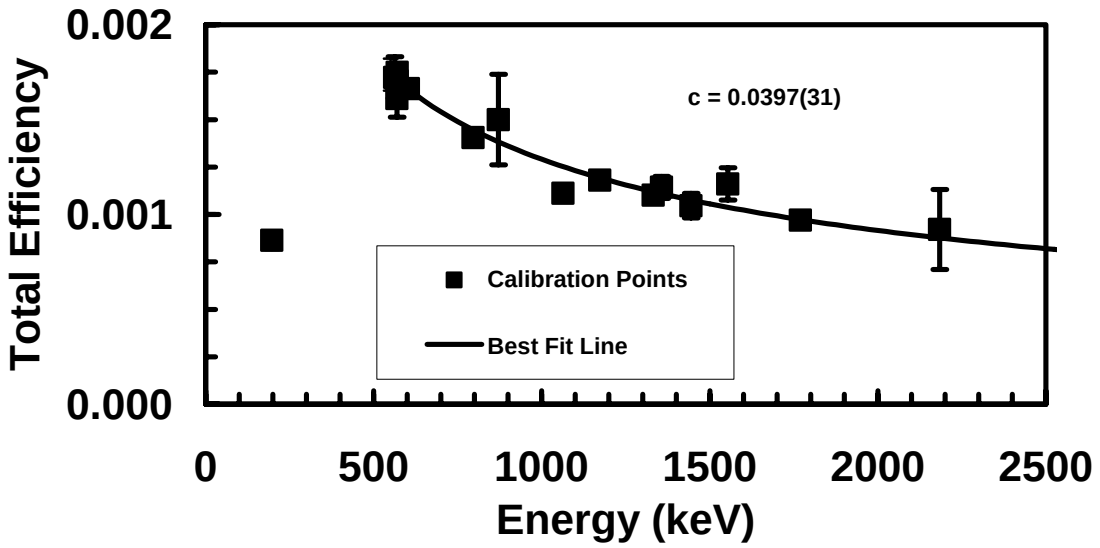

Figure 46 Efficiency calibration points for detector Ge #2 and the best fit through those data. The only variable parameter in the fit is the "c" parameter – the value is presented in the plot.

Since there is only one variable in the fit and therefore no correlation problem, the error on parameter c was deduced by the change in its value necessary to produce an increase in the total chi-squared of one unit. This error is valid over the interpolation region ranging from about 560 keV to 2180 keV in energy. To estimate the error associated with extrapolating the fit to higher energies, the high efficiency at 560 keV ($c + \sigma$) and the low efficiency at 2180 keV ($c - \sigma$) were fit to the same functional form. This was repeated for the low efficiency at 560 keV ($c - \sigma$) and the high efficiency at 2180 keV ($c + \sigma$). The two curves diverge above the interpolation range and hence give significantly higher error on the efficiency in the high-energy extrapolation region. Figure 47 shows the efficiency data for Ge2, the best-fit line to the data, the error range in the interpolation region, and the error range in the extrapolation region. It is noted

that the percent error in the interpolation region is roughly 8% of the efficiency whereas at 4000 keV, the percent error has increased to approximately 16% of the efficiency.

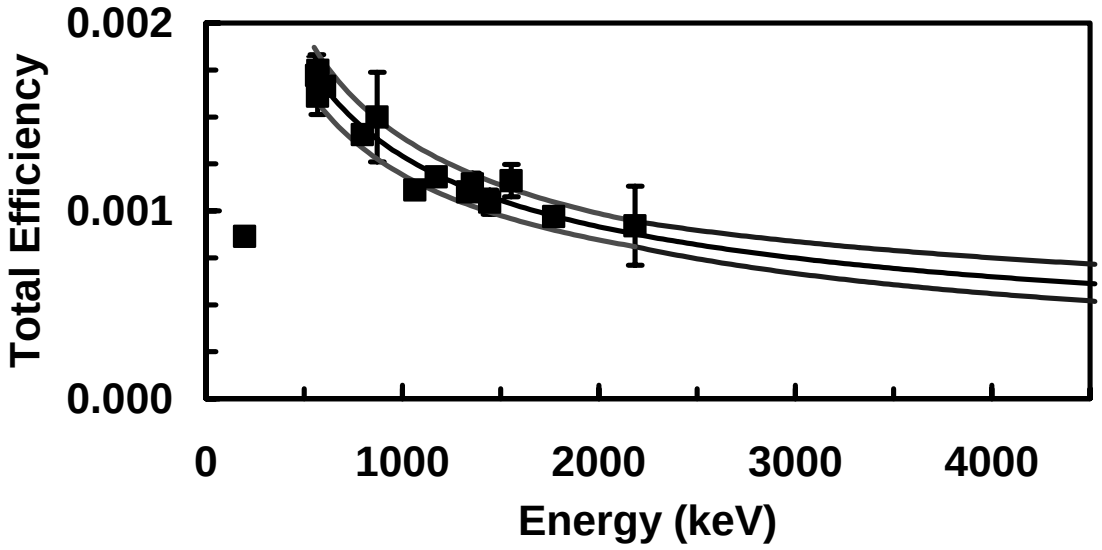

Figure 47 Efficiency calibration data for detector Ge #2 showing the interpolation and extrapolation error ranges (red and blue, respectively) as a function of gamma-ray energy.

3.9 GAMMA RAY INTENSITIES – ^{19}N

The branching ratios for gamma ray emission as a function of energy can be calculated for those transitions that were assigned as following the beta decay of ^{19}N. The integrated area of the gamma lines divided by the detector efficiency leads to the total number of gamma rays emitted over the course of the data runs. This value divided by the total number of decays (from the integrated half-life spectra) of the respective isotopes gives the intensity of the lines per decay of the parent isotope. Table 29 gives the energy of the gamma line, number of decays observed in each of Ge1 and Ge2, the efficiency of each detector at that energy, the total number of source decays, and the calculated intensity of each gamma line.

Table 29 Gamma ray absolute intensities for those transitions that can be ascribed to the beta decay of ^{19}N.

Energy (keV)	Ge1 Counts	Ge2 Counts	β-Source (x 1e-7)	εGe1 (x 1000)	εGe2 (x 1000)	Iγ Ge1 (x 1000)	Iγ Ge2 (x 1000)
96	25155	N/A	4.64(2)	1.86(51)	N/A	291(80)	N/A
821	1220	579	4.64(2)	2.75(22)	1.42(11)	10(1)	9(1)
1374	12455	5571	4.64(2)	2.22(20)	1.10(9)	121(13)	109(11)
1472	824	330	4.64(2)	2.15(18)	1.06(9)	8(1)	7(1)
1652	1426	635	4.64(2)	2.05(15)	1.01(7)	15(2)	14(2)
1938	845	394	4.64(2)	1.91(14)	0.93(7)	10(2)	9(2)
1980	15043	6735	4.64(2)	1.89(14)	0.92(7)	172(15)	158(14)
2473	7946	3513	4.64(2)	1.73(15)	0.82(8)	99(10)	92(10)
3136	3617	1602	4.64(2)	1.56(19)	0.72(9)	50(7)	48(7)
3849	8454	3614	4.64(2)	1.44(17)	0.66(8)	127(17)	118(16)
3945	1249	611	4.64(2)	1.42(19)	0.65(9)	19(3)	20(4)

3.9.1 GAMMA RAY INTENSITIES – ^{20}N

Due to the low production rate of ^{20}N relative to the other RIBs, the potential for missing gamma rays during the beam off period was substantial. To limit this effect, the relative intensities of the gamma rays ascribed to the decay of ^{20}N were determined using the data collected in the germanium detectors over all times. The inherent assumption in this portion of the analysis was that the relative efficiency of the germanium detectors as a function of energy is not affected by monitoring over all times.

Table 30 lists the peak areas, efficiencies, and calculated relative intensities for gamma rays observed in each of the germanium detectors over all times and assigned to the decay of ^{20}N. The intensities are relative to the 1674 keV line which is set to one hundred.

Table 30 Calculated relative intensities of gamma rays emitted during the decay of ^{20}N. The intensities are relative to the 1674 keV line that is set to 100.

Eγ keV	Ge #1 Counts	Ge #2 Counts	ε-Ge #1 (x 1000)	ε-Ge #2 (x 1000)	Iγ Ge #1 Relative	Iγ Ge #2 Relative
96	968(32)	N/A	1.86(51)	N/A	88(24)	N/A
1374	234(39)	93(32)	2.22(20)	1.10(9)	18(3)	15(5)
1674	1206(45)	565(26)	2.05(15)	1.00(7)	100(8)	100(8)
1814	74(13)	48(15)	1.97(20)	0.96(8)	6(1)	9(3)
1895	174(37)	74(12)	1.93(18)	0.94(8)	15(4)	14(3)
2394	155(26)	59(10)	1.76(16)	0.84(9)	15(3)	12(3)
2782	47(19)	12(5)	1.65(15)	0.78(9)	5(2)	4(2)

The results for the relative intensities of the lines are in close agreement between the two germanium detectors. The gamma lines at 96 and 1374 keV are characteristic of transitions in ^{19}O. These gamma rays indicate beta delayed neutron emission from ^{20}N leading to excited levels of ^{19}O rather than to the ground state.

To determine the absolute intensities, the stronger peaks that were integrable in the beam-off spectra collected by the germanium detectors were analysed. This permits the calculation of the absolute intensity at these energies due to the fact that it is during this time period when the beta decay of ^{20}N can be monitored quantitatively. Also, the

half life gated on the 96 and 1374 keV lines as they appear in the beam-off spectra confirm them as being due to the decay of ^{20}N. Table 31 gives the absolute intensities for some of the ^{20}N gamma ray lines using this method.

Table 31 Absolute intensity of gamma rays ascribed to the decay of ^{20}N.

Eγ keV	Ge #1 Counts	Ge #2 Counts	^{20}N β- /10^5	ε-Ge #1 (x 1000)	ε-Ge #2 (x 1000)	Iγ Ge #1 (x 1000)	Iγ Ge #2 (x 1000)
96	347(21)	N/A	7.6(1)	1.86(51)	N/A	246(69)	N/A
1374	74(16)	40(9)	7.6(1)	2.22(20)	1.10(9)	44(11)	48(12)
1674	421(23)	205(16)	7.6(1)	2.05(15)	1.00(7)	270(25)	270(29)
1895	32(8)	N/A	7.6(1)	1.93(18)	0.94(8)	22(6)	N/A
2394	57(15)	N/A	7.6(1)	1.76(16)	0.84(9)	43(12)	N/A

Taking the relative gamma intensities in concert with the smaller sub-set of measured absolute intensities, the absolute intensities for all of the lines for both detectors can be calculated. Since the 1674 keV line has the lowest error, this line's intensity was utilized to calculate the absolute intensity of the others. Table 32 gives the final evaluated intensities of the gamma lines due to ^{20}N.

Table 32 Intensity of the gamma-ray lines attributed to the decay of ^{20}N.

Eγ keV	Iγ Ge #1 Measured (x 1000)	Iγ Ge #1 Calculated (x 1000)	Iγ Ge #2 Measured (x 1000)	Iγ Ge #2 Calculated (x 1000)	Iγ Final (x 1000)
96	246(69)	-	-	N/A	246(69)
1374	44(11)	-	48(12)	-	46(9)
1674	270(25)	-	270(29)	-	270(19)
1814	-	16(4)	-	24(9)	18(4)
1895	22(6)	-	-	38(10)	26(6)
2394	43(12)	-	-	32(10)	37(8)
2782	-	13(6)	-	11(5)	12(4)

CHAPTER 4

INTERPRETATION

4.1 INTERPRETATION ^{19}N GAMMA RAYS

To determine the branching ratios for the beta decay of ^{19}N to bound excited states of ^{19}O, the transitions listed in table 29 of section (*) were assigned as either being due to transitions between states in ^{19}O or between states in ^{18}O. Table 33 lists those transitions assigned to ^{19}O along with their intensities and the characteristic levels of the transition. The intensities are given per 1000 parent decays.

Table 33 Gamma-ray transitions identified as being a result of ^{19}N beta decay to bound excited states of ^{19}O.

Energy (keV)	^{19}O Initial Level (keV)	^{19}O Final Level (keV)	Iγ Ge1 (x 1000)	Iγ Ge2 (x 1000)
96	96	0	291(80)	N/A
1374	1472	96	121(13)	109(11)
1472	1472	0	8(1)	7(1)
2473	3945	1472	99(10)	92(10)
3136	3232	96	50(7)	48(7)
3849	3945	96	127(17)	118(16)
3945	3945	0	19(3)	20(4)

From these data, it is possible to construct an energy level diagram illustrating the observed transitions. This will show which gamma rays must be in coincidence with each other and permit a determination of which levels are fed directly from the

beta decay and which gamma rays are consequences of cascades. Figure 48 shows the known energy level scheme for the ground state and bound excited states of ^{19}O. The levels are given in keV relative to the ground state at zero and are adapted from reference [tilley].

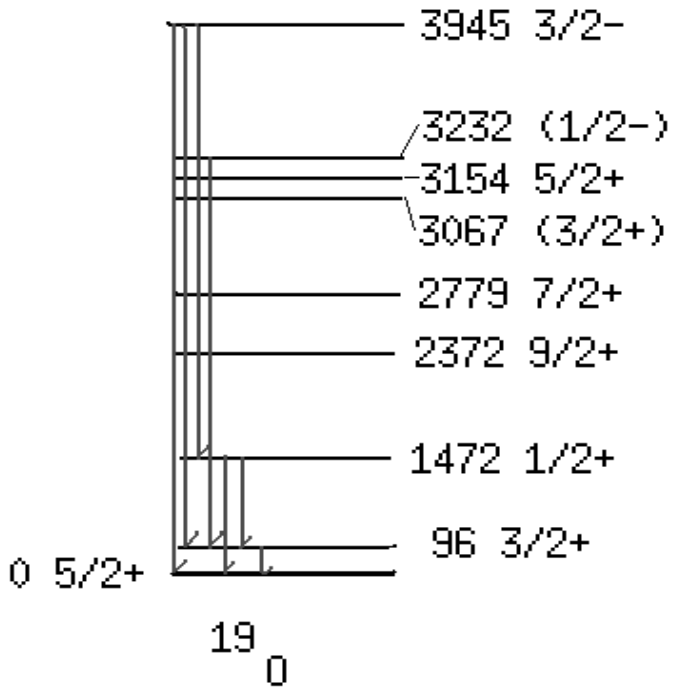

Figure 48 Partial energy level diagram of ^{19}O. Included are the bound state energy with spin and parity and the gamma transitions observed in this experiment.

To deduce the branching ratios for the beta decay of ^{19}N to bound states of ^{19}O, the intensities of those transitions that are not fed by a cascade remain unchanged. Those transitions that may be due to both beta feeding and as a result of one or more gamma-ray cascades require that their intensities be adjusted for the cascade feeding. In this case, the only transitions that may be due to both beta feeding and cascade feeding are the 1472-0, 1472-96, and 96-gs transitions. Unfortunately, the experimental

conditions prevented a determination of the germanium detector efficiency near 96 keV for detector Ge#2. Consequently, there can be no redundancy for the calculation of the beta feeding to the 96 keV level during the decay of ^{19}N.

From the observed intensities and the derived decay scheme, the branching ratios for pure beta feeding to bound excited states of ^{19}O can be calculated. The sum of the three transitions proceeding from the 3945 keV level is a measure of the beta strength to this level. The intensity of the 3232-1472 transition is a measure of the beta decay branching ratio to the 3232 keV level, and the sum of the 1472-gs and 1472-96 transitions, less the feeding through cascades, is a measure of the beta decay to the 1472 keV excited state. Similarly, the intensity of the 96 keV gamma ray less the cascade feeding from multiple sources will be a measure of the beta branch to the 96 keV level. Table 34 gives the calculated direct beta-decay branching ratios to bound excited states of ^{19}O where soluble. The last row of the table gives the total branching ratio to bound excited states of ^{19}O above and not including the 96 keV level.

Table 34 Bound levels in ^{19}O populated during the decay of ^{19}N. Listed are the branching ratios for the transitions as determined from the gamma-ray data collected by the germanium detectors.

Beta Decay Level Populated Directly	Branching Ratio (%) Germanium #1	Branching Ratio (%) Germanium #2
3945 3/2-	23.9(20)	23.0(20)
3232 (1/2-)	5.0(10)	4.8(7)
1472 1/2+	0.30(18)	0.24(16)
96 3/2+	< 4.3	N/A
Ground State 5/2+	N/A	N/A

TOTAL B.R.	29.2(23)	28.1(23)

The branching ratio determination for direct beta feeding to the ^{19}O first excited state at 96 keV is given as an upper limit. The branching ratio calculated from the 96 keV line's intensity less the feeding is consistent with zero. The upper limit represents subtracting the minimum possible cascade contribution (mean less one sigma) from the maximum possible intensity (mean plus one sigma) of the 96 keV line. This experiment was not sensitive to the beta decay of ^{19}N feeding the ground state of ^{19}O directly.

4.2 POTENTIAL PROBLEM WITH BOUND STATE FEEDING RESULTS

The efficiency calibration of the germanium detectors is suspect for the higher energy gamma rays due to the fact that the calibration data cover a range having an upper limit of 2200 keV or thereabouts. The efficiencies quoted for the >3.0 MeV gamma rays are extrapolations over an extremely large span. For the case of the 3232 keV gamma line, there is no alternative to the extrapolation. However, the 3945 keV level in ^{19}O has been populated in the past and the subsequent de-excitation of this level has been monitored []. From the independence hypothesis, the de-excitation of a level should not be dependent on the manner by which it is populated – provided there is no polarization component. Therefore, since the de-excitation gamma rays and their intensity have been recorded in the past, this provides an opportunity to determine the branching ratios by other means. Table 35 lists the data from the literature relevant to the relaxation of the 3945 keV level in ^{19}O.

From our own data, the calibration of the detector efficiency for the 2473 keV line is considered reliable. The reliability was checked by a comparison of our

extrapolation against data recorded by the germanium detectors during a different NSCL experiment [] having a calibration point at 2615 keV. The agreement between the shapes of the calibration curves above 500 keV for both experiments improved the confidence for the efficiency value at 2473 keV derived in this work.

Table 35 Literature values for the de-excitation branching of the 3945 keV excited state of ^{19}O.

Initial Level (keV)	Final Level (keV)	Gamma Energy (keV)	De-excitation Branch (%) [*]	De-excitation Branch (%) [*]
3945	0	3945	24(8)	33(8)
3945	96	3849	48(8)	39(8)
3945	1472	2473	28(4)	28(4)

Accepting the efficiency at 2473 keV as valid, and utilizing the relative de-excitation strength of the 3945 keV level from the literature, extrapolating the efficiency of the germanium detectors for the 3945 and 3849 keV levels is obviated. Table 36 gives the calculated intensities for the 3945 and 3849 keV levels on the basis of the literature data and the subsequent beta decay branching ratio to the 3945 keV level.

Table 36 Calculated intensities of the de-excitation gamma rays from the 3945 keV excited state of ^{19}O and the inferred beta feeding to that state through the decay of ^{19}N.

Ge #1	Iγ 2473 keV (fixed)	Iγ 3945 Calculated	Iγ 3849 Calculated	^{19}N β-Branch 3945 keV (%)
Reference [ ]	99(10)	85(32)	170(41)	35.4(53)
Reference [ ]	99(10)	117(35)	138(37)	35.4(52)
Ge #2				

Reference [ ]	92(10)	79(30)	158(39)	32.9(51)
Reference [ ]	92(10)	108(33)	128(35)	32.8(50)

The salient feature of this method to determine the intensity of the higher energy gamma rays is that the value for the total beta branch into the 3945 keV level is significantly higher than what has been calculated using the extrapolated efficiency calibration. This suggests that the efficiency extrapolation results in a value that is higher than the true value. Such a discrepancy is entirely reasonable due to the fact that the potential for single and double escape increases rapidly above 2500 keV. This would substantially alter the functional form of the general efficiency curve above 2500 keV [] thus reducing the detection efficiency relative to the extrapolation.

The Tilley et al. reference, which is a compilation of the previously published experimental results, states that the de-excitation values given in [] are considered to be more reliable that that of reference []. Assuming this to be true, the total beta decay branching ratio for ^{19}N populating bound excited states above the 96 keV level will be 40.7(54) for Ge1 and 38.0(53) for Ge2. Table 37 summarizes the results of the gamma-ray branching ratio determination. The total branching ratio does not include the upper limit for the direct beta decay to the 96 keV excited level.

Table 37 Summary of beta decay strength to individual bound levels in ^{19}O from the decay of ^{19}N.

Beta Decay Level Populated Directly	Branching Ratio (%) Germanium #1	Branching Ratio (%) Germanium #2	B.R. (%) Mean Value
3945 3/2-	35.4(52)	32.9(51)	34.2(37)
3232 (1/2-)	5.0(10)	4.8(7)	4.9(6)
1472 1/2+	0.30(18)	0.24(16)	0.27(12)
96 3/2+	< 4.3	N/A	<4.3

Ground State 5/2+	N/A	N/A	N/A
TOTAL B.R.	40.7(54)	38.0(53)	39.4(38)

Due to the lack of confidence in the efficiency extrapolation, the value quoted for the beta-decay branching ratio to the bound excited state at 3945 keV will be that derived on the basis of the previously published experimental results of reference [].

4.3 INTERPRETATION OF ^{19}N DELAYED NEUTRONS

Between the neutron bars and the ^{6}Li detectors, the experiment was able to record twelve beta-delayed neutrons emitted during the decay of ^{19}N. Table 38 summarizes the observed delayed neutrons and the calculated branching ratio for each transition.

Table 38 Summary of observed delayed-neutron transitions from ^{19}N by energy.

Neutron Energy (MeV)	B.R. (%) from Array	B.R. (%) from ^{6}Li glass
4.91	0.90(10)	-
4.00	0.37(4)	-
3.06	1.97(32)	-
2.84	9.6(11)	-
2.49	3.5(4)	-
2.21	2.2(4)	-
1.27	1.9(2)	-
1.13	16.2(17)	18.2(23)
0.83	2.0(3)	-
0.62	2.2(3)	-
0.49	8.7(10)	8.6(10)

0.30	-	1.4(3)

To determine the beta branching to specific excited levels of ^{19}O that subsequently emit a neutron, it is necessary to determine if the neutron emission populates the ^{18}O ground state or one of the excited states. There is about 8.5 MeV available for delayed neutron emission and over twenty excited states in ^{18}O that could possibly be populated following the emission of a neutron from an excited level of ^{19}O.

The analysis of the gamma-ray data collected by the germanium detectors showed that there were four gamma rays characteristic of transitions in ^{18}O. These gamma rays could be indicative of beta-delayed neutron emission populating excited states of ^{18}O or they could simply be due to the beta decay of an ^{18}N contaminant. If the ^{18}O gamma rays are due to ^{19}N delayed neutron emission then the corresponding half lives of the gamma rays should be equal to the half life of ^{19}N (~300ms) and if the ^{18}O gamma rays are due to the beta decay of ^{18}N then the gated half lives will reflect the half life of ^{18}N (~620ms). Table 39 gives the measured half lives of the four ^{18}O gamma rays and the intensity of the lines for the measurements made by each of the germanium detectors. The intensities of the gamma rays are given per 1000 ^{19}N decays.

Table 39 Gamma rays characteristic of de-excitation in ^{18}O. The half lives of the gamma rays are listed along with the intensity of the lines assuming the ^{19}N parent.

Eγ keV	E_i level ^{18}O	E_f level ^{18}O	Half Life (ms)	Iγ Ge #1	Iγ Ge #2	Iγ Mean
1982	1982	0	300(10)	172(15)	158(14)	166(10)
1938	3920	1982	273(17)	10(2)	9(2)	10(2)
1652	3634	1982	305(14)	15(2)	14(2)	15(2)

821	4456	3634	364(45)	10(1)	9(1)	10(2)

On the basis of the measured gamma-ray half lives, it may be concluded that the observed ^{18}O gamma rays are indeed due to the decay of ^{19}N and thus reflect delayed neutron emission to excited states of ^{18}O. Accounting for the cascade feeding in the same manner as outlined in section (*), and incorporating level schemes from [], the branching ratios for delayed neutron emission populating the specific excited states of ^{18}O may be calculated. Table 40 gives the total strength of the (beta+neutron) feeding of the ^{18}O excited levels.

Table 40 Values for the (beta + n) feeding strength to each of the pertinent ^{18}O excited states.

^{18}O Excited State Populated (keV)	Beta + Neutron Feeding Strength (% of ^{19}N decays)
1982	13.7(11)
3634	0.1(3)
3920	1.2(3)
4456	1.5(4)

To determine the beta feeding to specific levels in ^{19}O prior to the neutron or gamma ray emission, it is desirable to find which delayed neutrons are in coincidence with the ^{18}O gamma rays that were observed. An effort was made to measure, directly, which neutrons and gammas correspond to the same transition by gating on the gamma rays of table 40 and reflecting back onto the (summed) delayed neutron spectrum

recorded by the neutron bar array. Table 41 gives the results of the coincidence measurement for each of the gamma rays gated.

Table 41 Neutrons in coincidence with selected ^{18}O gamma rays. Listed are those neutrons in coincidence and those neutrons that may be in coincidence on the basis of the gated spectrum.

Gamma-Ray Gate (keV)	Neutron in Coincidence (keV) Definite	Neutron in Coincidence (keV) Possible
1982	2840	490
	830	2210
		1270
1653	1270	
1938	830	
821	None	None

On the basis of these results, it can be concluded that the 830 keV neutron is emitted by from a level in ^{19}O that populates the 3920 keV excited state of ^{18}O due to the fact that this neutron appears to be in coincidence with both the 1938 and 1982 keV gamma lines. Also, the 1270 keV neutron appears to be in coincidence with the 1653 keV gamma ray – suggesting that the beta delayed neutron populates the 3634 keV excited state or perhaps the 4456 keV excited state. It is not possible to distinguish between the two given the statistics of the (821 keV gamma ray gated) neutron spectrum. Also, the strong 2840 keV neutron is in coincidence with the 1982 keV gamma ray suggesting that this neutron is emitted by a level in ^{19}O that populates the first excited state of ^{18}O. The 2210 and 490 keV neutrons may or may not be in coincidence with the 1982 keV gamma line. The low statistics of the coincidence spectra prevent conclusive assignment of these neutrons to the gamma ray.

4.4 DELAYED NEUTRON ASSIGNMENTS ^{19}N

From the delayed neutron branching ratios, observed ^{18}O gamma rays and the measured neutron + gamma ray coincidences, a cross table for the possible delayed neutron transitions may be constructed (Table 42). The cross table cells represent the energy of the intermediate ^{19}O level populated by the beta decay and emitting the neutron. The columns define the level of ^{18}O populated following the emission of the neutron. The energies are given in keV for all entries and the cell values are relative to the ground state of ^{19}O. Those cells that are blank have been eliminated as possible transitions either on the basis of the total energy (greater that that available for delayed neutron emission) or on the basis of the neutron branching ratio relative to the ^{18}O gamma-ray intensities. Since there is no evidence of any ^{18}O levels being populated other than those listed in table 41, the cross table (42) will be limited to those excited states plus the ^{18}O ground state.

Of the twelve delayed neutron transitions, only five can be conclusively assigned to specific levels in ^{19}O. These delayed neutron energies and corresponding ^{19}O level are underlined in the cross table. The remaining seven cannot be fixed as they may proceed through different intermediate states on the basis of the measured data. From the delayed neutron branching ratios and the definitive assignments it can be concluded that the small possible branch for delayed neutrons populating the 3634 keV excited level in ^{18}O is either in fact zero (with which the measurement is consistent) or is a result of a delayed neutron that was not measured in our experiment.

Table 42 Cross table for the assignment of intermediate states of ^{19}O populated during the decay of ^{19}N.

E-Neutron C.o.M.	E-^{19}O level (^{18}O gs)	E-^{19}O level (^{18}O 1982)	E-^{19}O level (^{18}O 3634)	E-^{19}O level (^{18}O 3920)	E-^{19}O level (^{18}O 4456)
4910	8867	10849			
4000	7957	9939			
3060	7017	8999			
2840		8779			
2490	6447	8429			
2210	6167	8149			
1270					9683
1130	5087				
830				8707	
620	4577				
490	4447	6429			
300	4257	6239			

4.5 INTERPRETATION OF ^{20}N GAMMA RAYS

To determine the branching ratios for the beta decay of ^{20}N to bound excited states of ^{20}O, the transitions labeled in table 32 of section (*) were assigned as either

being due to transitions between states in ^{20}O or between states in ^{19}O. Table 43 lists those transitions indicative of beta decay to bound states of ^{20}O.

Table 43 Gamma-ray transitions identified as being a result of ^{20}N beta decay feeding bound excited states of ^{20}O.

Gamma Energy keV	^{20}O Initial Level	^{20}O Final Level	Intensity (x 1000)
1674	1674	0	270(19)
1814	5387	3570	18(4)
1895	3570	1674	26(6)
2394	4072	1674	37(8)
2782	4456	1674	12(4)

From these data it is possible to construct and energy level diagram illustrating the observed transitions among the known ^{20}O levels. As with the ^{19}N data, this will make it possible to determine the cascade feeding and thus lead to an assessment of the branching ratios for the feeding of specific levels in ^{20}O during the beta decay. Figure 49 shows the gamma transitions in ^{20}O observed in this experiment.

From the observed intensities and the derived decay scheme, the branching ratios for pure beta feeding to specific bound levels in ^{20}O can be calculated. Table 44 gives the result of the branching ratio determination for the decay of ^{20}N to bound excited levels in ^{20}O.

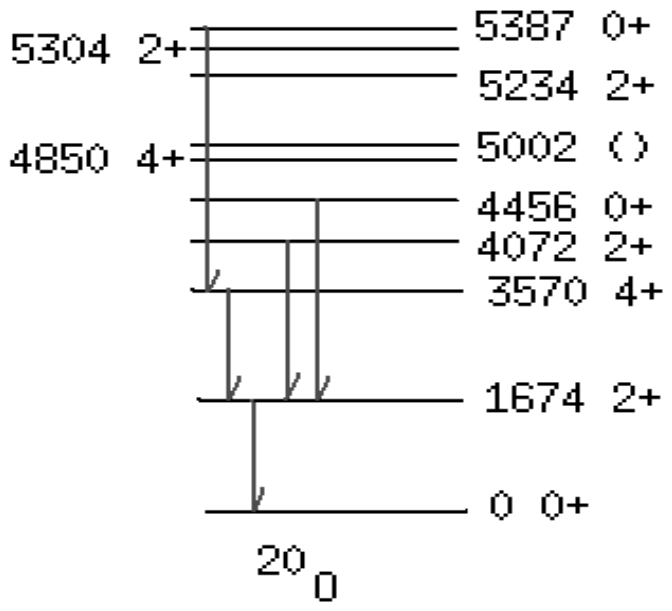

Figure 49 Partial energy level diagram of ^{20}O. Included are the bound-level energy, with spin and parity, along with the transitions observed in this experiment.

Table 44 Bound excited levels of ^{20}O populated during the decay of ^{20}N. Listed are the branching ratios for the beta transitions as determined from the measured gamma-ray data.

^{20}O Excited Level Populated Directly	Branching Ratio of Direct β-Feeding
Energy of Level (keV)	(Percent)
5387 0+	1.8(4)
4456 0+	1.2(4)
4072 2+	3.7(8)
3570 4+	0.8(8)
1674 2+	19.5(22)
G.S. 0+	N/A
Total Branching Ratio	27.0(46)

4.6 INTERPRETATION OF ^{20}N NEUTRON SPECTRUM

Analysis of the delayed neutron spectrum collected by the neutron bar array suggests eight beta delayed neutrons emitted by the ^{20}N isotope. Table 45 lists the energy of those delayed neutrons and their corresponding branching ratios. Taking the data together, the delayed neutron emission probability from ^{20}N is 34.0(40) percent of the decay strength for delayed neutrons above 1.1 MeV in energy. The low rate and decreasing detection efficiency of the array below this cut off prevent measurement of delayed neutrons at lower energy.

Table 45 Energy and branching ratio for delayed neutrons observed during the decay of ^{20}N. Also given is the P_n value for delayed neutrons emitted above 1.1 MeV in energy.

Energy of ^{20}N Delayed Neutron (Center-of-Mass MeV)	Branching Ratio (Percent)
1.16	4.5(5)
1.33	2.5(3)
1.63	8.3(9)
2.19	12.1(13)
2.63	1.3(2)
3.38	2.1(3)
3.88	2.7(3)
4.64	0.5(1)
TOTAL	**34.0(40)**

The gamma-ray spectra collected during the decay of ^{20}N showed two gamma rays at 96 and 1374 keV - which are characteristic of transitions in ^{19}O. The first a transition from the 96 keV first excited state to the ground state and the second a transition from the 1472 keV second excited state to the 96 keV level. These gamma rays were shown to have half-lives consistent with that of ^{20}N indicating that there is beta delayed neutron emission from ^{20}N populating excited levels in ^{19}O rather than the ground state. The branching ratios for these transitions, with cascade feeding taken into account, are 20.0(70) and 4.6(9) percent for the 96 and 1374 keV transitions, respectively.

With regard to delayed neutron emission from ^{20}N, it is not possible to assign beta decay branching ratios to specific excited levels of ^{20}O above the neutron emission threshold. This is due to the following considerations: first, several possibilities exist for the final ^{19}O level populated rendering the evaluation of the level energy inconclusive, second, the implantation rate of ^{20}N coupled with the detection efficiencies prevent neutron-gamma coincidence measurements that could restrict the ^{20}O level energy, third, only seven ^{20}O excited levels above the neutron emission threshold are known with but four of these being above the lowest experimentally observed neutron energy, and fourth, the extent of the above-threshold levels is below 10.5 MeV relative to the ground state of ^{20}O while the Q-value is about 18 MeV.

The one exception to this is the 2.19 MeV delayed neutron peak. The intensity of this transition is strong enough that the coincidence between it and the 96 keV should have been observed. The spectrum, however, does not indicate a coincidence between the two - suggesting that the delayed neutron emission populates the ground state of ^{19}O

rather than the 96 keV excited state. Furthermore, one of the known ^{20}O levels is at 9.77 MeV (~2.17 MeV above the neutron emission threshold) which is consistent in energy with the 2.19 MeV neutron observed. Thus, this transition is tentatively assigned as proceeding through the 9.77 MeV level in ^{20}O with a branching ratio of 12.1(13) percent.

4.7 ^{19}N SHELL MODEL CONSIDERATIONS

From the energies of the ^{19}O intermediate levels that may be populated directly in the ^{19}N beta decay and the measured branching ratios of the transitions, the log(ft) values of the specific transitions can be calculated. The log (ft) values provide insight into the nature of the decay (allowed etc…) and also lead to a determination of the B(GT) transition strength. The log (f) values are taken from the literature [] while the t value is simply equal to the half life of ^{19}N in seconds divided by the measured branching ratio of the specific channel expressed as a transition probability (BR/100). The B(GT) strength is equal to (6177/ft).

Table 46 lists all transitions observed in this experiment (delayed neutron as well as beta decay to bound states of ^{19}O), the experimentally derived transition strength, the log (ft) values and the calculated B(GT) strength. The column labeled "transition identifier" gives the energies of the delayed neutrons for the (β+n) transitions while "to bound" indicates a transition to the bound ^{19}O level listed in the second column. For those cases where the delayed-neutron emitting state is not conclusive, all possibilities are shown based on the delayed neutron energy.

Table 46 Calculated log(ft) and B(GT) values for the possible beta transitions in the decay of ^{19}N. The transition probability is the branching ratio divided by 100.

Transition Identifier	^{19}O level Populated	Transition Probability	Log (ft)	B(GT)
(β+n) 4910	8867	0.009	4.65	1.37E-01
(β+n) 4910	10849	0.009	3.20	3.87
(β+n) 4000	7957	0.0037	5.49	2.00E-2
(β+n) 4000	9939	0.0037	4.39	2.52E-1
(β+n) 3060	7017	0.0197	5.13	4.55E-2
(β+n) 3060	8999	0.0197	4.25	3.45E-1
(β+n) 2840	8779	0.0964	3.68	1.28
(β+n) 2490	6447	0.0349	5.08	5.09E-2
(β+n) 2490	8429	0.0349	4.30	3.07E-1
(β+n) 2210	6167	0.0224	5.37	2.65E-2
(β+n) 2210	8249	0.0224	4.57	1.67E-1
(β+n) 1270	9683	0.0189	3.87	8.32E-1
(β+n) 1130	5087	0.1618	4.83	9.18E-2
(β+n) 830	8707	0.0202	4.40	2.45E-1
(β+n) 620	4577	0.0215	5.83	9.04E-3
(β+n) 490	4447	0.0869	5.27	3.33E-2
(β+n) 490	6429	0.0869	4.70	1.24E-1
(β+n) 300	4257	0.014	6.11	4.78E-3
(β+n) 300	6239	0.014	5.55	1.74E-2
to bound	3945	0.342	4.79	9.95E-2
to bound	3232	0.049	5.81	9.64E-3
to bound	1472	0.0027	7.39	2.54E-4
to bound	96	0.043	6.42	2.33E-3
to bound	0	n/a	n/a	n/a

Shell model calculations to predict the Gamow-Teller beta decay strengths of ^{19}N to levels in ^{19}O were calculated by Warburton in reference []. In the model, the even parity states of ^{19}O were calculated within the $(0s)^4(0p)^{12}(2s,1d)^3$ model space, the ^{19}N states were assumed to arise from the $(0s)^4(0p)^{11}(2s,1d)^4$ model space, and the odd parity ^{19}O levels required consideration of both the $(0s)^4(0p)^{11}(2s,1d)^4$ component and the $(0s)^4,(0p)^{12}(2s,1d)^2(0f,1p)^1$ component to account for all possible 1$\hbar\omega$ excitations. The model uses a modified Millener-Kurath interaction to calculate the odd-parity

levels in ^{19}O and the Chung-Wildenthal or Universal (2s1d) interaction for the low-lying even-parity levels.

Table 47 compares the transitions observed in this experiment with the predictions of the shell model calculations of Warburton. The table, where necessary, identifies transitions by subscript that cannot be conclusively ascribed to the specific level in ^{19}O. Tabulated are the branching ratio, log(ft), B(GT), and level spins for each observed or calculated transition.

Table 47 Comparison of the ^{19}O energy levels from this experiment with predictions made using the shell model []. The subscripts on the experimental energy levels indicate the two choices for the ^{19}O level due to the uncertainty in the delayed neutron decay. The tabulated B(GT) values have been multiplied by a factor of 1000.

This Experiment					Shell Model Predictions				
Ex	Jp	BR%	Logft	B(GT)	Ex	Jp	BR%	Logft	B(GT)
96	3/2+	<4.3	6.42	2.3	96	3/2+	0.49	7.30	
1472	½+	0.27	7.39	0.25	1472	1/2+	4.88	6.06	
3232	½,3/2	4.9	5.81	9.6	3232	1/2-	1.1	6.77	1.0
3945	½,3/2	34.2	4.79	99.5	3945	3/2-	6.2	5.86	8.5
4257_1		1.4	6.11	4.8					
4447_2		8.7	5.27	33.3					
4577		2.2	5.83	9.0	4582	3/2-	3.4	5.97	6.6
5087		16.2	4.83	245.0	5082	1/2-	39.2	4.77	103.6
6167_3		2.2	5.37	26.5					
6239_1		1.4	5.55	17.4					
6429_2		8.7	4.7	124.0					
6447_4		3.49	5.08	50.9					
					6755	3/2-	12.7	4.75	109.3
7017_5		2.0	5.13	45.5					
					7119	3/2-	4.3	5.08	50.6
					7509	3/2-	12.2	4.49	200.1
					7622	1/2-	1.3	5.42	23.3
					7843	3/2-	3.7	4.87	82.7
7957_6		0.37	5.49	20.0					
					8196	3/2-	5.4	4.55	172.6
8249_3		2.24	4.57	167.0					
8429_4		3.49	4.30	307.0					
					8505	1/2-	3.6	4.57	166.9
					8506	3/2-	2.5	4.74	111.2
8707		2.02	4.40	245.0					
8779		9.64	3.68	1280					
8867_7		0.9	4.65	137.0					
8999_5		1.97	4.25	345.0					
9683		1.89	3.87	832.0					
9939_6		0.37	4.39	252.0					
10849_7		0.9	3.20	3870					

4.8 BETA DECAY OF ^{20}N

For the beta decay of ^{20}N feeding bound excited levels of ^{20}O and the one delayed neutron transition assignment, it is possible to determine both the log(ft) and

B(GT) values for the specific transitions. The Q value of the ^{20}N ground state to ^{20}O ground state transition is known to be 17.97 MeV. From this quantity, the branching ratios and the half life measurement, the log(ft) and B(GT) values were calculated. Table 48 gives the results of these calculations.

Table 48 Calculated log(ft) and B(GT) values for specific decays assigned to the decay of ^{20}N. The transition identifier segregates beta decay to bound states from the delayed neutron emitting level.

Transition Identifier	^{20}O level keV	Transition Probability	Log(ft)	B(GT) (x 1000)
(β + n) 2190	9770	0.121(13)	4.7	123
To bound	1674	0.195(22)	5.9	8
To bound	3570	0.008(8)	7.1	0.5
To bound	4072	0.037(8)	6.3	3
To bound	4456	0.012(4)	6.8	1
To bound	5387	0.018(4)	6.4	2.5

The log(ft) values are consistent with first forbidden beta transitions. This leads to the conclusion, since 0+ and 2+ levels are populated, that the spin and parity of the ^{20}N ground state is low (1- or 2-) and most likely equal to (1-).

4.9 ASTROPHYSICS RESULTS

To deduce the probability and relative strengths of astrophysical reactions, and thus the rates of isotopic production, the most important quantity to determine, on a reaction-by-reaction basis, is the reaction rate per particle pair, $\langle\sigma v\rangle$. This quantity incorporates, into the reaction rate, changes in the cross section as a function of energy where the energy, in itself a temperature dependent distribution, is based on the particular astrophysical environment. Mathematically, $\langle\sigma v\rangle$ is given by the expression:

$$\langle \sigma v \rangle = (8/\pi\mu)(kT)^{-3/2} \int_0^\infty \sigma(E) E \exp(-E/kT) dE$$

where σ is the cross section, v is the velocity, μ is the reduced mass, k is the boltzmann constant, and T is the temperature of the system.

The above expression is completely general though, typically, reaction cross sections are separated into direct capture and resonant capture components. The separation is permissible due to the fact that all of the non-trivial differences between the direct and resonant components resides in the σ(E) term of the integral. Thus, rewriting the total cross section σ(E) as a sum of the σ(E) components affects the equation only by expanding the integral into a sum of component integrals. The total cross section <σv>, then, may be expressed as [ozawa]:

$$\langle \sigma v \rangle = \langle \sigma v \rangle_{dc} + \langle \sigma v \rangle_{res}$$

where the subscripts dc and res refer to direct capture and resonant capture, respectively.

4.9.1 DIRECT CAPTURE CONTRIBUTION TO THE $^{18}O(n,\gamma)^{19}O$ REACTION RATE

For neutron induced astrophysical reactions, such as the (n,γ) reaction that is of interest here, determining the direct capture component to the overall rate is somewhat simpler than for rates involving charged particles. The reason this is so is due to the fact that penetrability considerations, generally associated with coulombic interactions or tunneling phenomena, are either non-existent or greatly reduced where neutrons are involved. For example, the absorbtion of (l=0) or s-wave neutrons by a target nucleus is not hindered by a barrier to its penetration (penetrability = 1). Of course, even higher order neutron partial waves (l>0) do not experience a typical coulombic barrier, however they are weakly hindered by an angular momentum barrier which is a function

of the system's reduced mass and the interaction energy. Even so, the angular momentum barrier is effectively much lower than the barrier to charged particles and furthermore, can be approximated by a simple mass and energy relation. For p-wave (L=1) neutrons, the penetrability is approximated by:

$$P_1 = \mu^{1/2} E^{3/2}$$

The direct capture cross section $<\sigma v>_{dc}$ can be solved as a Maclaurin series expansion in $E^{1/2}$ about zero energy. The result in terms of $<\sigma v>_{dc}$ takes on the form [Fowler, rolfs]:

$$<\sigma v>_{dc} \quad = \quad S(0)\left[1+0.3312\frac{S'(0)}{S(0)}T_9^{1/2}+0.06463\frac{S''(0)}{S(0)}T_9\right]$$

where the constant S and its derivatives are parameters of the expansion and can be determined experimentally [fowler], the derivatives of S are with respect to $E^{1/2}$, and T_9 is the temperature in billions of degrees Kelvin.

For our particular reaction of interest, the $^{18}O(n,\gamma)^{19}O$ reaction, the values of the constant S and its derivatives are tabulated in []. Using these values, the direct capture cross section $<\sigma v>_{dc}$ can be calculated for the $^{18}O(n,\gamma)^{19}O$ reaction. The result yields:

$$<\sigma v>_{dc} \quad \cong \quad 4.60\cdot 10^{-21} T_9 \; cm^3/\sec$$

for temperatures of ($T_9 > 0.01$). However, it is noted that the values of the constants given in [fowler] are the arbitrary estimates of the author. These estimates were made prior to the measurement of the thermal neutron absorption cross section of ^{18}O and are reported with an uncertainty of a factor of two.

In addition to the method of calculating the direct capture cross section as above, the direct capture cross section $\langle \sigma v \rangle_{dc}$ may be approximated by the sum of the s-wave (l=0) and p-wave (l=1) components such that [rauscher]:

$$\langle \sigma v \rangle_{dc} = \langle \sigma v \rangle_{dc,s} + \langle \sigma v \rangle_{dc,p}$$

Determining the s-wave part of the total cross section $\langle \sigma v \rangle_{dc,s}$ takes advantage of the so-called 1/v law where it holds that the product $\sigma_n v_n$ is a constant over all energies [rolfs]. Therefore, knowing the cross section at *any* energy provides knowledge of the cross section at *all* energies for the s-wave part of the interaction. Since the thermal neutron absorption cross section is known for ^{18}O [rauscher], the s-wave component $\langle \sigma v \rangle_{dc,s}$ can be found from the expression [Fowler]:

$$\langle \sigma v \rangle_{dc,s} = 2.20 \cdot 10^{-19}\ \sigma(thermal) \quad cm^3/\sec$$

taking the experimental value of σ(thermal) to be 1.60 x 10^{-4} barns, the calculated s-wave portion of the direct capture cross section becomes:

$$\langle \sigma v \rangle_{dc,s} = 3.52 \cdot 10^{-23}\ cm^3/\sec$$

To determine the p-wave component of the direct capture cross section, $\langle \sigma v \rangle_{dc,p}$, the expression:

$$\langle \sigma v \rangle_{dc,p} = 1.787 \cdot 10^{-16} S_n T_9 \quad cm^3/\sec$$

from Rauscher et al [] was used. In this expression, the S_n term is the S-factor for p-wave neutrons given in units of (barn $MeV^{-1/2}$). This term incorporates all of the strictly nuclear properties of the cross section into one expression where the cross section and the S-factor are related by:

$$\sigma(E) = S_n(\mu E)^{1/2}$$

The approximation for the penetrability of p-wave neutrons (equation %) has been folded into the expression. The value of S_n for the $^{18}O(n,\gamma)^{19}O$ reaction has been measured experimentally and is listed in table 7 of reference [rauscher]. Given that:

$$S_n = 52.4 \cdot 10^{-6} \quad \mu barns / MeV^{1/2}$$

the p-wave component of the direct capture cross section can be calculated as:

$$< \sigma v >_{dc,p} = 9.36 \cdot 10^{-21} T_9 \quad cm^3 / \sec$$

Thus, the total direct capture cross section $<\sigma v>_{dc}$ for the $^{18}O(n,\gamma)^{19}O$ reaction as calculated from the sum of the s-wave and p-wave components is then:

$$< \sigma v >_{dc} = < \sigma v >_{dc,s} + < \sigma v >_{dc,p} = 3.52 \cdot 10^{-23} + 9.36 \cdot 10^{-21} T_9 \quad cm^3 / \sec$$

The large p-wave cross section relative to the s-wave is most probably due to direct p-wave capture into the first excited, 96 keV level ($3/2^+$) of ^{19}O.

Because the parameters given in [fowler] are arbitrarily assigned and because the parameters listed in [rauscher] are determined through experiment, the value of $<\sigma v>_{dc}$ calculated in the above equation is considered more reliable than that of equation (*). Thus, the result generated by equation (*) will be the value incorporated into the expressions for the total reaction cross section from here forward.

4.9.2 RESONANT CAPTURE OF THE $^{18}O(n,\gamma)^{19}O$ REACTION RATE

In addition to the direct capture of neutrons by a nuclide, there is the possibility of neutron absorption through resonances in the reaction product. The strength of resonant capture depends on the relative energy of the level with respect to the unbound system, the temperature or energy distribution of the incident neutrons, the resonant widths of the entrance and exit channels and, the spin/parity of the resonance and target

nuclide. The functional form of the equation used to determine the resonant part of the cross section, $<\sigma v>_{res}$, is given as [ozawa, rolfs, rauscher,fowler]:

$$< \sigma v >_{res} \quad = \quad 2.557 \cdot 10^{-13} (\omega\gamma)_r \, A^{-3/2} \, T_9^{-3/2} \, Exp(-11.605 \, E_r / T_9) \quad cm^3 / \sec$$

where A is the reduced mass in atomic mass units, E_r is the center of mass energy of the resonance in MeV, and $(\omega\gamma)_r$ is the resonance strength in MeV.

The resonance strength $(\omega\gamma)_r$ is the product of a statistical factor and the gamma width of the resonance (Γ_γ). Mathematically, the value is given by:

$$(\omega\gamma)_r \quad = \quad (2J_r + 1)/[(2J_T + 1)(2J_P + 1)] \quad \bullet \quad \Gamma_\gamma$$

Where the J values are for the resonance, target nuclide ground state, and projectile, and the gamma width (Γ_γ) is in units of eV. For the case of the $^{18}O(n,\gamma)^{19}O$ reaction rate, the target spin is 0 (^{18}O ground state spin), the neutron projectile spin is ½ (incident neutron), and the gamma width is expected (Γ_γ) to be less than 1 eV from the systematics []. Consequently, the value for $(\omega\gamma)_r$ can be calculated to be:

$$(\omega\gamma)_r \quad \leq \quad (2J_r + 1)/2 \quad \bullet \quad 10^{-6} \, MeV$$

with J_r being the spin of the resonance in ^{19}O absorbing the incident neutron.

To assess the upper limit on the resonance contribution to the $^{18}O(n,\gamma)^{19}O$ reaction proceeding through the states observed in this experiment, all observed neutrons were assumed to populate the ground state in ^{18}O. This minimizes the resonance energy and thus maximizes the potential contribution to the reaction. Also, the beta transitions were assumed to be of the allowed type (which is consistent with the log(ft) values) and the ground state spin of ^{19}N was assumed to be ½-, which is consistent with the other known odd-mass nitrogen isotopes. Assuming the allowed

decay and the spin of the ^{19}N ground state, the spin and parity of the intermediate levels in ^{19}O are restricted to being either ½- or 3/2-, with 3/2- being the choice that will maximize the resonant contribution (see equation *).

On the basis of these assumptions, the measured energies of the delayed neutrons, and with reference to equation (*), the strength of the ^{18}O(n,γ)^{19}O reaction rate through each excited level of ^{19}O can be reduced to a functional form having but one parameter – the temperature. Equation (*) gives the functional form of the resonant contribution for the delayed neutron emitting states observed in this experiment.

$$< \sigma \upsilon >_{res} \quad = \quad 5.55 \bullet 10^{-19}\ T_9^{-3/2} \times$$

$$[\, Exp(-3.48/T_9) + Exp(-5.69/T_9) + Exp(-7.20/T_9) + Exp(-9.63/T_9)$$

$$+ Exp(-13.11/T_9) + Exp(-14.74/T_9) + Exp(-25.65/T_9) + Exp(-28.90/T_9)$$

$$+ Exp(-32.96/T_9) + Exp(-35.51/T_9) + Exp(-46.42/T_9) + Exp(-56.98/T_9)\,]$$

Clearly, the last several terms will not contribute much to the total resonant capture strength due to the large negative exponent. This is a consequence of the high relative energy of the state with respect to the (^{18}O + n) energy.

4.9.3 COMPARISON OF DIRECT AND RESONANT CAPTURE STRENGTHS

The direct capture strength $<\sigma v>_{dc}$ is given as a function of temperature in equation (*) while the resonant capture strength is given as a function of temperature in equation (*). A plot of the two components of the ^{18}O(n,γ)^{19}O reaction over all temperatures will illuminate the relative probability for the two branches. Figure 50 shows such a plot where the direct capture component is shown in red and the resonant capture component is shown in blue. Also shown is the temperature range normally associated with the inhomogeneous big bang model.

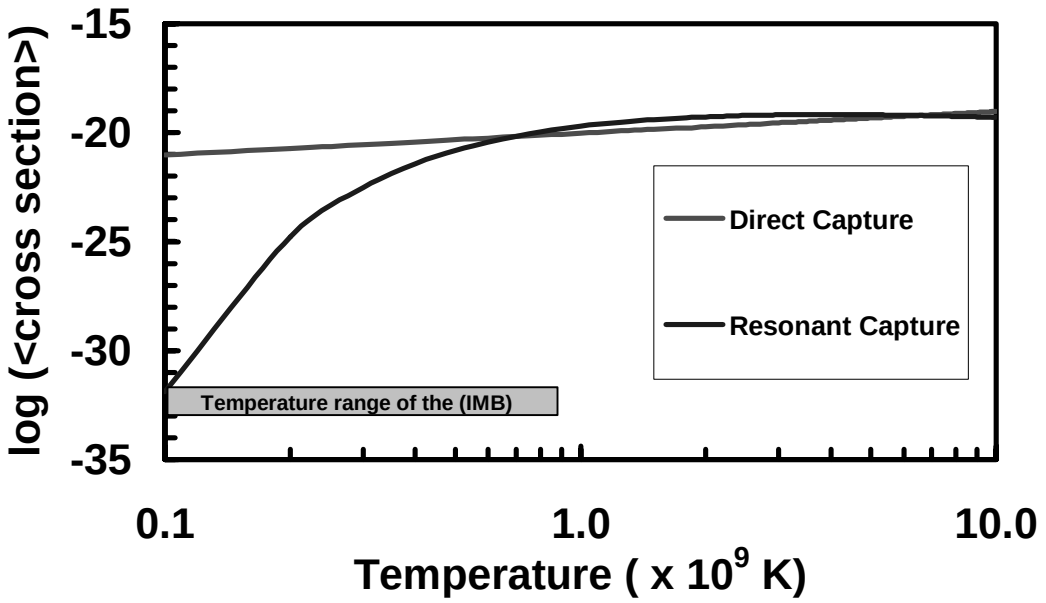

Figure 50 The direct capture and resonant capture cross sections as a function of temperature. The temperature range for the IMB model of the big bang is shaded.

The salient feature of the plot is that the direct capture cross section dominates the resonant capture cross section over most of the temperature range of interest for the inhomogeneous big bang model. In fact, the direct capture component is many orders of magnitude stronger up to a temperature of about 0.4 T_9. Above a temperature of 0.8 T_9 however, the resonant capture is comparable to the direct capture and thus could be the dominant component of the reaction rate at the upper edge of the postulated temperature range of the IMB model.

CHAPTER 5

SUMMARY AND CONCLUSIONS

5.1 SUMMARY AND CONCLUSIONS – ^{19}N

In this experiment, quantitative measurement of the ^{19}N decay was made including a determination of the half life, beta decay to bound excited states of ^{19}O and delayed neutron emission to levels in ^{18}O. The half life of ^{19}N was determined to be 299 (± 4 ±16) milliseconds; which is in agreement with reference [91Re].

Seven gamma rays characteristic of ^{19}O were observed accounting for 39.4(38)% of the total decay strength. The gamma rays suggest direct beta feeding to three, possibly four, bound excited levels of ^{19}O. The levels populated are the 3945 (3/2-), 3232 (1/2-), 1472 (1/2+) and possibly the 96 (3/2+) level, with branching ratios of 34.2(37), 4.9(6), 0.27(12) and 4.3(UL), respectively. The results of the gamma ray spectra are not consistent with those published in [88Duf] as the 709 keV gamma ray reported there was not observed in this experiment.

Twelve delayed neutrons were observed by the neutron bar array and the ^{6}Li glass detectors. The neutrons ranged in energy from 300 keV up to nearly five MeV and in branching ratio from 0.37(4)% up to 16.2(17)% of the total decay strength. In addition, gamma rays from ^{18}O were determined to be from the ^{19}N source suggesting delayed neutron emission to bound excited states of ^{18}O rather than direct population of the ground state. The total delayed neutron emission probability for ^{19}N was found to be 50.9(62)% of the decay strength; which is in agreement with reference [94Re]. The

branching ratio for delayed neutron emission to bound excited states of ^{18}O was found to be 16.5(21)% of the total. Figure 51 shows the beta feeding to specific levels in ^{19}O, where possible, and table 49 shows the transitions that cannot be assigned on the basis of these experimental data.

Table 49 Summary of transitions observed during the decay of ^{19}N that cannot be definitively assigned to intermediate levels in ^{19}O.

Transition Type	Neutron Energy (CoM)	Branching Ratio (%)
(β + n)	300 keV	1.4(3)
(β + n)	490 keV	8.7(10)
(β + n)	2210 keV	2.2(4)
(β + n)	2490 keV	3.5(4)
(β + n)	3060 keV	1.97(32)
(β + n)	4000 keV	0.37(4)
(β + n)	4910 keV	0.90(10)

A comparison of the shell model predictions with the data recorded in this experiment is not particularly favorable. The model derived half life is a factor of two larger than experiment and, with the exception of the lower energy levels being comparable in energy, the delayed neutron emitting excited states do not appear to track between experiment and theory even when the transition uncertainty is included in the mix. It is hoped that consideration of these new data will facilitate improvements in the model parameters to better approximate the reality of this nuclear system.

From the observed neutron energies and their log(ft) values, a functional upper limit on the resonant neutron capture cross section of ^{18}O was derived. The resonant

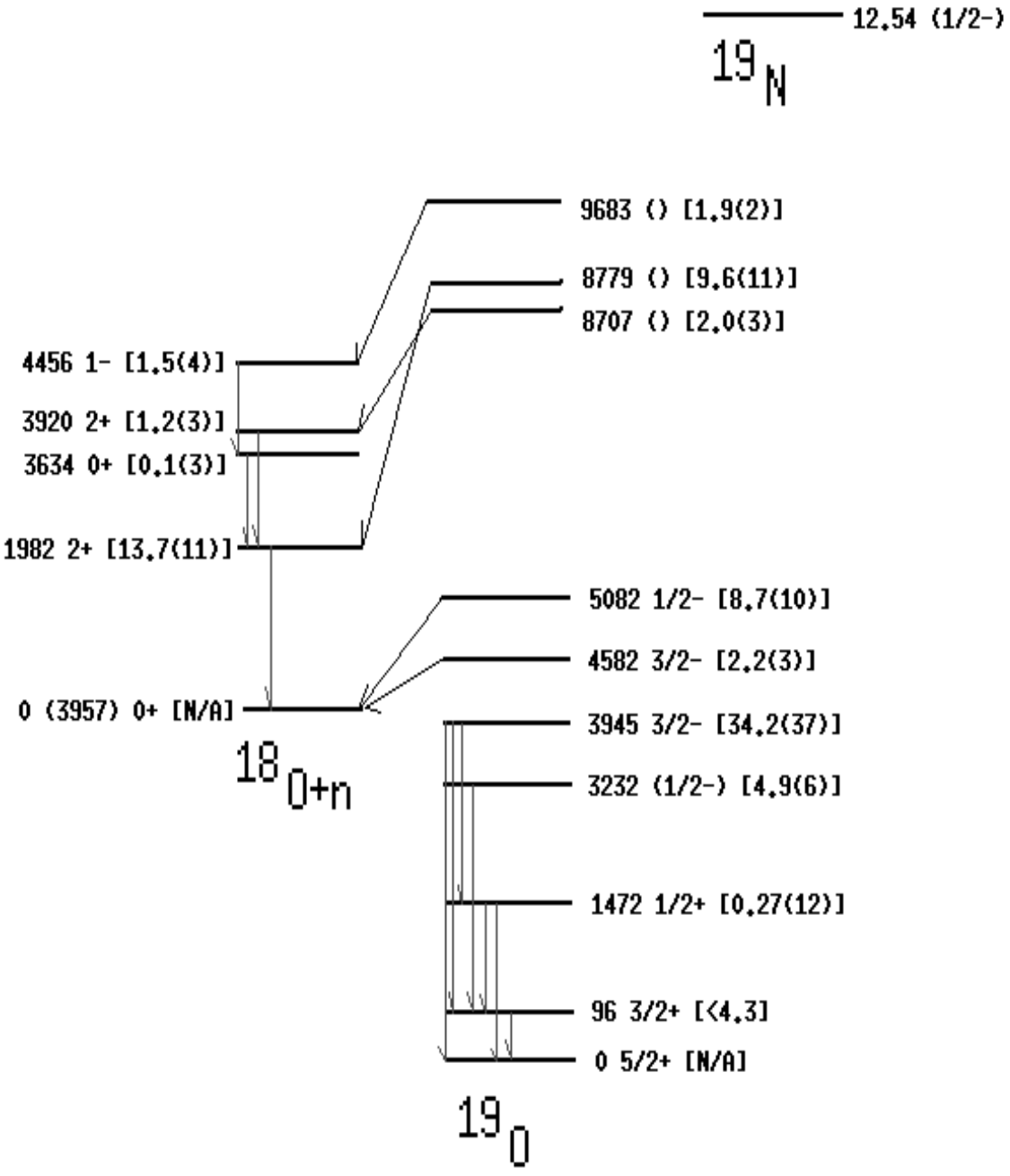

Figure 51 The decay of ^{19}N. Shown are the levels of ^{19}O that are definitely populated during the beta decay with their spin, parity and measured branching ratios.

cross section was compared with the direct capture cross section and found to be orders of magnitude lower, over most of the temperature range of interest, for inhomogeneous big bang models of nucleosynthesis. It is noted, however, that at about (T_9 = 0.8), the upper limit of the resonant part is comparable to the direct capture cross section.

From the beta decay log(ft) values and the known spin and parity of the ^{19}O levels populated, the ground state spin and parity of ^{19}N is restricted to be either (1/2-) or (3/2-). This result is consistent with the common-sense assignment of (1/2-) that is characteristic of all other odd-mass nitrogen isotopes where the ground state properties are known. It is noted that this experiment was not sensitive to the ^{19}N ground-state to ground-state decay, or to delayed alpha emission which is energetically possible.

5.2 SUMMARY AND CONCLUSIONS – ^{20}N

As with ^{19}N, the ^{20}N data permitted re-evaluation of the beta decay half life, measurement of the delayed neutron spectrum, and observation of beta feeding to bound excited states of the daughter ^{20}O. The half life of ^{20}N was found to be 121 ($\pm$ 5 $\pm$10) milliseconds; which is in agreement with the results published in [94Re, 88Mu].

Analysis of the gamma ray data illuminated five transitions characteristic of ^{20}O indicating direct beta feeding to bound levels of the daughter. From the gamma ray energies and the inferred cascades the beta decay can be demonstrated to populate four, possibly five, bound excited levels of ^{20}O. The populated levels are the 5387 (0+), 4456 (0+), 4072 (2+), 1674 (2+) with branching ratios of 1.8(4), 1.2(4), 3.7(8) and 19.5(22) percent, respectively. The fifth possible level is at 3570 (4+) with a branching ratio of 0.8(8) percent (which is also consistent with zero percent). From these spin/parity

values and the calculated log(ft) of the beta decay, the ground state of ^{20}N is most consistent with a (1-) spin and parity assignment.

The neutron bar array permitted identification of eight delayed neutrons ranging in energy from 1.16 to 4.46 MeV and ranging in branching ratio from 0.5(1) to 12.1(13) percent of the total decay strength. The probability for neutron emission is calculated to be 34.0(40)% of the total decay strength for neutrons above 1.1 MeV in energy. From the gamma ray data, two transitions characteristic of ^{19}O are observed and assigned as following directly from the decay of ^{20}N. These are the 96 keV and 1374 keV lines and their observation suggests delayed neutron emission from ^{20}N populating excited levels of ^{19}O rather than the ground state.

Due to the lack of information regarding higher energy levels in ^{20}O, and the uncertainty in the decay characteristics, it is only possible to assign one beta transition to a specific neutron-emitting level of ^{20}O. Figure 52 shows the beta feeding to specific levels in ^{20}O, where possible to assign, and table 50 shows the transitions that cannot be assigned on the basis of these experimental data.

Table 50 Summary of transitions observed during the decay of ^{20}N that cannot be assigned to specific intermediate levels of ^{20}O.

Transition Type	Neutron Energy (CoM)	Branching Ratio (%)
(β + n)	1160 keV	4.5(5)
(β + n)	1330 keV	2.5(3)
(β + n)	1630 keV	8.3(9)
(β + n)	2630 keV	1.3(2)
(β + n)	3380 keV	2.1(3)
(β + n)	3880 keV	2.7(3)
(β + n)	4640 keV	0.5(1)

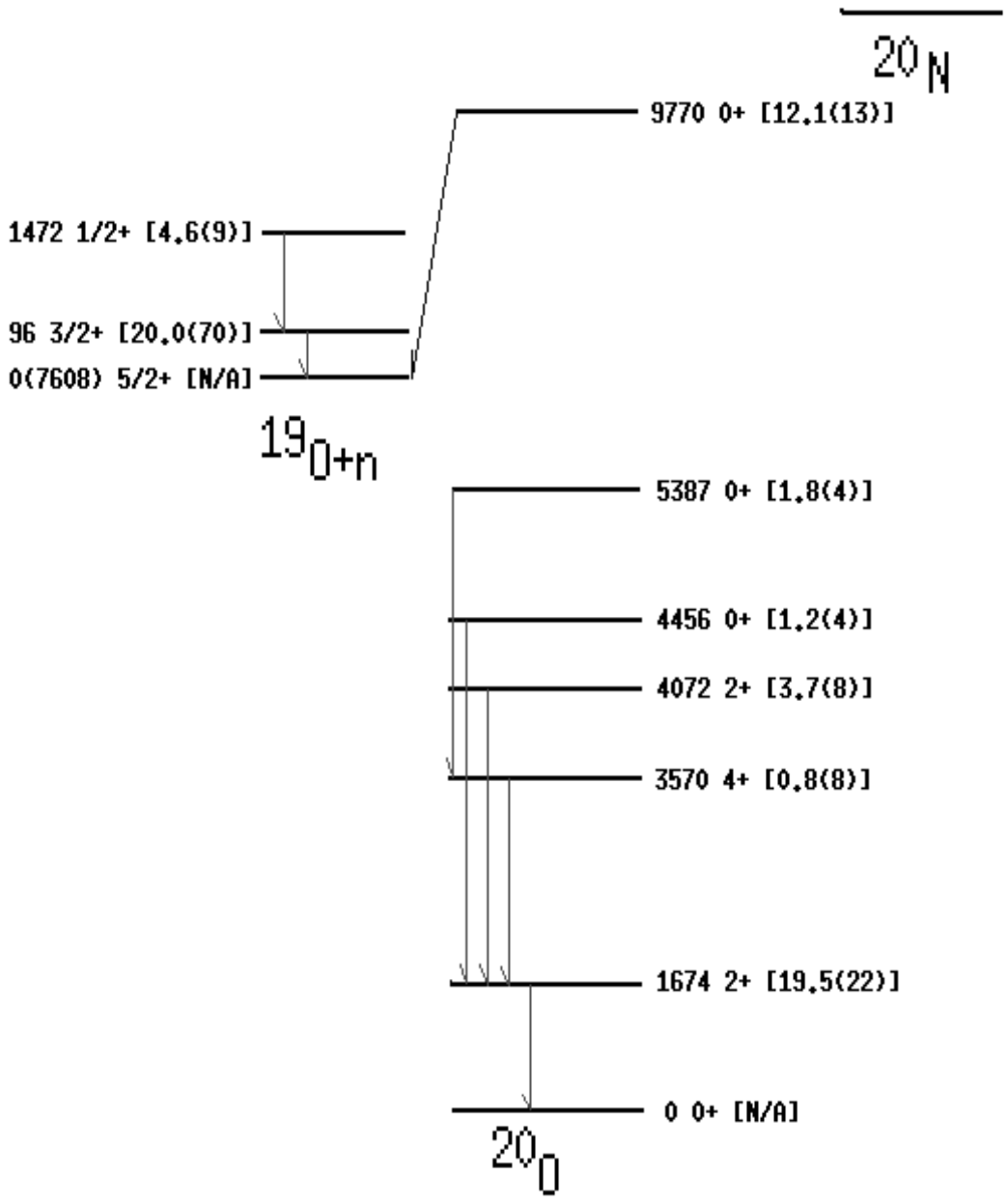

Figure 52 The decay of ^{20}N. Shown are the ^{20}O energy levels definitely populated by the beta decay with the spin parity and branching ratio as a percent of the total decay strength.